8-1-2018

The Mechanical Performance and Microstructure Development of Laser Beam Welds and Post Weld Heat Treatment of Ti 1023 Alloy

Meng Fu Huang
Lehigh University, mengfu248@gmail.com

The Mechanical Performance and Microstructure Development of Laser Beam Welds and Post Weld Heat Treatment of Ti 1023 Alloy

by

Meng Fu Huang

A Dissertation
Presented to the Graduate and Research Committee
of Lehigh University
in Candidacy for the Degree of
Doctor of Philosophy

in

Mechanical Engineering

Lehigh University
August 2018

Approved and recommended for acceptance as a dissertation in partial fulfillment of the requirements for the degree of Doctor of Philosophy.

_____

Date

_____

Dissertation Director: Dr. Wojciech Misiolek

_____

Accepted Date

Committee Members:

_____

Committee Chair: Dr. Wojciech Misiolek

_____

Dr. D. Gary Harlow

_____

Dr. Herman Nied

_____

Dr. David Angstadt

_____

Dr. Timotius Pasang

Acknowledgements

I would like to thank my advisor, Dr. Wojciech Z. Misiolek. We had plenty of meetings and discussions during my doctoral study in Lehigh university. I always could learn from his guidance in each discussion. In addition, he always encouraged me to think and try a little more than what I was capable of. I could feel the growth of my mind and knowledge, that made me immersed in the joy of research. I could not complete this study without his supports and helps. Besides of the professional field, he was very humor, and liked to share his life experience. It is so great that I had this opportunity to work with you, thank you for being my mentor.

I would also like to thank my doctoral committee members: Dr. Gary Harlow, Dr. Herm Nied, Dr. David Angstadt, and Dr. Timotius Pasang. They were so patient to provide me the valuable advices and point out how to extend my research. This was a good journey, thank you for accompanying with me pass through each milestone of my doctoral study.

Next, I would like to thank Dr. Ahmad Chamanfar and Dr. Adam Z. Bunsch. They worked with me on the as-welded specimen analysis and residual stress measurement, respectively. I also learned a lot from you, thank you for showing me how to implement the experiment and measure the residual stress.

Many thanks to Dr. Timotius Pasang team of Auckland University of Technology,

Auckland, NZ. Thank you for the heat treatment discussions and providing the laser beam welding samples.

To the staff of Mechanical Engineering & Mechanics department: Allison Marsteller, Barbara McGuire, and the staff of Materials Science & Engineering department: Janie Carlin, Lisa Arechiga, Dr. Laura Moyer, William J. Mushock, Dr. Robert Keyse, thank you for the kindly helps during my study in the Lehigh university.

Thanks to the 202th Arsenal (Taiwan), which financially supported me to conduct the study in the Lehigh University.

Finally, I must thank my family: my mom (Rui-Ju Zhuang), dad, wife (Chia-Wen Tu), and younger brother (Dian-Long Zhuang). Thank you for raising me or always be there for me on my different life stages. This means a lot to me, and I love you.

Table of Contents

List of Tables

List of Figures

Abstract

Titanium alloys are widely used in the aerospace industry. For example, most components of the Boeing 777 landing gear are made of the Ti-10V-2Fe-3Al (Ti1023) alloy due to its lighweight and superior mechanical strength. In addition, because Titanium is chemicaly active element, when jointing the Ti alloy components, the laser beam welding (LBW) has been selected for avoiding the eventual contaminations and narrowing the heat affected zone by the presence of its protected atmosphere and low heat input. However, there is a lack of reported research results about welded Ti1023 alloy, particularly laser beam welding. Therefore, the microstructure and mechanical properties of LBW Ti1023 were first investigated in this study.

Three zones were formed on the LBW Ti1023: base material (BM), heat affected zone (HAZ), and fusion zone (FZ). The bimodal (spherical and lath) distribution of primary α phase dispersed in a matrix of β phase was observed on the BM and HAZ. However, only β phase was observed in the fusion zone (FZ). This whole β phase structure was formed due to two steps: melting and retaining. The melting temperature was higher than β-transus temperature and transformed the α phase into β phase. Then, fast cooling can avoid α martensite formed and retain the β phase. In addition to the microstructure, the experimental results from the hardness and tensile tests showed lower properties in the FZ. Moreover, the residual stress of BM and FZ were measured

separately in this study.

During analysis of the entire manufacturing process, post welding heat treatment (PWHT) was applied to improve mechanical properties of the welded components. Two subgroups of the heat treatment conditions were set and investigated. The experiment results of both subgroups presented a different extent of strength improvement. The heat treatment condition of one subgroup is annealing+aging. The hardness of all three zones (base material, heat affacted zone, and fusion zone) in this subgroup increased and are almost equal to each other due to their structure consisted of primary α (α_p) and secondary α (α_s) phase. From the hardness profile and tensile test results, the optimization heat treatment condition of this subgroup is chosen as 750^{o}C annealing for 1 hour and following by water quenching, then through 500^{o}C aging for 4 hours and following by air cooling. Another subgroup heat treatment condition consists only of aging. The FZ in this subgroup showed the highest hardness because only α_s was observed. Also, the optimization heat treatment condition is chosen as 500^{o}C aging for 4 hours and following by air cooling.

1. Introduction

1.1 Titanium and its alloys

Titanium (Ti) is the fourth most abundant structural metal (after aluminum, iron, and magnesium) and it is estimated for about 6% in the earth crust [1]. Because its high chemical activity, titanium is usually present in the form of ilmenite ($FeTiO_3$) and rutile (TiO_2) ores. Titanium is the element located in the Group 4 of the periodic table. The atomic number, atomic weight, and electronic configuration of Ti are 22, 47.9g/mol, and $1s^2 2s^2 2p^6 3s^2 3p^6 3d^2 4s^2$, respectively. Titanium was noticed first by British mineralogist, William Gregor, who discovered it in ilmenite in 1791. Then, this element was named "Titanium" by a German chemist, Martin Heinrich Klaproth. However, titanium was not widely investigated and used due to difficult obtaining pure titanium. Titanium reacts easily with oxygen, nitrogen, and hydrogen. An efficient purity titanium process was proposed by a Luxembourg chemist, Kroll, in 1940. He produced pure titanium by reacting $TiCl_4$ with magnesium in an argon atmosphere (known as Kroll process). Development of this process allowed further titanium applications and it still widely used in industry today.

Titanium and its' alloys have several important mechanical properties, which make them were widely investigated and applied in number of industries, mainly in aerospace and automotive racing. First, titanium has high strength to density ratio. That means

that a structural element can achieve the same strength at the reduced, volume and weight in comparison to other metals. In other words, it has higher structural efficiency. For example, titanium' s tensile strength is close to that of steel, but titanium's density is only 60% of steel. When comparing to aluminum and magnesium, although both of them have much lower density than titanium, their tensile strength is roughly only $\frac{1}{3}$ of titanium. Therefore, titanium became an attractive choice and has been used in design to fit the lightweight requirement in the aerospace engines, frames, and components. For instance, several important parts of GE-90 engine, used in Boeing 777 airplane, are made of titanium alloys (Figure 1.1). In addition, most of the landing gear is also made of Ti alloys (Figure 1.2). Second, titanium shows superior corrosion resistance. At the room temperature, titanium reacts with oxygen easily and forms a stable oxide layer (TiO_2, Ti_2O_3, TiO) on the surface. This structure can isolate the inner titanium from the outer environment. So, the chemical and marine industries use many titanium applications. Third, retention of high mechanical properties at elevated working temperatures makes titanium attractive in several aerospace applications. The melting point of titanium is 1,668℃ which is 1000℃ higher than aluminum and magnesium. Also, the mechanical properties of aluminum and magnesium drop rapidly when the temperature is higher than 300℃. However, titanium can retain its high mechanical properties even while the service temperature achieves 600℃. Fourth, titanium has

good biocompatibility and non-magnetic properties. Titanium does not release its ions when put inside a human body. That is why the titanium alloys are so widely used to make tooth implants, artificial knees and heart valves, and cardiac catheters. Besides above specific characteristics, titanium owns other good properties, such as low thermal expansion coefficient. In short, titanium is an attractive and widely used alloy in the aerospace, military, and biomedical industries. More than forty titanium alloys were developed for these commercial businesses. In addition, more than a hundred titanium alloys were investigated so far.

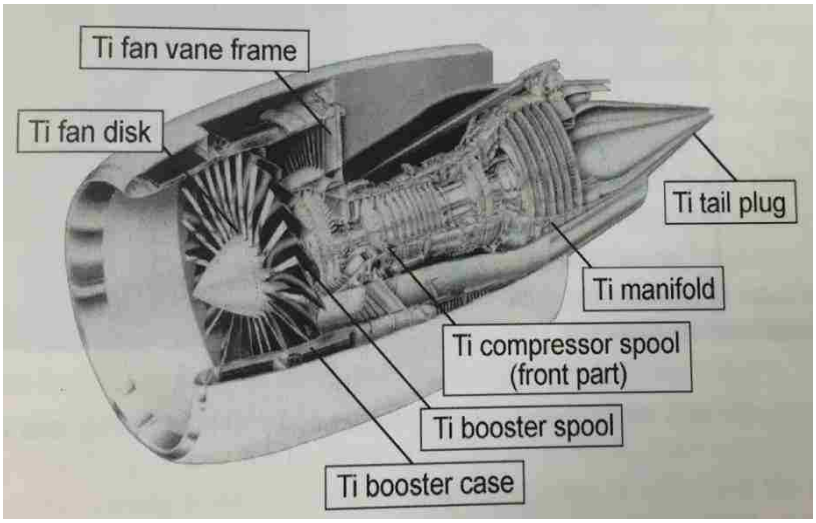

Figure 1.1: Several important parts of GE-90 engine are made of Ti [2]

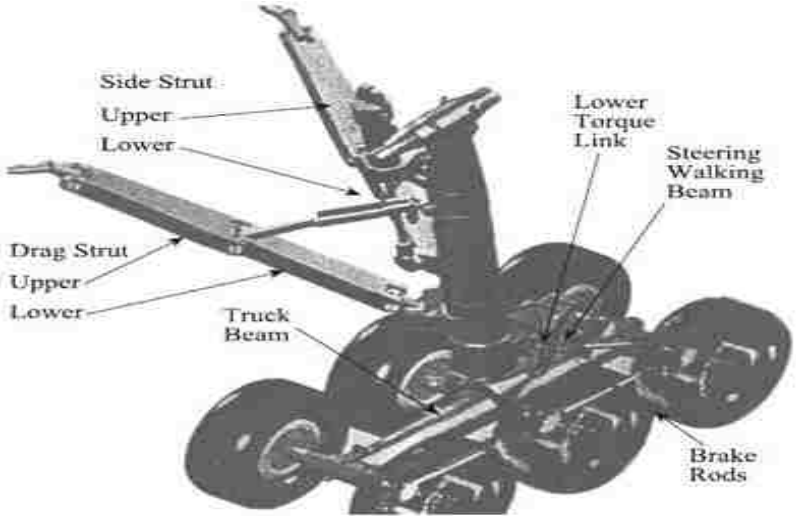

Figure 1.2: Titanium used in the Boeing 777 landing gear [3]

The crystal structure of pure titanium is hexagonal close-packed (α phase) at lower temperatures. Once the temperature is higher than 882℃ (β-transus temperature), it turns into body-centered cubic (β phase). Moreover, the elements of titanium alloys contribute to the α or β phase stability. For example, aluminum (Al) and oxygen (O), are α stabilizers. This type of elements contributes to formation of the α phase and raise the β-transus temperature. In addition, molybdenum (Mo) and vanadium (V), which promoting formation of the β phase and called β stabilizer. Moreover, some elements, such as zirconium (Zr) and tin (Sn), are called neutral due to the fact that these elements only slightly lower the β-transus temperature and then increase it at higher concentrations. The schematic representation of the effect of specific alloying additions on phase diagrams of titanium alloys is shown in Figure 1.3. Three main types of titanium alloys can be classified, which is alpha alloys, alpha+beta alloys, and beta

alloys (Figure 1.4). The descriptions of these three alloys are discussed in the following section.

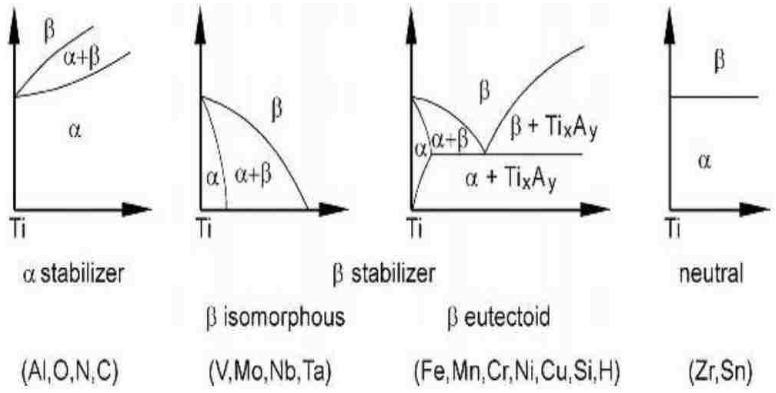

Figure 1.3: The schematic of elements effect on phase diagram of titanium alloys [2]

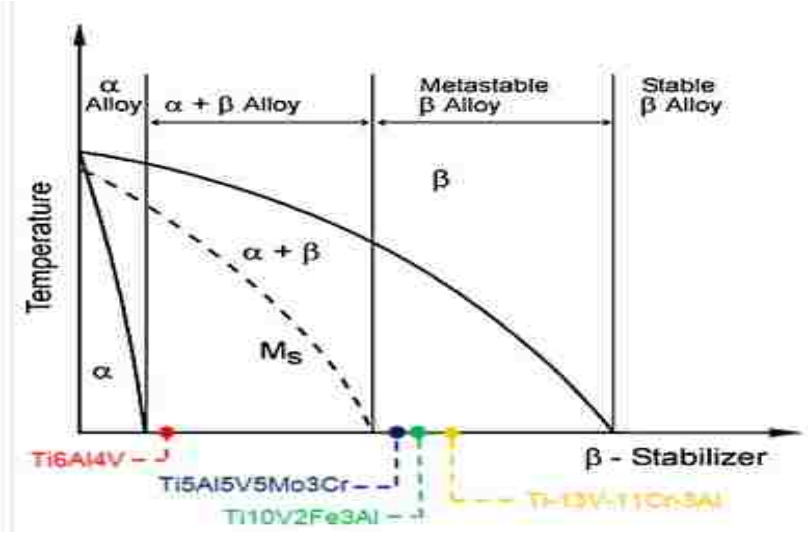

Figure 1.4: Phase diagram shows three main types of Ti alloys [2]

1.1.1 Alpha Alloys

Titanium alloys that contain dominantly α crystal structure and small concentrations of β stabilizers are defined as alpha alloys, such as commercially pure (CP) Ti and Ti-5Al-2.5Sn. Even though not an alloy, CP Ti still is classified into this

group. The main feature of CP Ti is its excellent corrosion resistance. However, CP Ti shows lower strength due to lack of solid solution strengtheners. This issue can be addressed by adding small additions of iron and oxygen. As for other alpha alloys, the predominate α stabilizer is aluminum. In general, alpha alloys consist of high Al content which strongly forms the α phase at room temperature, and even keeps it at high temperatures. Although aluminum shows the signification influence in alpha alloys, there is still a limitation amount of Al, which can be used in these alloys. The Al equivalent (as follows) can describe this relationship [4]:

$$[Al]_{eq} = \frac{1}{3}[Sn] + \frac{1}{6}[Zr] + 10([O] + [C] + 2[N]) \qquad \text{Equation 1.1}$$

After calculation, the weight percent of Al should be less than 9% in order to keep its stability. Or, the finer α_2 (Ti_3Al) is formed and it causes the alloy embrittlement. The α grains commonly are equiaxed [2] and their crystal structure is hexagonal close-packed. Therefore, their forgeability is limited due to this HCP structure. To improve the ductility and tensile strength of alpha alloys, several elements, such as Mo and Fe, can be added into these alloys. These types of element tend to form small amount of β phase between α plates, that provides the improvement of forgeability.

Another benefit of alpha alloys is their good weldability. Comparing the microstructure before and after heat treatment, the structure still stays all α or almost all α. In other words, there is a limited phase transformation. Therefore, this lack of

respond to heat treatment makes them good candidate for welding. However, on the other hand, alpha alloys can-not be strengthened by heat treatment. Thus, like the previous mentioned HCP solution, adding small concentrations of β stabilizers can contribute the strength during heat treatment.

In summary, comparing to alpha+beta and beta alloys, the alpha alloys have several characteristics which are: medium strength, good creep resistance, no responsive to heat treatment, good weldability, and excellent corrosion resistance. In addition, adding small amount of some elements can efficient improve alpha alloys' ductility and tensile strength.

1.1.2 Alpha+Beta Alloys

Alpha+beta alloys contain α stabilizers plus β stabilizers (about 4-6Wt.%) which are used in larger amount than alpha alloys. In addition, this amount of β stabilizers is enough to form and keep the β phase regardless of the manufacturing process or heat treatment. The α stabilizers (such as aluminum) in the alpha+beta alloys contribute to form the α phase and result in higher strength due to the HCP structure. The β stabilizers (such as molybdenum or vanadium) help to form and keep the β phase, and then increases the alloy's ductility [5]. From the pseudo-binary phase diagram (Figure 1.4), alpha+beta alloys compositions range from the alpha/alpha+beta boundary to the

martensite start line (M_s). Therefore, the microstructure of alpha+beta alloys has both the HCP α phase and BCC β phase. Because the heat treatment can change the microstructure of alpha+beta alloys significantly, the phase compositions and mechanical properties will be variety and applied in many purposes. For example, the volume percent of β phase can be controlled by heat treatment. The process begins with raising the temperature higher than the β-transus, and whole alloy transforms to the β phase. Then, by difference cooing rates (such as water, oil, or air), the faster cooling rate preserves more β phase and lath α (martensitic transformation) nucleation and growth [6]. This composition affects higher hardness with expected good ductility. Or, the slower cooling rate allows more lath α phase to nucleate and grow. Sometimes, the α grains even can turn equiaxed in shape. Besides, aging results in another kind of structure. The α phase is much finer and precipitates in the matrix of β phase.

In short, comparing to alpha and beta alloys, the alpha+beta alloys show some characteristic features. First, these alloys can be formed not only by adding different α and β stabilizers but also by the heat treatment. These alloys have the most types of compositions and microstructure. That also provides a wide range of properties for industry applications. For instant, the form and volume percentage of both α and β grain can be adjusted by heat treatment. Also, the α phase promotes hardness and the β phase promots ductility. Second, the strength of these alloys can also be improved by

precipitation of the α phase. Third, because these alloys do strongly response to heat treatment, the weldability of alpha+beta alloys depend on the amount of α phase. High volume percent of α phase makes acceptable weldability.

1.1.3 Beta Alloys

The titanium alloys containing enough β stabilizers to retain a full β phase when quenching from above the β-transus temperature can be defined as beta alloys. In the phase diagram (Figure 1.4), it shows that the beta alloys are located on the right side area of the graph. Also, all the beta alloys do not pass through the martensite start (M_s) line. That means no matter how fast or slow the cooling rate is, there is no α martensite phase formed after quenching [2]. Beta alloys can be divided into two subgroups: metastable and stable beta alloy (in some literature, they are also called solution lean and rich beta alloy [7]). The main difference is the amount of β stabilizers and the precipitation hardening after heat treatment. In these two types of beta alloys, the stable (rich) beta alloys, as its name implies, are composed of high amount of β stabilizers and retain β phase after heat treatment. Thus, the heat treatment can-not increase the strength of stable beta alloys. On the other hand, the metastable (lean) beta alloys contain less β stabilizers and as the result of that the β phase is less stable. When temperature decreases from the β-transus, the β matrix tend to form the primary α phase

and solute the β stabilizers into the remaining β matrix. This microstructure (α and β phase) also can be predicted from the phase diagram (Figure 1.4), the left down area of metastable beta alloys is covered by α+β phase. This alloy chemical composition makes the left β matrix containing heavy β stabilizers and stable β matrix. Also, the driving force of β decomposition during the following annealing and aging is reduced. In the case of quenching, two phases can be observed in the metastable beta alloys, α" and ω. At low aging temperature, the isothermal ω precipitates first and then contributes to forming the α on the further aging. If only ω phase precipitates, it reduces ductility. However, if the aging is long enough to form the α coarse grain, that benefit better strength and ductility (more details of α" and ω are discussed in the following chapter 1.2.2.2 and 1.2.2.3).

In the beta alloys, there are two groups of elements stabilizing the β crystal structure [6]: the β-eutectoid and the β-isomorphous (Figure 1.3). The manganese(Mn), iron(Fe), chromium(Cr), cobalt(Co), nickel(Ni), copper(Cu), and silicon(Si) belong to the β-eutectoid group because these elements form eutectoid phase reaction with titanium. As for β-isomorphous elements, such as molybdenum(Mo), vanadium(V), tantalum(Ta), and niobium(Nb), they are miscible in the β phase. Like the Al is critical α stabilizer, Mo is the important β stabilizer among above-mentioned β stabilizers. Thus, a Mo equivalent concept was proposed to describe the relationship for the β phase

stability and the weighted averages of the alloying elements in wt% [8]:

$$Mo_{eq}=1.00Mo+0.28Nb+0.22Ta+0.4W+0.67V+1.25Cr+1.25Ni+1.7Mn+1.7Co+2.5Fe$$

Equation 1.2

If the Mo_{eq} is higher than 10wt%, β stabilizing elements suppress the martensite formation and preserve the β phase upon quenching [8].

In conclusion, the beta alloys present several characteristics when comparing to the alpha and alpha+beta alloys. In general, beta alloys are denser due to the need of large additions of the heavy β stabilizers (such as Mo, V, Cr). In addition, high amount of β phase contributes to good ductility. That provide a large capacity for cold work. Therefore, the beta alloys fit the requirement for titanium components that need some degree of deformation. Also, for metastable β alloys, the strength after cold work can be improved by heat treatment. Moreover, the creep strength is poor due to the less amount of α phase. Furthermore, after quenching, the α phase is formed easily in the β grain boundary, that decreases the toughness. However, the fracture toughness can be improved by aging.

1.1.3.1 Ti-10V-2Fe-3Al (Ti1023) Alloys

The chemical composition of Ti1023 is shown in Table 1.1 [6]. In general, the microstructure of Ti1023 is α (HCP) phase dispersed in the β (BCC) matrix. When the temperature is higher than Ti1023 β-transus (about 800°C [6]), the whole α phase transforms to the β phase. In addition, the microstructures are also affected by manufacturing processes, such as homogenization, deformation, recrystallization, annealing, and aging [2]. Three images of Ti1023 microstructure at different conditions are presented in Fig. 1.5 [9]. First, when the sample was exposed to the 830°C heat treatment for 2 hours, only β phase could be observed in Fig. 1.5(a). Second, if the heat treatment temperature went down to 775°C, the microstructure showed 10% elongated α phase texture in the β matrix, shown in Fig. 1.5(b). Third, when rolling was added at 680°C to the previous heat treatment conditions, the α grain turned globular, shown in Fig. 1.5(c). Thus, these three types of microstructure show that the volume fraction, grain size and morphology of α and β phase can be controlled by heat treatment temperature and deformation processing. Furthermore, according to the element weight percent, the Mo equivalent for Ti1023 is 11.45%, that is larger than 10%. Therefore, the α martensite is not excepted to be formed even on fast cooling rate [8]. In addition to the microstructure, several mechanical properties were investigated [6,10]. The Vickers hardness of Ti1023 was reported in the range of 300 to 470HV. The hardness is affected

by the volume fraction of α, the size of α and β phase, and precipitation of ω particles. In some beta alloys (such as Ti1023), the β phase transforms to ω particles when rapid quench or aging below 400°C takes place [10]. Also, all mechanical properties such as: the yield strength, ultimate tensile strength, total elongation, and ductility, are interrelated with the microstructure. For instance, the ductility is strongly affected by the morphology of α grain. Coarse and globular α grains make the alloy easy to be formed. On the other hand, acicular and elongated α grains are difficult to form. Therefore, by controlling the manufacturing process and heat treatment, Ti1023 products can achieve excellent fracture toughness with desirable strength for the application in the aerospace industry.

Table 1.1
Chemical composition (wt.%) of the Ti-1023 alloy [6]

Material	Al	Fe	V	C	H	N	O	Ti
Ti1023	2.6-3.4	1.6-2.2	9-11	0.05	0.015	0.05	0.13	Bal.

Figure 1.5: Different microstructure of Ti1023 (a) only β phase exist; (b) 10% elongated α phase texture in β matrix; (c) 10% globular α phase texture in β matrix [9]

1.2 Phases in Titanium

Because its alloys elements, temperature, cooling rate, and deformation process, several phases (crystal structures) can be observed in Ti and Ti alloys. These phases can be divided into two main types: equilibrium and non-equilibrium. The equilibrium phases are formed due to minimum of the Gibbs free energy rule. On the other hand, the non-equilibrium phases exist because of unstable factors, such as fast heating or cooling rate. However, the non-equilibrium phases can turn to equilibrium easily if the favorable processing parameters are in place.

1.2.1 Equilibrium Phases

The α and β phase are the most basic and important crystal structure in the Ti and Ti alloys. In addition, other equilibrium phases which only exist in some specific composition of Ti alloys are also discussed in this section.

1.2.1.1 α Phase

When the temperature is lower than β-transus (or at room temperature), the α stabilizers contribute to forming α phase in the Ti and Ti alloys. This α phase has a hexagonal close-packed (HCP) crystal structure. The schematic of α structure is shown in Figure 1.6 [2]. At room temperature, the values of α lattice parameters a and c are 0.295nm and 0.468nm, respectively. After calculation, the c/a ratio is 1.587, which is smaller than HCP ideal ratio (1.633) [5]. The most densely packed plane (basal plane)

is the (0002) plane (at the bottom of unit cell). Also, the a_1, a_2, and a_3 axes are the close-packed directions within $\langle 11\bar{2}0\rangle$. The elastic modulus (E) ranges from 145GPa (stress axis parallel to the c-axis) to 100GPa (stress axis perpendicular to the c-axis). And, the shear modulus (G) varies from 46 GPa to 34 GPa when the shear stress is in the (0002) and $\{10\bar{1}0\}$ planes with the $\langle 11\bar{2}0\rangle$ direction. When the temperature is increased, both E and G decrease. The slip systems for Ti, there are three main slip directions $\langle 11\bar{2}0\rangle$. The slip planes are (0002), three $\{10\bar{1}1\}$, and six $\{10\bar{1}1\}$. Therefore, they make total of 12 slip systems [2]. However, in the room temperature, there are only 3 slip systems in HCP crystal structure.

Two types of α phase can be classified: primary α (α_p) and secondary α (α_s) [9]. The α is formed upon the solution treatment, cooling from the β-transus, and annealing (700~780℃). This process is called primary α. In contrast, when aging at lower temperature (400~550℃), the formed α becomes secondary α. The morphology of both α phases is also different. The α_p has particle shape at the beginning stage. Then, as more α_p particles are formed, they coalesce together and grow to form lathes, islands, and then coarser structures. However, because the α_s is precipitated on a lower temperature, α_s is generally finer than α_p and not easy to be observed. Although there are some different between these two α phases, the basic crystal structure of them is the same (HCP).

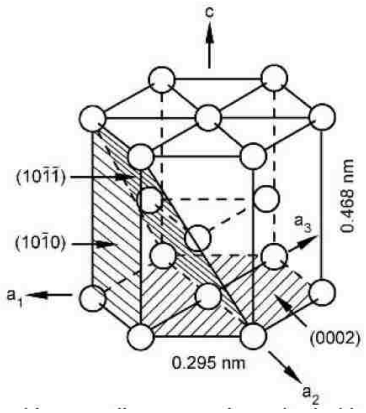

Figure 1.6: A schematic of α unit cell which is the hexagonal close-packed (HCP) crystal structure [2]

1.2.1.2 β Phase

When the temperature is higher than 882℃, the α phase in the pure Ti turns into β phase. This temperature is also known as β-transus. The elemental composition of Ti alloys strongly affect the exact transformation temperature. Same as the α stabilizers contributes to forming of the α phase, the β phase depends on the amount of β stabilizers. The β phase presents a body-centered cubic (BCC) crystal structure. Figure 1.7 shows a schematic of β unit cell [2]. The lattice parameter of β in the pure Ti is 0.332nm. The elasticity modulus and shear modulus of β phase are 58 GPa and 20 GPa, respectively. Also, these two moduli values are more precise at higher temperature due to the fact that the β phase is more stable at higher temperature. The most densely packed family of planes is $\{110\}$. And, the close-packed directions are $\langle 111 \rangle$. For its' slip systems, the planes are $\{110\}$, $\{112\}$, $\{123\}$, and the directions are $\langle 111 \rangle$. That gives a total 48 slip systems in β phase. Thus, comparing to the HCP of α phase, the

BCC of β phase is much more easily to deform.

When the temperature is lower than the β-transus temperature, the diffusional transformation of β into α is present in all Ti alloys. The α phase plays an important role to influent the alloys' mechanical properties due to the α's HCP crystal structure, especially among the beta alloys. There are several favor orientations while the β phase transformed to the α phase. The driving force is minimum at the interfacial energy between these two phases. These four orientation relationships (OR) are shown as follows:

Burgers OR: $(0001)_\alpha // \{011\}_\beta ; \langle 11\bar{2}0\rangle_\alpha // \langle 1\bar{1}1\rangle_\beta ; \{1\bar{1}00\}_\alpha // \{121\}_\beta$

Pitsch-Schrader OR: $(0001)_\alpha // \{011\}_\beta ; \langle 11\bar{2}0\rangle_\alpha // \langle 100\rangle_\beta ; \{1\bar{1}00\}_\alpha // \{0\bar{1}1\}_\beta$

Potter OR: $(0001)_\alpha 2° from \{011\}_\beta ; \langle 11\bar{2}0\rangle_\alpha // \langle 1\bar{1}1\rangle_\beta ; \{1\bar{1}01\}_\alpha // \{110\}_\beta$

Rong-Dunlap OR: $(0001)_\alpha // \{021\}_\beta ; \langle 11\bar{2}0\rangle_\alpha // \langle 100\rangle_\beta ; \{1\bar{1}00\}_\alpha // \{0\bar{1}2\}_\beta$

Among above orientation relationships, the Burgers OR is the first studied and confirmed in titanium [2,16]. The martensite transformation, nucleation, and growth of α phase are all following this Burgers OR.

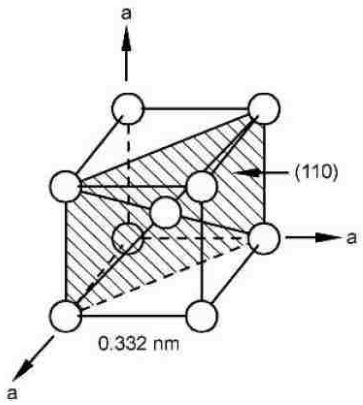

Figure 1.7: A schematic of β unit cell which is the body-centered cubic (BCC) crystal structure [2]

1.2.1.3 Other Phases

Two other equilibrium phases can be found in the Ti-Al alloys (system): α_2 and γ [2]. If the Al content is higher than 5wt%, α_2 precipitates in the α matrix. In contrast, the γ is formed when the Al content exceeds 50wt%. The composition of α_2 and γ is Ti_3Al and TiAl, respectively. In α_2, the Al element may be substituted by Sn, Ga, or In. Both of α_2 and γ reduces alloys' ductility due to their crystal structure. The α_2 is hexagonal with a DO_{19} structure, and the γ has a tetragonal L 1_0 structure. These two structures have fewer slip systems than α's. The α_2 was observed in Ti-6Al-4V, and the γ was found in Ti-48Al-2Cr.

Another phase, O, can be formed at a higher Nb concentrations of composition Ti_2AlNb which contain 25wt% Al and 12.5-24wt% Nb [2]. The crystal structure of this phase is similar to the α_2, but the lattice parameter is different. The atomic radii difference of Al and Nb distort the hexagonal (α_2) structure and make it an

orthorhombic cell. One more phase, B2 (CsCl), can be found at Nb concentrations of about 15wt% or higher, such as Ti-25Al-15Nb [2]. B2 is made of two interpenetrating BCC lattices. Also, the rapid quenching from the β field results in this phase and make it brittle.

1.2.2 Non-Equilibrium Phases

When fast heating or cooling, not only the equilibrium phases are formed, but also several non-equilibrium phases are presented. This is because the atoms diffusion has not long enough time for controlling nucleation and growth to form the stable phases. Here, kinetics dominates the phase formation, such as martensitic transformation. The name martenstite is taken from steel terminology because this transformation fulfills the general characteristics of the martensitic reaction [5]. Four non-equilibrium phases (α', α", ω, β') are introduced in this section.

1.2.2.1 α' and α"

Normally, the β phase transforms to the α phase when the temperature lower than the β-transus. However, the rapid quenching results in martensitic transformation and then formation of α' and α". One can see in the phase diagram of Ti alloys (Figure 1.4), the M_s line presents the start of martensitic transformation. That means the cooling located on the right hand side of this line causes martensitic reaction. Also, this phase

diagram shows that the M_s temperature is a function of Ti alloys content. The crystal structures of α' and α" are hexagonal and orthorhombic, respectively. There were two morphologies observed for α': massive martensite and acicular martensite [1,2]. Massive martensite can only be formed in pure Ti. Also, it contained packets of parallel α plates or laths. As for acicular martensite, it consisted a mixture of α plates which have different Burgers relationship. In general, the α' is formed mostly in the lean solute content of Ti alloys, such as Ti-6Al-4V. As the solute content increased, the α" is usually present, such as in Ti-6Al-2Sn-4Zr-6Mo alloy. But, because Mo is a strong β stabilizer, high content of Mo (>10wt% [11]) has suppressed this martensitic transformation and still retained the β phase. The distinction between α' and α" is unclear, some authors used α^m to present both α' and α" [1]. Calculating the electron-to-atom ratio was provided to estimate which is phase prefered to be formed [12]. If the electron-to-atom ratios was greater than 4.07, the α" phase tend to be formed. Otherwise, the α' phase was formed favorly [13]. These two non-equilibrium phases contained a high dislocation density [2] and leaded to lower ductility, but they did not make alloys brittle [5].

1.2.2.2 ω and β'

The ω phase can be divided into two types: athermal and isothermal. Both

of them were hexagonal crystal structure. Also, their lattice parameters are the same: a=0.282nm and c=0.460nm, but they have different crystal symmetries [14]. These two metastable phases can be distinguished in accordance to the forming process. The athermal ω (ω_a) is formed during the cooling stage. In contrast, the isothermal ω (ω_{iso}) is formed during the aging stage [5]. Even though aging contributed to forming of the ω phase, the ω phase turnes to equilibrium α phase when the aging time is too long. The ω phase is very fine (about 2-4nm) and difficult to resolve optically. Generally, the ω phase has cuboidal and ellipsoidal morphologies. These ω morphologies depend on the mismatch between the ω particle and the β matrix. High value of this mismatch causes the cuboidal morphology, and lower mismatch results the ellipsoidal morphology. According to Hickman, the ω phase does not form in the Ti-Nb system during rapid quenching due to formation of the α' and α". However, after reheating the Ti-Nb alloys, the ω phase can precipitate and retain when cooling down to the room temperature [15]. When the Ti alloys contain high volume of the ω phase (more than 50% [5]), the embrittlement occurs. But, the ω particles also can resist the dislocation movement. Therefore, small amount of ω phase can strength the alloys properties, but high volume of ω phase was not acceptable in industry applications.

During the Ti alloys rapid quenching, the retained β phase may contain a non-equilibrium phase: β'. This phase is stable in the solute rich beta alloys. Both of β

and β' are BCC, but with different lattice parameters due to the fact that β is the solute rich phase and the β' is the solute lean phase. Even though the β' can precipitate in the β phase, there still is no hardness increase [5].

1.3 Welding Titanium Alloys

In industry, some metal workpieces may have too complex shapes, or need to be joint into a larger part, or there is a need to repair a damage. The welding technique has been developed and it is very useful to fulfill these fabrication requirements. So, without exception, the welding is also very widely used in the titanium business. However, because the characteristic of Ti, some welding techniques can damage the original properties of Ti alloys. Therefore, the welding methods used for Ti alloys and challenges they face are discussed. In this discussion, the laser beam welding has several advantages for Ti alloys welding. Then, the research on the laser beam welding of the Ti alloys is described in the following chapter.

1.3.1 Welding Methods and Encountered Problems

In the traditional welding process materials are joint by the metal fusion by providing a lot of heat and forming sizeable welding pool. The traditional welding methods also can be applied to Ti and Ti alloys. However, the first encountered problem are the severe contaminations, such as oxidation or hydrogenation. Because Ti is a

highly reactive metal, it is very easy for Ti to react with the elements from the atmosphere, such as oxygen, hydrogen, and nitrogen. These contaminations result in the embrittlement of Ti alloys. Therefore, several welding methods are more appropriate to avoid this situation. The examples are: the shielded metal arc welding (SMAW), gas tungsten arc welding (GTAW), gas metal arc welding (GMAW), and laser beam welding (LBW). In these welding methods, the welding workpiece is shielded by a protect atmosphere, for instance, the argon gas. Another method, which can achieve this purpose is the electron beam welding (EBW). This method does not provide a protected atmosphere, but it achieves shielding of the molten metal by providing a high vacuum. In short, these welding methods prevent the Ti exposure to the atmosphere and eventual embrittlement.

Another problem is deterioration of the mechanical properties after welding. Several reasons have been proposed for this deterioration including solidification segregation, contamination cracking, hydrogen embrittlement, porosity, and phase transformation [6]. For example, Tal-Gutelmacher et al. discussed the hydrogen embrittlement of Titanium-base alloys [37]. In addition, the solidification cracking should be considered when joint Ti-6A-4V [6]. However, the phase transformation was the dominant of mechanical properties changes during welding. During the welding process, the working zone is a fusion zone (FZ). Then, the FZ fast cooling and

solidification after the welding resource left. This wide temperature range and rapidly change made the FZ microstructure transformation. Thus, the mechanical properties were also affected according this change. For example, for the beta alloys, the ductility decreased on the FZ. A useful method was proposed to solve this issue, the heat treatment (more detailed were discussed in chapter 1.4).

1.3.2 Laser Beam Welding

The Laser Beam Welding (LBW) not only can avoid the Ti alloys welding embrittlement by providing an Ar protect atmosphere, but also provides several advantages in Ti alloys welding [17,18]. First, the high aspect ratio of weld geometry. The laser beam is generated from Nd:YAG or CO_2 emission laser systems and can be focused control by its energy up to 10^3-10^7 W/mm^2 spot. That contributes narrower weld width and larger weld depth for reducing the heat affected area. Second, the diameter and focused location of laser spot can be adjusted and controlled precisely. That gives the wide applications for workpiece of variety geometries. Third, comparing to arc welding, the lower heat input of LBW meant smaller temperature difference range. That contributed to lower microstructure and mechanical properties change. Therefore, laser beam welding is widely used in aerospace industry [17]. Several research articles about LBW Ti alloys have been reported [19-21]. Denny investigated the LBW Ti-6Al-4V (Ti64, alpha+beat alloy) [19]. Three zones which were the base

metal (BM), heat affected zone (HAZ), and fusion zone (FZ) were present after welded. The microstructure images of these three zones are shown in Figure 1.8. The α grain was contained in the intergranular β phase in the BM. When analyzing the HAZ, the acicular α textured in the transformed β phase is observed. As for the FZ, the acicular α phase was observed and the β grain grew larger. Also, the grain size of the FZ β can be controlled by the laser power and cooling rate. Beside microstructure, the hardness profile of LBW Ti64 is shown in Figure 1.9. It can be observed that the hardness increased as moving from BM toward HAZ and FZ. In addition, other mechanical properties, such as yield strength (YS), ultimate tensile strength (UTS), reduction in area (RA), and elongation (EL), were measured and presented decreased in the FZ. Denny believed that the grain size is one of the most important factors to affect mechanical properties.

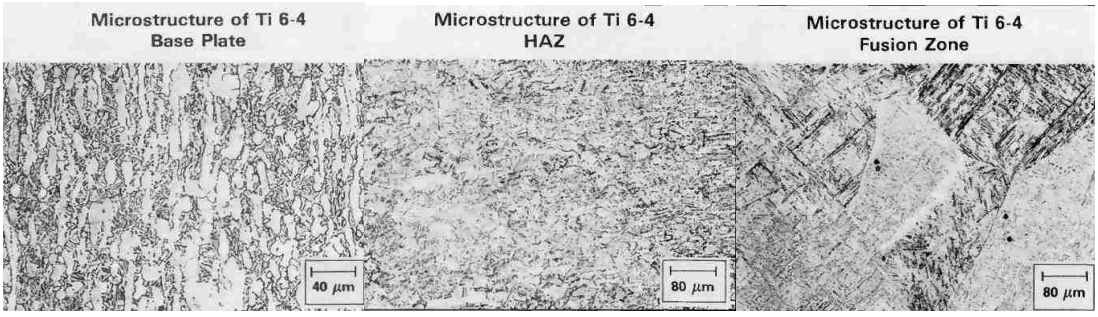

Figure 1.8: Microstructures of Ti64 after LBW at base metal, heat affected zone, and fusion zone [19]

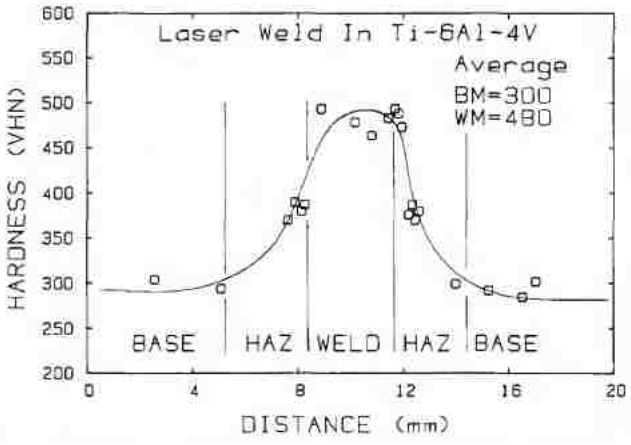

Figure 1.9: Hardness profile of Ti64 after LBW [19]

The mechanical properties and microstructure of LBW Ti-6Al-2Sn-4Zr-2Mo (Ti6242, alpha+beta alloy) was investigated by Chamanfar et al. [20]. The microstructure of the three zones are shown in Figure 1.10. The acicular α in the β matrix also can be observed in the FZ. This acicular α structure was believed coming from the martensite transformed due to the fast cooling in the alpha+beta alloys. In addition, the hardness evolution of LBW of Ti6242 has a similar tendency with LBW Ti64. Here, this formed acicular α' martensite was believed to contribute to the higher hardness due to its HCP crystal structure. Moreover, the microstructural difference and several welding defects reducing the values of YS, UTS, and EL were observed.

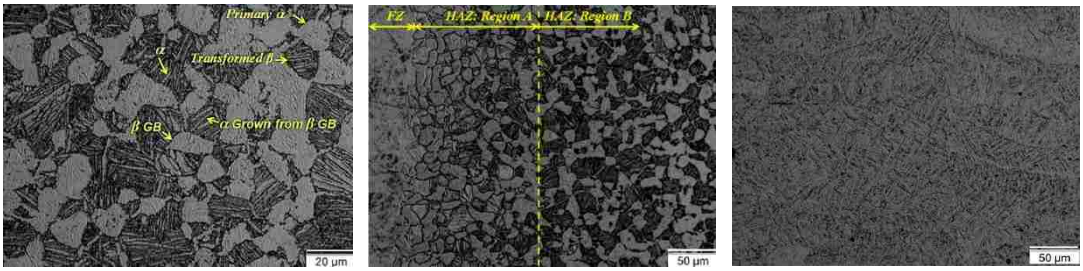

Figure 1.10: Optical images of Ti6242 after LBW at BM, HAZ, and FZ (from left to right) [20]

Beside alpha+beta alloys, a beta alloys Ti-5Al-5V-5Mo-3Cr (Ti5553, beta alloys) after LBW was investigated by Pasang et al. [21]. Figure 1.11(a) shows the BM microstructure that consists α particles distributed within the β matrix. Figure 1.11(b) includes the microstructure of the HAZ and FZ. The equiaxed β phase was observed in the HAZ. In addition, the β grain size grew from the HAZ toward the FZ. Moreover, only columnar and dendritic morphology of β phase was shown in the FZ. Figure 1.12 shows the hardness profiles across three zones of LBW Ti5553. The hardness of FZ was lower than that of HAZ and BM. That revealed a total opposite trend of alpha+beta alloys hardness profiles. It was believed that there was no acicular α' martensite formed in β alloys. The crystal structure of α phase (HCP) has fewer slip system and is harder than β phase (BCC). Thus, this whole β structure (without any α) contributed to this phenomenon. Finally, the UTS and elongation measurement were decreased after LBW.

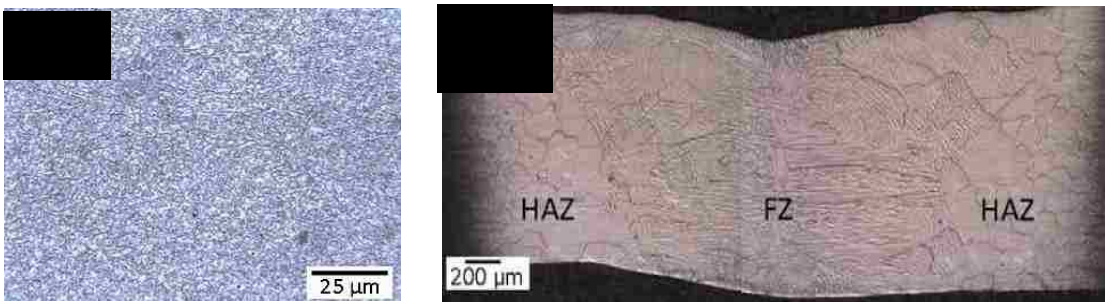

Figure 1.11: Optical images of Ti5553 after LBW at (a) BM, (b)HAZ and FZ [21]

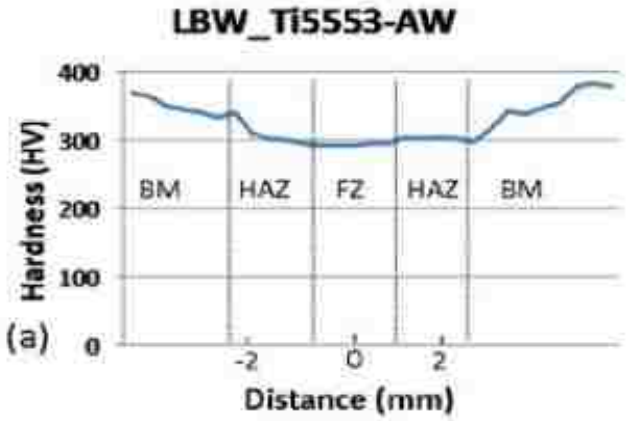

Figure 1.12: Hardness profile across three zones of Ti5553 after LBW [21]

1.4 Post Weld Heat Treatments

1.4.1 Purpose and Procedure of Post Weld Heat Treatments

During the welding, not only high energy is put into the workpiece, but also temperature is elevated and dropped very fast. This heating and quenching procedure is responsible for microstructure differences within the workpiece. And then, in general, the mechanical properties tend to represent microstructural changes as well. Therefore, the efficient method to solve this issue is post welding heat treatment (PWHT). When doing the PWHT, the welded workpiece is reheated to a temperature below its lower transformation temperature. And then, kept it at that temperature for amount of time to guarantee temperature equilibration. During this PWHT, the input energy provides kinetic energy to the atoms of the workpiece. Thus, released residual stress, reduced defects, retained or even enhanced strength are all excepted after PWHT.

1.4.2 Post Weld Heat Treatments of Titanium

Several PWHT of Ti alloys have been investigated [22-24]. The tensile strength and ductility of LBW Ti-23Al-17Nb were improved after 980^{o}C heat treatment and air cooling [22]. Zhang studied the TC4 and TC17 conditions after linear friction welded and PWHT [23]. The hardness of TC4 was decreased after PWHT. In contrast, the hardness of TC17 after PWHT showed an opposite result. Zhang believed that this phenomenon was related to the morphology of α martensite. In addition, the PWHT of LBW Ti-15V-3Cr-3Al-3Sn and Ti64 was observed that the hardness was increased in both Ti alloys. Thus, these researchers demonstrated that the mechanical properties of PWHT LBW welding Ti alloys were mostly improved. And, this improvement was based on its microstructure.

1.4.3 Heat treatment of Ti1023

Because there is no available literature on PWHT of LBW Ti1023 has been available, the research of Ti1023 heat treatment was investigated [9,31,32]. The relevance of heat treatment temperature and resulting microstructure is shown in Figure 1.13 [9,31]. Due to the β-transus of Ti1023 is about 800^{o}C, the heat treatment (annealing) temperature should be lower than it. So, it can be observed that the heat treatment at 700-780^{o}C formed the primary α (α_p) phase. In addition, the secondary α (α_s) phase was precipitated in the aging step at 400-550^{o}C. The morphology of α_p phase was globular

or lamellar. In contrast, the α_s phase was in the form of very fine particles and difficult to observe under optical microscopy. The reason of this big different morphology of α_p and α_s is the temperature they were formed. The higher formed temperature of α_p made its grain coarser. In addition, two mechanical properties were measured. The hardness was higher when material was exposed to the aging treatment [9]. And, the ductility decreased for the microstructure which contained no α_p [32].

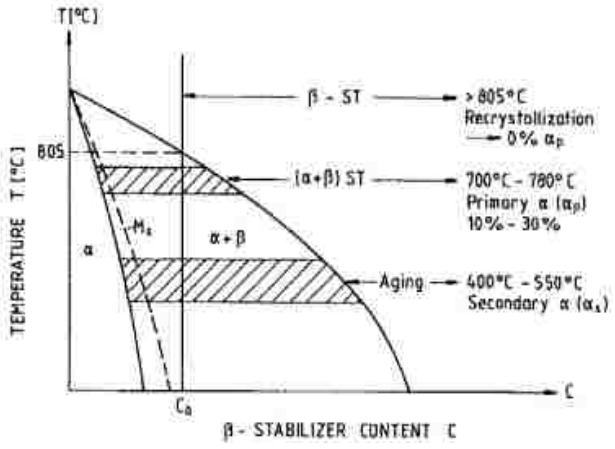

Figure 1.13: Schematic phase diagram of Ti1023 [9,31]

1.5 Residual Stress Measurements

1.5.1 Residual Stress

When an external force is applied to a material, a stress inside of the material is generated to resist this external force. Once this external force is removed, the stress should disappear and the material should be back to its original state. In some cases, even when the external force is removed, there is a remaining stress within the material.

This is called residual stress. This kind of residual stress is usually generated from mechanical loading. Another kind of residual stress could be generated from thermal cycling or as the result of phase transformation. Because of the presence of the external forces the crystal lattice strains and its characteristic parameters changed. Especially when the material is exposed to a wide temperature difference and rapid cooling rate, such as welding, the massive phase transformation generates high residual stress.

Generally, residual stresses cannot be measured directly. Thus, they can be calculated based on the measured local strain ε. There are several methods to determine the residual stress, such as mechanical, magnetic, ultrasonic, thermoelastic, photoelastic, electrical, and diffraction techniques [25]. Among the diffraction techniques, the most commonly used method for stress determination is the $\omega - d_{hkl} sin^2\Psi$ method [26]. The description of this diffraction method is provided below. First, from Bragg's law:

$$n\lambda = 2d_{hkl} \sin\theta \qquad \text{Equation 1.3}$$

where n is an integer, λ is the wavelength of the X-ray, d_{hkl} is the inter-planar spacing, θ is the angle of the diffraction lines. When there is no stain in the material, the d_{hkl} equals d_0 which is the strain free inter-planar spacing. The θ shift take place due to the fact that the present local strain is responsible for a change in the inter-planar spacing d. Thus, the inter-planar spacing can be measured using the X-ray diffraction and then one can perform the strain and eventually stress calculations. When making

the measurements on the surface, the strain in z-direction (ε_z) is:

$$\varepsilon_z = \frac{d_n - d_0}{d_0} \qquad \text{Equation 1.4}$$

where d_n is the inter-planar spacing of planes which are normal to the specimen. If titling the specimen at an angular Ψ, the strain is:

$$\varepsilon_\Psi = \frac{d_{\Psi\emptyset} - d_0}{d_0} \qquad \text{Equation 1.5}$$

$\emptyset$ is the rotation angle of specimen (also as angle between a fixed direction in the plane of the sample and the projection within that plane). From Hooke's law:

$$\sigma_y = E\varepsilon_y \qquad \text{Equation 1.6}$$

E is elastic modulus. In addition, the Poisson's ratio ν can be shown as:

$$\nu = -\frac{\varepsilon_x}{\varepsilon_z} = -\frac{\varepsilon_y}{\varepsilon_z} \qquad \text{Equation 1.7}$$

Assuming there is a stress only within the analyzed plane, this means that $\sigma_z = 0$. Thus,

$$\varepsilon_x = \varepsilon_y \qquad \text{Equation 1.8}$$

Combining Equation 1.6-1.8:

$$\varepsilon_x = \varepsilon_y = -\nu\varepsilon_z = \frac{-\nu\sigma_y}{E} \qquad \text{Equation 1.9}$$

When applying stress σ_x along x direction to strain the material, the Equation 1.9 can be expressed as:

$$\varepsilon_z^1 = -\frac{\nu\sigma_x}{E} \qquad \text{Equation 1.10}$$

Also, when applying σ_y along y direction to strain the material, the Equation 1.9 will change to:

$$\varepsilon_z^2 = -\frac{\nu\sigma_y}{E}$$ Equation 1.11

And, when applying σ_z along z direction to strain the material, form Equation 1.6:

$$\varepsilon_z^3 = \frac{\sigma_z}{E}$$ Equation 1.12

By assuming $\sigma_z = 0$ and combining Equation 1.10-1.12, we will get a new form:

$$\varepsilon_z = \varepsilon_z^1 + \varepsilon_z^2 + \varepsilon_z^3 = -\frac{\nu}{E}(\sigma_x + \sigma_y)$$ Equation 1.13

Then, combining Equation 1.4 and 1.13 will give us:

$$\frac{d_n - d_0}{d_0} = \varepsilon_z = -\frac{\nu}{E}(\sigma_x + \sigma_y)$$ Equation 1.14

From elasticity theory for an isotropic solid and a bi-axial stress on the surface [27]:

$$\varepsilon_{\emptyset\Psi} = \frac{d_{\emptyset\Psi} - d_0}{d_0} = \frac{1+\nu}{E}\left(\sigma_x cos^2\emptyset + \sigma_y sin^2\emptyset\right) sin^2\Psi - \frac{\nu}{E}(\sigma_x + \sigma_y)$$ Equation 1.15

Where, the surface stress $(\sigma_\emptyset)$ is $\sigma_x cos^2\emptyset + \sigma_y sin^2\emptyset$. Thus, from Equation 1.15, the relation of the plane space and $sin^2\Psi$ can be shown as:

$$\sigma_\emptyset = \frac{E}{(1+\nu) sin^2\Psi}\left(\frac{d_{\emptyset\Psi} - d_0}{d_0}\right)$$ Equation 1.16

Here, a gradient of the inter-planar spacing $\left(\frac{d_{\emptyset\Psi} - d_0}{d_0}\right)$ and angular $(sin^2\Psi)$ can be observed from Equation 1.16. In other words, this slope presents the stress of material. This is known as the XRD residual stress method and its schematic is shown in Figure 1.14.

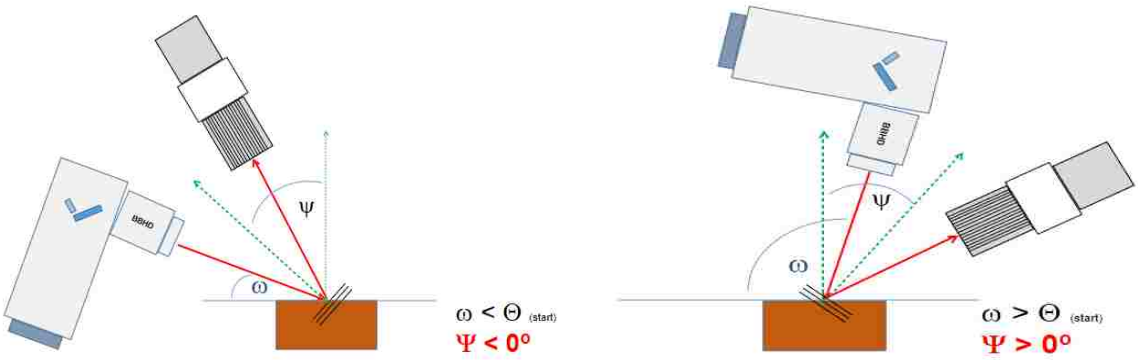

Figure 1.14: The schematic of XRD residual stress measurement (left) Ψ tilt < 0∘ and (right) Ψ tilt > 0 [39]

1.5.2 Residual Stress Measurement of Titanium

Among studies of residual stress in Ti alloys, most researches focused on the Ti64 alloy [28-30]. Rae measured the residual stress of electron beam welded Ti64 [28]. The results showed the residual stress on the FZ was higher than this within the HAZ and BM. And, the highest residual stress was located in the middle of the FZ. Meanwhile, the microstructure of FZ presented an acicular α' martensite in the β grains. Meng and Zhou investigated the residual stress variety of Ti64 alloy after laser peening [29,30]. Both researches showed that the residual stress distribution became more uniform after thermal relaxation.

1.6 Motivation

Because the beta alloy Ti1023 was widely used in the aerospace industry, such as the application in the landing gear of Boeing 777, its microstructure and mechanical

properties had been proposed in the presented study. Meanwhile, the laser beam welding showed many advantages when applied to the Ti alloys in the aerospace industry. For instance, the Ar gas atmosphere prevented contaminations during welding. Some of Ti alloys after LBW have been studied. However, there is a lack of research results on welded Ti1023, particularly laser beam welding. In addition, the post weld heat treatment of LBW Ti1023 has not been proposed yet. Thus, this study addresses this gap by presenting the following: the variety of microstructures, mechanical properties, and residual stresses found as a result of laser beam welding and post weld heat treatment in the Ti1023. In addition, the mechanical properties relationship with its microstructure is discussed. Moreover, the optimization parameters of PWHT LBW Ti1023 for the mechanical property improvements are proposed. Because of this work, the future extended application of Ti1023 is excepted.

2. Experimental Procedure

2.1 Material

The Ti1023 blocks with the following dimensions: 140mm × 58mm × 46mm (length × width × thickness) were received from the North American Alloys. The chemical compositions of these blocks met the chemical requirements (see Table 1.1) of TIMETAL 10-2-3 (Titanium Metals Corporation of America). The microstructure and microhardness of these Ti1023 blocks are presented in chapter 3. Next, these blocks were sliced into 1.6mm thick sheets by wire electro-discharge machining (EDM).

2.2 Laser Beam Welding

Before the welding process, the cut sheets were cleaned with ethanol and metal brush to remove contaminations. LBW was executed at Auckland University of Technology, Auckland, New Zealand. Several parameters were set up and kept constant for this LBW process. The power and spot size of this laser was set at 1.2kW and 0.6mm, respectively. For preventing the oxidation of Ti1023 during welding, the Ar gas was used as a protective and shielding atmosphere at 10-35L/min. Also, the beam travel speed was constant at 150cm/min. After the sheets were welded, the flat tensile test dog-bones were cut perpendicular to the welding direction (welding line) according to the ASTM E8 standard. These ASTM E8 samples met the requirements of tensile test

(more details in the chapter 2.5.2). Additionally, the material on the sides of the dog-bone sample was used for microstructure observation and microhardness measurements. A schematic diagram with the lay-out of the welded path, microstructure and mechanical properties samples is shown in Figure 2.1.

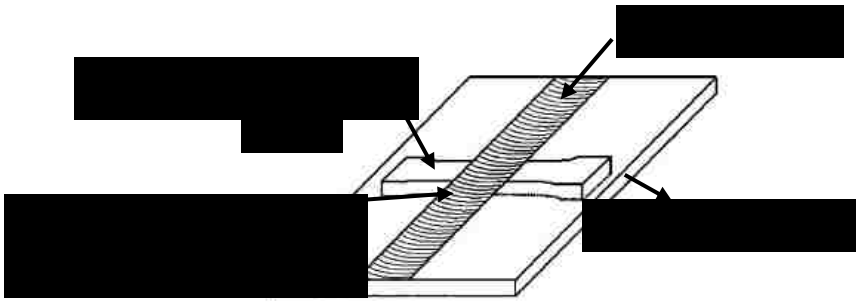

Figure 2.1: Schematic diagram shows welding sheet and the specimen location for tensile test and optical microscope [33]

2.3 Post Weld Heat Treatments

As it was concluded from the previous literature review, the reduced mechanical properties from welding can be improved by PWHT. In addition, the Ti1023 phase diagram (Figure 1.13) showed that the primary α (α_p) and secondary α (α_s) were formed in different heat treatment temperature range. In order to investigate how does the α_p and α_s affect the mechanical properties, two subgroups of PWHT parameters were planned in this research: annealing+aging and aging. The whole heat treatment conditions are shown in the Table 2.1. The rational for designing heat treatment conditions is explained in this section. The heat treatment was processed in a sealed Lindberg/Blue M^{TM} tube furnace. In addition, this tube furnace was purged with the Ar

gas during whole heat treatment process in order to provide protective atmosphere and avoid any oxidation.

2.3.1 Annealing+Aging

In this subgroup of experiments, because the annealing step forms the α_p phase and the aging forms the α_s phase, the final microstructure of this subgroup was expected to contain both α_p and α_s. In Comparison to the as-welded and only aged conditions, this subgroup might show more balanced properties. In addition, the heat treatment temperature can-not be higher than the β-transus (800^{o}C). Moreover, no matter if in the annealing (700-780^{o}C) or in aging (400-550^{o}C), the higher heat treatment temperature between these two ranges was excepted to contribute obvious results. For example, the amount and rate of the formed α_p on the 780^{o}C is higher than it on the 700^{o}C. And, the amount and rate of the formed α_s on the 550^{o}C is higher than it on the 400^{o}C. In addition, the upper limit temperature (780^{o}C) was not chosen due to avoid the β phase transformation. Therefore, the samples of this subgroup were annealed first at 750^{o}C for 1 hour. The reason for selection of 1 hour was an expectation to limit the amount of α_p phase. Because of the known and fixed alloy compositions, the total amount of α phase is constant. So, more α_p means less α_s. In addition, 1 hour annealing provided the ability to control the aging effect. Then, the water quenching of the samples to the room

temperature right after taking them out from the furnace was applied. Next step was aging at 500°C for 2.5, 4, and 8 hours, separately. It was followed by the air cooling to room temperature. Thus, a relationship between hardness and aging time can be developed. Finally, the optimization parameters could be found. At last, a sample, which went only through 750°C annealing for 1 hour, was prepared for observations of the only α_p microstructure and its mechanical properties.

2.3.2 Aging

Because the aging treatment forms the α_s phase, this microstructure was excepted to result high mechanical properties. Additionally, in order to keep the α stabilizers from forming α_s and without forming any α_p, only aging at 500°C was designed. Therefore, the specimens of this subgroup were exposed to aging at 2.5, 4, and 20 hours, separately. The same as in the previous subgroup, a relationship of hardness and aging time can be established., and the optimization aging time can be found.

Table 2.1: Post weld heat treatment temperatures and times designed after laser beam welding

	Named	Annealing Temperature (°C)	Annealing Time (hours)	Cooling Method	Aging Temperature (°C)	Aging Time (hours)	Cooling Method
	As-welded	-	-	-	-	-	-
Annealing +Aging	750°C-1hr	750	1	Water	-	-	-
	750°C-1hr +500°C-2.5hr	750	1	Water	500	2.5	Air
	750°C-1hr +500°C-4hr	750	1	Water	500	4	Air
	750°C-1hr +500°C-5hr	750	1	Water	500	5	Air
	750°C-1hr +500°C-8hr	750	1	Water	500	8	Air
Aging	500°C-2.5hr	-	-	-	500	2.5	Air
	500°C-4hr	-	-	-	500	4	Air
	500°C-5hr	-	-	-	500	5	Air
	500°C-6hr	-	-	-	500	6	Air
	500°C-10.5hr	-	-	-	500	10.5	Air
	500°C-20hr	-	-	-	500	20	Air

2.4 Microstructural Characterization

The microstructure evaluation of these samples was an important factor that influenced their mechanical properties. Therefore, the first analysis of this work was to characterize their microstructure. The light optical microscope (LOM) and scanning electron microscope (SEM) were used in this study. From these observation, not only the morphology can be presented, but also the volume fraction and grain size can be measured.

2.4.1 Specimen Preparation

Before observing the microstructure, the samples should be prepared by the following steps. It started from mounting the samples and then grinding with 320, 400, and 600 SiC grit paper. Next, the samples were polished with 6, 3, 1, and 0.25μm

diamond abrasive. Between each grinding and polishing, the cotton, water, and ethanol were used to clean and dry the surface of the samples. To reveal the microstructure, the specimens surface should be etched for 20~25 seconds by Kroll's reagent which was mixed with 100ml water, 6ml HNO_3, and 3ml HF.

2.4.2 Light Optical Microscope

The Olympus BH-2 light optical microscope with Pax-it imaging camera and software were applied to reveal the microstructure of all samples. From this LOM images, several important information can be extracted. First, the morphology of both α and β phases can be established. Especially among the beta alloys, the shape and distribution of the α phase can affect the mechanical properties, such as hardness and ductility. Second, the volume fraction of the α phase can be defined. The point counting method (ASTM E562-02) was used with these LOM images. At least five random images were selected from each zone of every samples. Third, the grain size of the α phase was measured. Ten random selected α grains from the same five images were measured. Thus, this gave a total of fifty size measurements for each zone of interest.

2.4.3 Scanning Electron Microscope

In Comparison to the resolution of LOM, the α_s was too fine and could not be

observed by standard LOM. Thus, scanning electron microscope (SEM) can help to provide this observation. The Hitachi 4300SE was used to identify the α_s phase. In addition, the morphology of both α and β phase can be observed at higher magnification.

2.5 Mechanical Property Characterization

The value of the mechanical properties indicates the macro view of microstructure. Also, the industry requirement is to have these data for the product designed references. In this study, the hardness and tensile strength of as-welded and PWHT LBW Ti1023 were tested for characterize their mechanical properties.

2.5.1 Microhardness Profiles

The hardness shows the material's resistance to deformation when localized force is applied. Before this test, the specimen surface was ground, polished, and cleaned as in the above procedures. The Leco Microhardness Tester LM248AT with 300g load and 13 seconds dwell time were used. The Vickers microhardness indentation diagonal size is about 40μm, which allows individual indentation area to be tested in three characteristic welding zones. From BM to BM across the HAZ and FZ, at least twenty indents were tested to plot hardness profile of each specimen. Also, the hardness of each zone was averaged to present its hardness.

2.5.2 Tensile Testing

The flat dog-bone (ASTM E8) were prepared for tensile testing to measure the yield strength (YS), ultimate tensile strength (UTS), and elongation (EL). A 30kN 5567 tensile testing machine with an Instron digital image correlation system and software was used in this test. The welds were located in the middle of the specimen and perpendicular to the tensile direction.

2.6 Residual Stress Measurement

In this experiment, the PANalytical Empyrean X-ray diffractometer with copper x-ray tube was used to identify the composition phases and then to measure the residual stress. For the incident beam conditions, the divergence slit was $\frac{1}{4}°$ and the mask was 2mm. As for the diffracted beam conditions, the soller slits was 0.04 radians and the fixed anti-scatter slit (FASS) size was 7.5mm. This measurement began with the wide range (30°~130°) of diffraction angle for the characteristic BM, HAZ, and FZ zones of the studied material. First, the diffraction patterns were expected to confirm the presence of the α and β phase of Ti alloy. The HighScore software was applied to identify the crystallographic peaks. Also, the diffraction peaks located at the high angles range were visible due to the presence of residual stress. These measurements were clearer for the higher diffraction angles. In addition, the variety range of Pulse Height

Discrimination (PHD) was tested in order to obtain clearer diffraction peak (higher peak/background ratio). Second, residual stress measurements were executed by $\omega - d_{hkl}sin^2\Psi$ method and PANalytical Empyrean, and then calculated by Stress software. All stress scans were performed in the range of 5° around the chosen high angles diffraction peaks which were measured from the previous steps. Moreover, 13 scans were executed with different positive and negative Ψ tilt for each sample.

3. Results and Discussion

3.1 As-welded: Laser Beam Welding of Ti1023

In this study, the microstructure and mechanical properties of as-welded condition are first revealed. The objective of this research was to establish the baseline knowledge about welded material, which would be the basis for development of the PWHT strategy as well as the reference information for future comparisons to the PWHT results.

3.1.1 Microstructure Observation

Three microstructure zones of as-welded specimen are present under the microscopy observation. First of all, the light optical microstructure of base material (BM) is shown in Figure 3.1. This image reveals the bimodal (spherical and lath) distribution of primary α phase (bright phase) dispersed in a matrix of β phase (gray phase). Also, the volume fraction and average size of α phase were determined to be 40.1±3% and 5.3±4μm, respectively. For more details of the size distribution, the analysis can be based on the division of α phase into two groups based on their morphologies. Thus, the size of spherical and lath primary α were measured to be 1.6±0.9μm and 9.0±1.8μm, respectively. The spherical primary α provides the material with deformation ability and contributes to a higher ductility at a given strength [6]. The BM microstructure can be explained by the location of the Ti1023 chemical composition on the pseudo-binary Ti phase diagram (see Figure 1.4). In general, the

Ti1023 is first hot deformed in the β region and then in the α+β field. While hot deforming in the α+β field, the α begins to nucleate at the β grain boundary. In the meantime, the formed α phase is deformed and recrystallizes as the β matrix deformed structure [2].

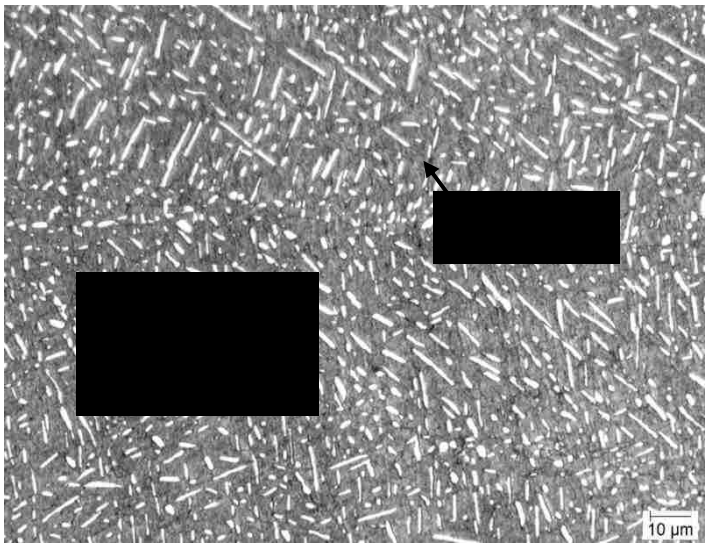

Figure 3.1: Light optical microstructure of Ti1023 base material (BM) presenting the primary α (bright area) with bimodal distribution and β matrix phase (gray area)

During the laser welding process, the heat was provided into the workpiece and increased the temperature. Generally, the temperature was high enough to form a melting pool. In other words, the temperature in the fusion zone was significantly higher than the β-transus temperature. Meanwhile, this heat also extended and gradually entered into the heat affected zone. As the laser moved out, the temperature decreased rapidly in both FZ and HAZ. Because of the wide temperature difference and fast cooling rates, the microstructures of the HAZ and FZ were expected to be different from that of the BM.

The light optical image of the heat affected zone (HAZ) is shown in Figure 3.2.

This microstructure of HAZ is characterized by spherical and lath of α phase in the β matrix. The heat from the laser source formed this microstructure. This heat partial dissolution and/or transformation of α phase into β phase occurs leading to a variation of α phase. This phenomenon is more obvious when observing the HAZ location closes to the FZ, as presented in the Figure 3.3. The volume fraction and size of α phase were determined to be 37.4±3% and 3.5±2.8μm, respectively. In addition, the primary α can be separated to spherical and lath, which were measured as 1.4±0.4μm and 5.5±2.6μm, respectively. By comparing the volume fraction and size of primary α in the HAZ and BM, the volume fraction, grain size, and standard deviations in the BM are larger than those in the HAZ, as shown in the Figure 3.4. From the microstructure observations, it is believed that the reason for this smaller standard deviation in the HAZ is the breaking up of lath particles and decreasing size of spherical particles. This result presents the range of primary α size to be wider in the BM.

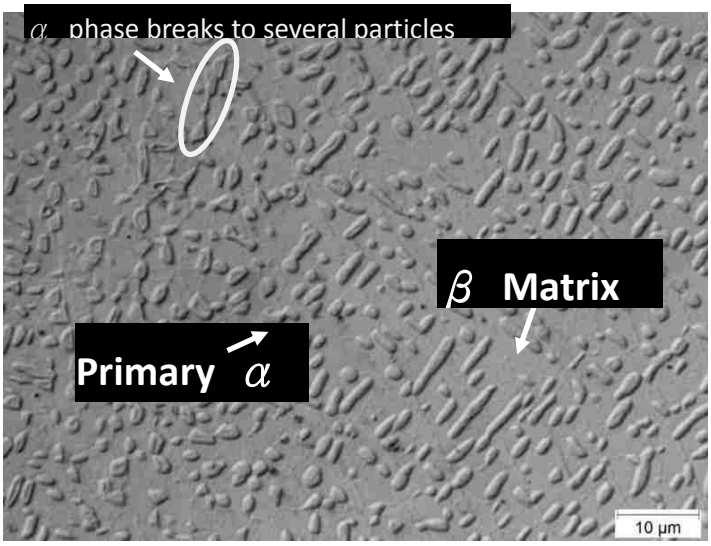

Figure 3.2: Light optical image of laser welded Ti1023 HAZ

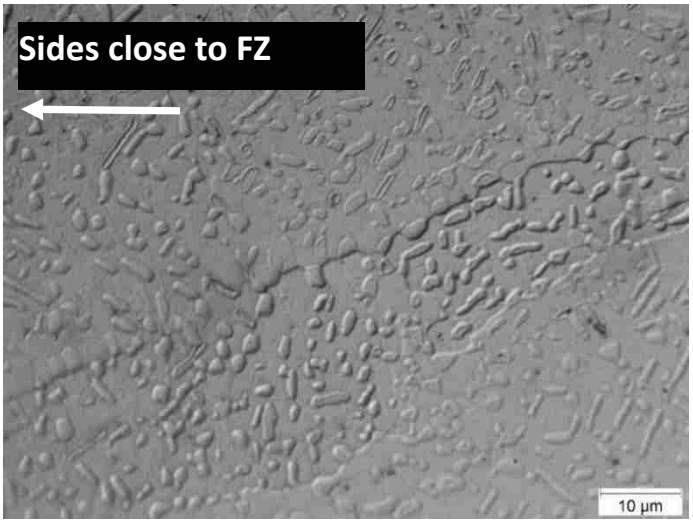

Figure 3.3: Microstructure of HAZ locations close to the FZ

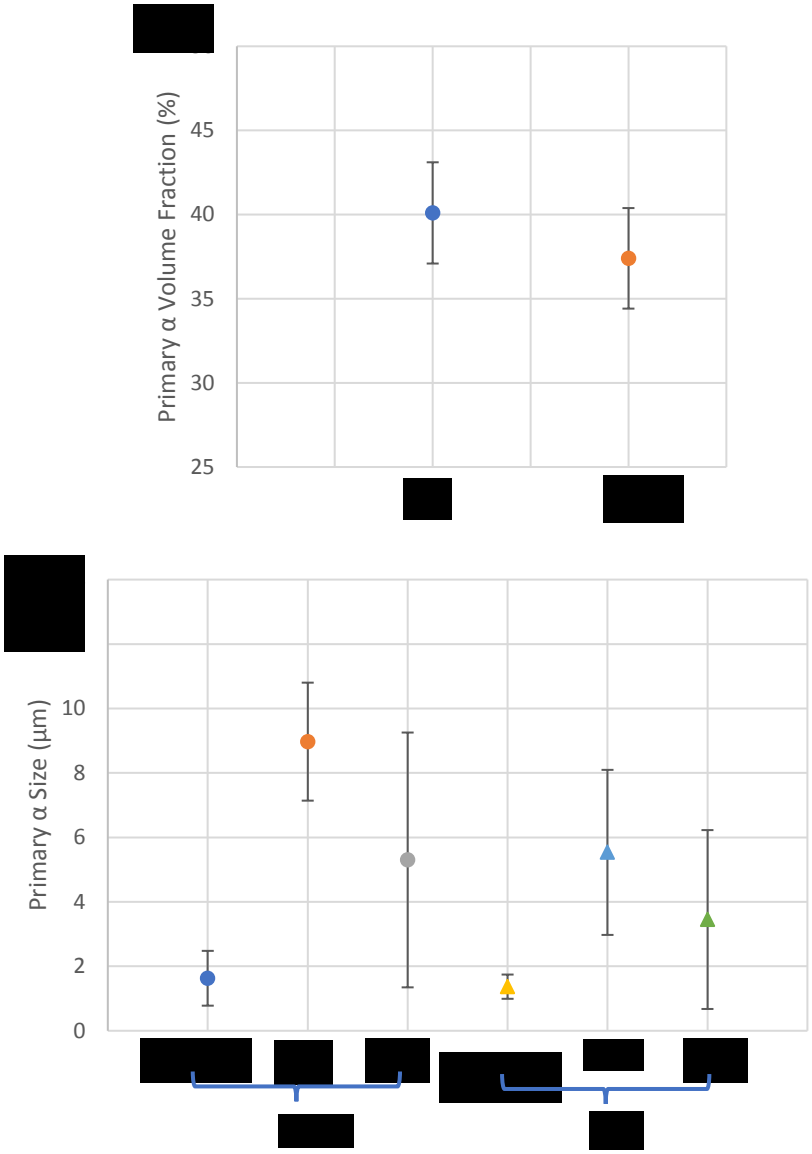

Figure 3.4: (a) The primary α volume fraction and (b) size in the BM and HAZ. The error bars show the standard deviations in the measurements

During the laser welding, a melted pool was formed when the input heat increased the temperature above melting point. Then, after the laser resource moved away, this melted pool cooled fast and solidified to form an area, which is called the fusion zone (FZ). Figure 3.5 shows the microstructure of this zone within the LBW Ti1023. In addition, Figure 3.6 and Figure 3.7 show the images of SEM and BSE within the same zone, respectively. First, it can be observed that a columnar and cellular dendritic structure was formed in the FZ on Figure 3.5. When observing the location near HAZ, the grain boundary is nearly parallel to the sample surface. By comparing, the grain boundary at the weld centerline shows vertical direction. It was also observed in the FZ of the LBW Ti64 [6]. This grain boundary geometry was strongly affected by the heat flow of weld solidification process. When laser welded, the temperature gradient resulted in the highest temperature at the weld centerline and decreased toward both sides of the BM. In contrast, as the laser source moved away, the grains solidified from both sides of the FZ toward the weld centerline. Therefore, the grain boundary near the HAZ is perpendicular to it on the weld centerline [6].

Second feature of FZ is fact that only the β phase is present in the LOM (Figure 3.5), SEM (Figure 3.6), and BSE (Figure 3.7). Also, more discussions on the present phase within the BSE images can be seen in chapter 3.2.1.1. That means all the primary α phase has transformed to the β phase and retained it at the room temperature. Two

steps caused this phenomenon. First step is the melting of the FZ, which means the temperature was higher than β-transus during laser welding. Therefore, whole grain formed the β phase in this step. Second step is fast cooling to retain the β phase. In addition, unlike the alpha or alpha+beta alloys, there is no α martensite formed of Ti1023 while cooling rapidly. This also can be explained by phase diagram [2] and Mo_{eq} [8]. From the Ti alloys phase diagram, Ti1023 is located on the right side of the martensite starting (M_s) line. That means the α martensite is suppressed in the Ti1023 no matter of the cooling rate. Besides, as reported by Bania, the Mo_{eq} of this Ti1023 is 11.45wt%, which is higher than 10wt% and without forming the α martensite.

Lastly, porosity and undercut were also observed in the FZ. Porosity is one of the defects formed during welding of Ti alloys [6]. And it also has been presented in other LBW Ti alloys, such as Ti5553 [21] and Ti6242 [20]. This is generally attributed to the gas bubbles absorbed in the melt pool which cannot be released during solidification. And, the gas may be caused by hydrogen from the workpiece surface contaminations such as grease or oil [17]. Undercut is another welding defect. During the welding, a large amount of heat was put into the material. This energy resource not only caused a melted pool, but also evaporated part of the molten metal. That resulted in the material loss phenomenon and generally it is located on the edge of the FZ.

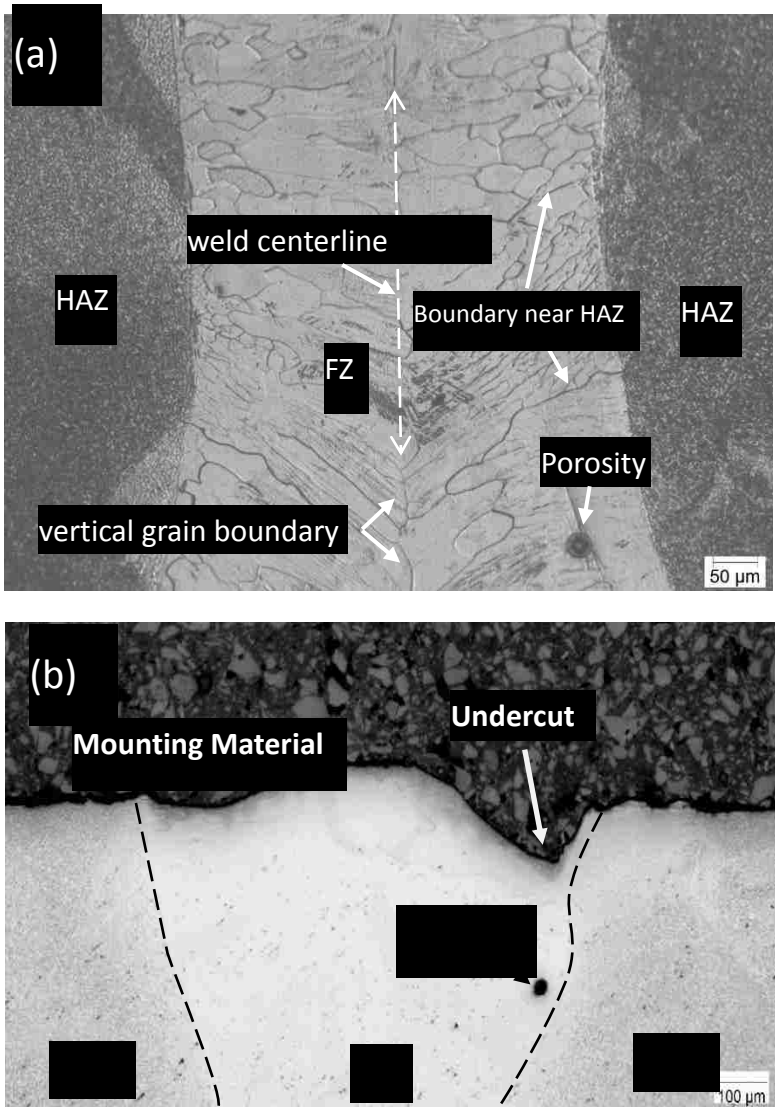

Figure 3.5: Optical micrographs showing the laser welded Ti1023 FZ and HAZ microstructures. (a) The columnar and cellular dendritic β grains and presence of porosity in the FZ. (b) The shape of FZ shows irregular edge which appears like undercut. In addition, porosity and undercut are observed in FZ

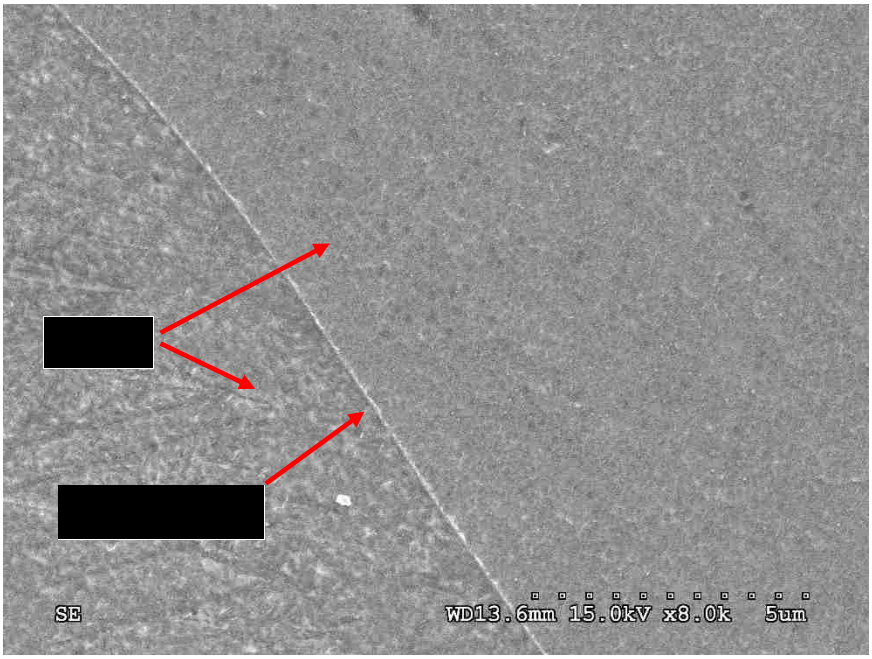

Figure 3.6: SEM micrograph of the fusion zone (FZ) of as welded material shows β phase around the grain boundary

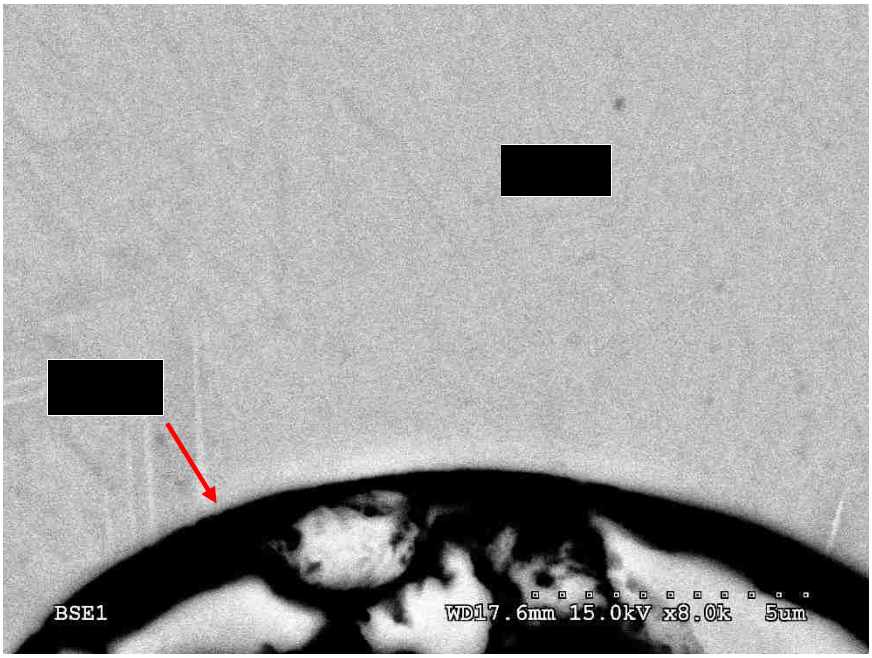

Figure 3.7: BSE micrograph of the fusion zone (FZ) of the as welded material showing β phase and porosity

3.1.2 Mechanical Properties

3.1.2.1 Microhardness Profiles

The microhardness profiles across three zones of LBW Ti1023 are plotted

in Figure 3.8. It presents that the BM hardness (363~392HV) is higher than the FZ (319~332HV) and HAZ (299~355HV) hardness. This phenomenon can be explained by the above microstructure observation. The BM structure contains higher primary α volume fraction and lager α grain size than that of the other two zones. In addition, there is no primary α preserved in the FZ. Because the hexagonal close packed (HCP) has fewer slip systems than the body center cubic (BCC), the α phase (HCP) is harder than the β phase (BCC). Therefore, higher amount of primary α phase in the BM contributes higher microhardness. This hardness profile of LBW Ti1023 is similar to the other beta alloy (such as Ti5553), but totally opposite to the alpha+beta alloy (such as Ti64 and Ti6242). This also can be explained by its microstructure. In the FZ of the alpha+beta alloys, the acicular α' (α prime) martensite was formed and contributed to higher hardness [20]. According to Donachie [6], this α' (α prime) martensite formed in alpha and alpha+beta titanium alloys because of β decomposition by a martensite reaction while cooling rapidly.

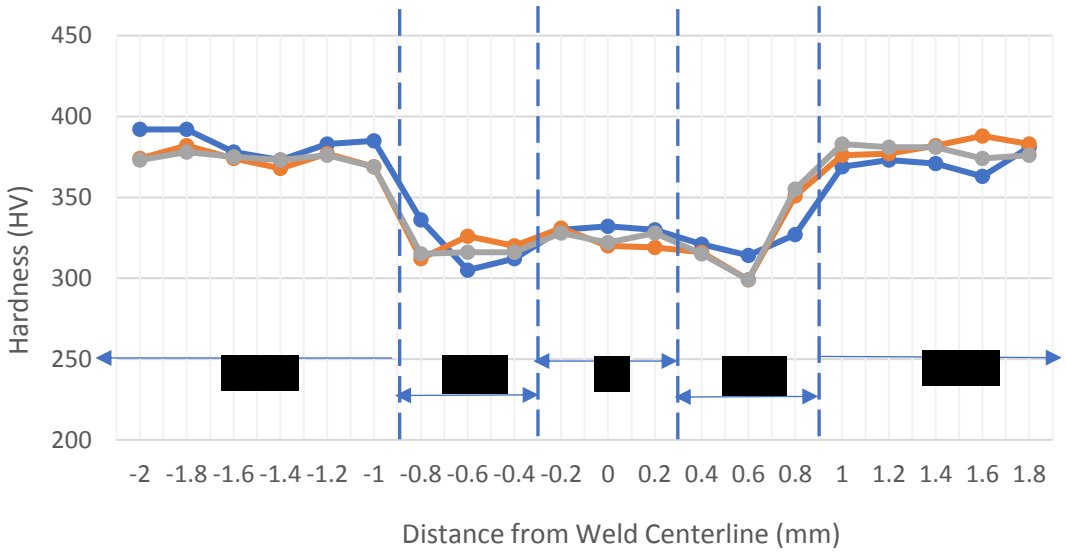

Figure 3.8: Microhardness profile across the weld on the laser welded Ti1023.

3.1.2.2 Tensile Testing

Before conducting the tensile testing, the light optical image of the weld within the tensile test specimen was taken and it is shown in Figure 3.9. Then, the tensile properties of as-welded Ti1023 were measured and are presented in Table 3.1. In order to compare the effect of the laser-welding, the tensile properties of the as-received material (BM) were also provided in Table 3.1. The YS, UTS, and total elongation of the as-laser welded samples were 834MPa, 934MPa, and 1.8%, respectively. When comparing to BM (without welding), these properties are lower. In addition, by investigating the strain map of the tensile testing sample (Figure 3.10; the various colors specify different strains), it showed that the maximum strain is located in the FZ and HAZ. Moreover, when observing the specimen after tensile test, the fracture is located within the FZ. Thus, between these three zones of the as-welded specimen, these

reduced tensile properties can be attributed to the FZ. Several factors were considered and observed in the FZ. First is the microstructure change. Only β is formed in the FZ and results in lower hardness. According to Boyer, the UTS decreases as the hardness decreases [1]. Thus, it is expected that the YS and UTS is lower than in the BM. In addition, because the spherical primary α provides higher ductility [6], lack of spherical α particles results in lower elongation in the FZ.

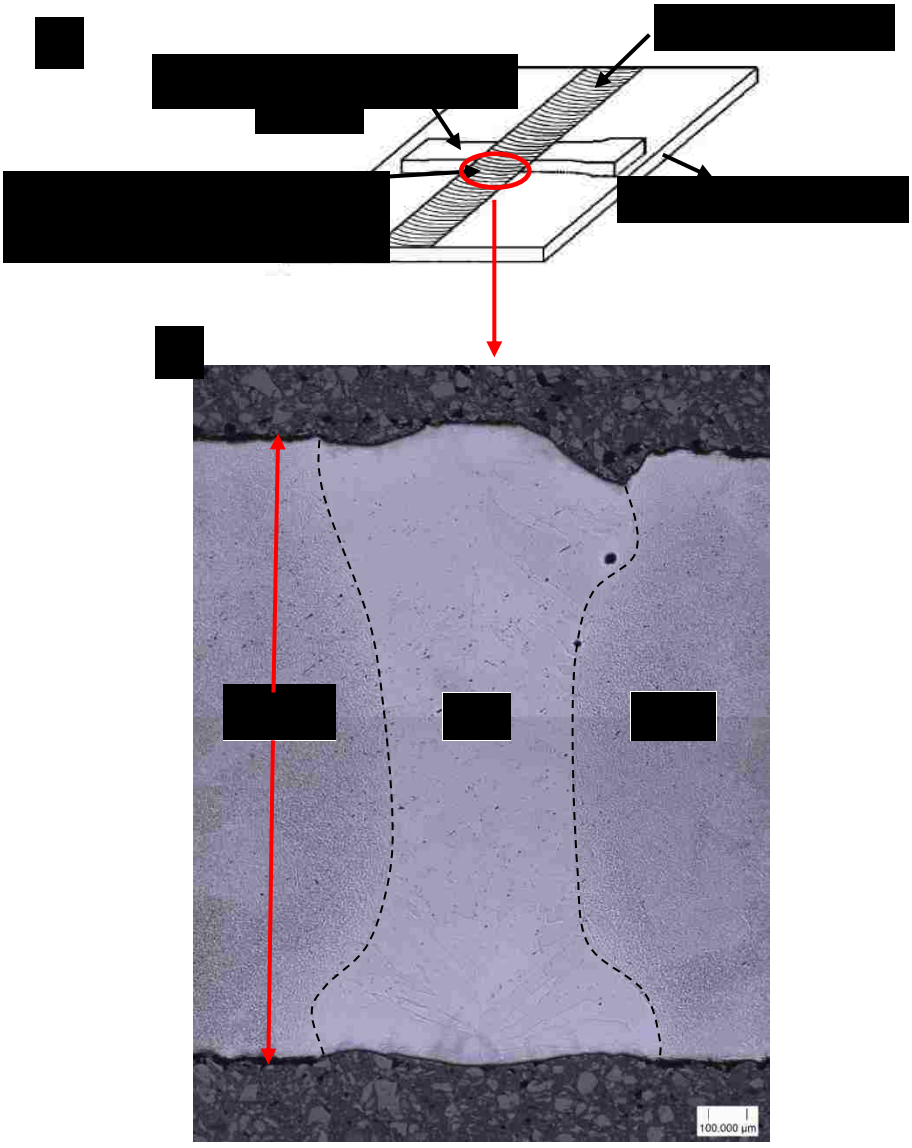

Figure 3.9: (a) Location and orientation of the tensile test specimen containing weld. [33] (b) The light optical image of the weld within the tensile test specimen.

Table 3.1:
Tensile properties of the as-laser welded Ti1023 compared to the BM.

Conditions	Yield Strength (MPa)	Ultimate Tensile Strength (MPa)	Total Elongation (%)
As-laser welded	834	934	1.8
As-received (BM)	1106	1239	4

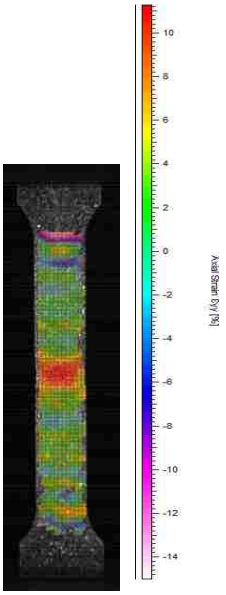

Figure 3.10: Strain map of the sample during tensile testing. The different colors specific strains

3.1.3 Residual Stress

The residual stress measurement began with the composition phases identification. The X-ray diffraction pattern of LBW Ti1023 base material is shown in Figure 3.11. It can be observed that the diffraction peaks at the smaller diffraction angles are stronger than those at the higher diffraction angles. This situation can be explained by the intensity equation [34]:

$$I_{(hkl)} = \left|F_{(hkl)}\right|^2 M_{(hkl)} Lp_{(hkl)} \qquad \text{Equation 3.1}$$

Where, $F_{(hkl)}$ is the structure factor which including temperature effects,

$M_{(hkl)}$ is multiplicity for reflection hkl, $Lp_{(hkl)}$ are Lorentz and polarization factors. The above three factors decreased with increasing diffraction angle. Thus, the diffraction intensity is lower at the higher diffraction angles.

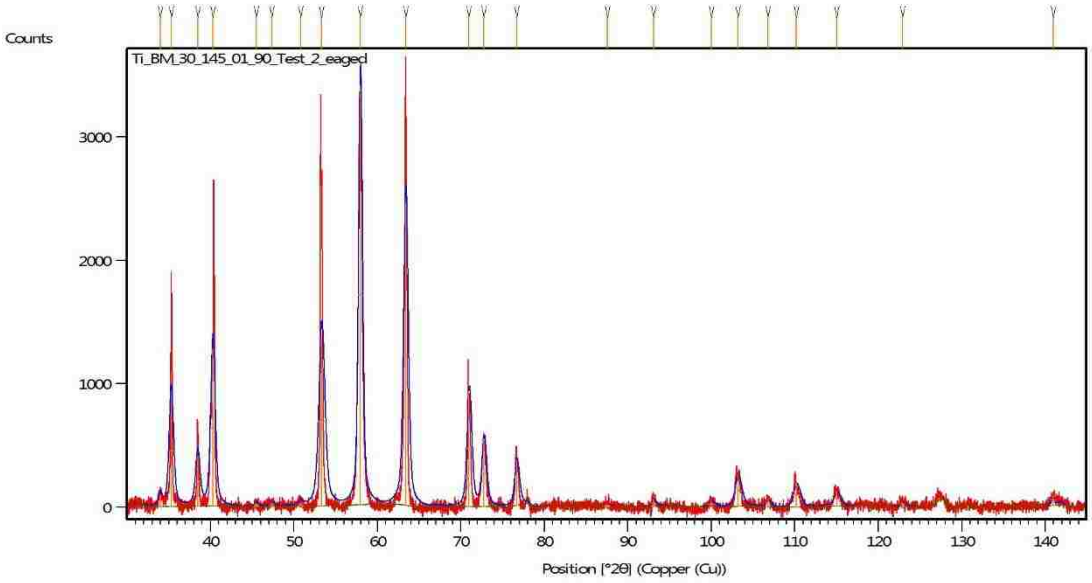

Fig. 3.11: The X-ray diffraction pattern of LBW Ti1023 base material

In order to improve the ratio of diffraction peak to the background signal, different range of Pulse Height Discrimination (PHD) was tested as shown in Figure 3.12. It can be observed that both, the peaks and the background signal intensity decreased from 600 to 100 counts when the PHD range was applied decreasing from 25~75 to 55~75. Thus, the 55~75 PHD was chosen to test the following measurements due to the fact that the ratio of the diffraction peak to the background signal is highest for these PHD ranges.

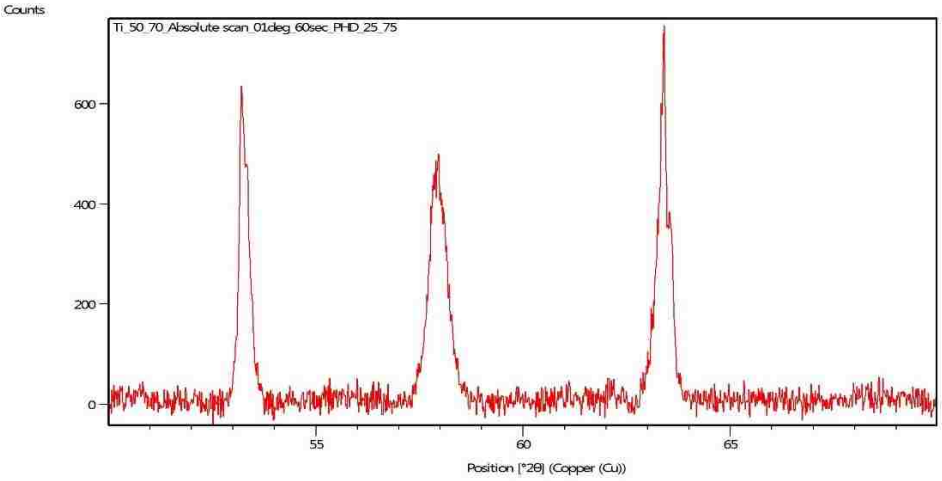
Counts
Ti_50_70_Absolute scan_01deg_60sec_PHD_25_75
600
400
200
0
55
60
65
Position [°2θ] (Copper (Cu))

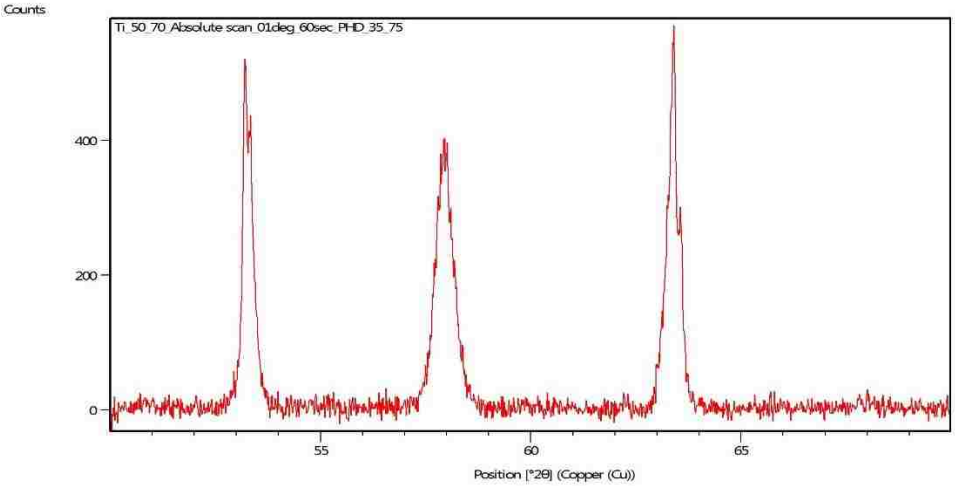
Counts
Ti_50_70_Absolute scan_01deg_60sec_PHD_35_75
400
200
0
55
60
65
Position [°2θ] (Copper (Cu))

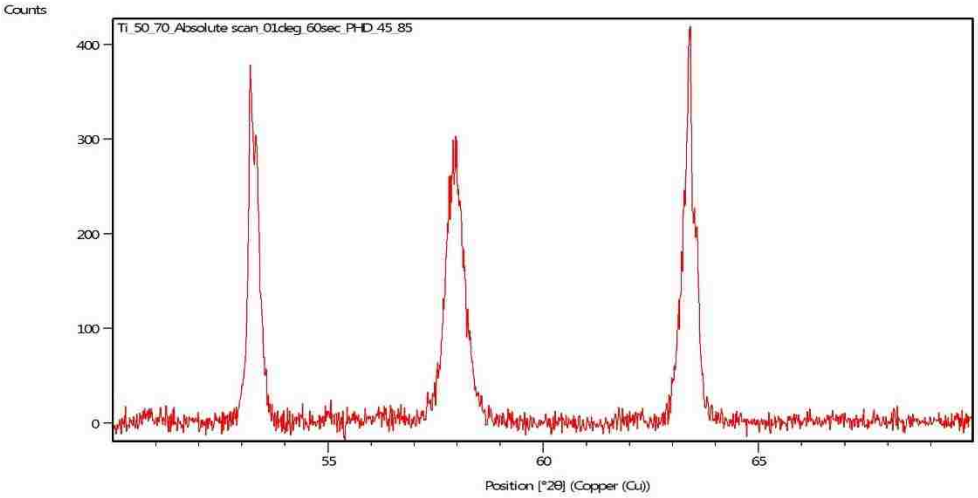
Counts
Ti_50_70_Absolute scan_01deg_60sec_PHD_45_85
400
300
200
100
0
55
60
65
Position [°2θ] (Copper (Cu))

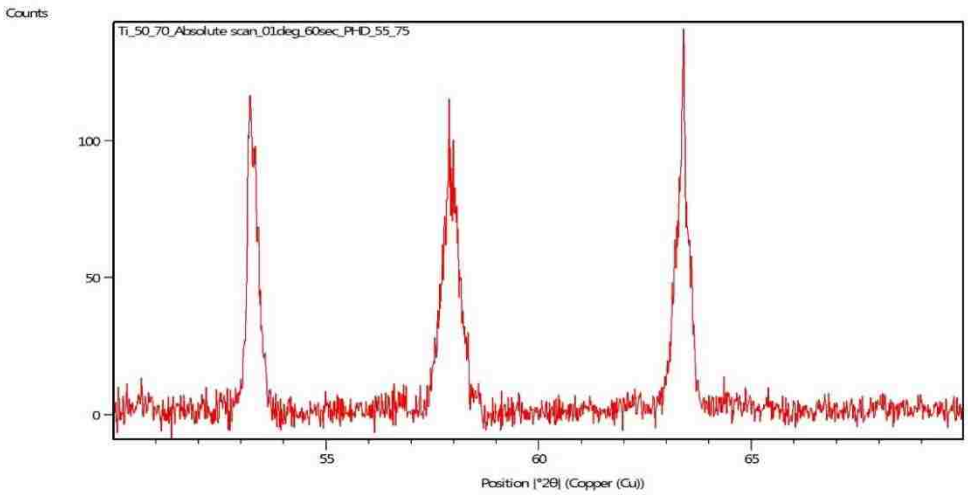

Figure 3.12: The diffraction results for different ranges of Pulse Height Discrimination (PHD), (a) 25~75, (b) 35~75, (c) 45~75, (d) 45~85, (e) 55~75

After PHD range optimization, Standard Bragg-Brentano diffraction was done for three zones of the sample surface. The diffraction pattern of Ti1023 as-welded BM is shown in Figure 3.13. The diffraction peak is pointed and pronounced and it does match the Ti diffraction pattern from the International Center for Diffraction Data [35]. Several peaks match the Ti β phase (Body-Centered Cubic, BCC) which are shown in Table. 3.2.

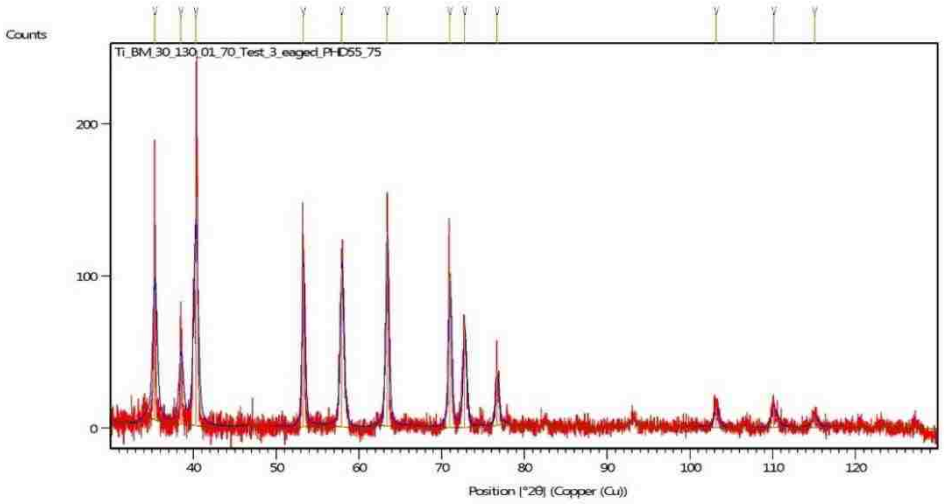

Figure 3.13: The diffraction pattern of the Ti1023 as-welded BM

Table 3.2: The diffraction pattern of Ti β phase (BCC)

				Diffraction line position for		3.3063
No	Dif. Line			Sin O	Angle	2Theta
	h	k	l		[rad]	[deg]
1	**1**	**1**	**0**	0.3298	0.33605	38.51
2	**2**	**0**	**0**	0.4664	0.48516	55.60
3	**2**	**1**	**1**	0.5712	0.60792	69.66
4	**2**	**2**	**0**	0.6595	0.72018	82.53
5	**3**	**1**	**0**	0.7374	0.82916	95.02
6	**2**	**2**	**2**	0.8077	0.94032	107.75
7	**3**	**2**	**1**	0.8725	1.06022	121.49
8	**4**	**0**	**0**	0.9327	1.20184	137.72
9	**4**	**1**	**1**	0.9893	1.42426	163.21

For as-welded material, the diffraction patterns of the HAZ and FZ were also measured and are shown in Figure 3.14 and 3.15, respectively. Based on data presented in Figure 3.13-15, a comparison of the experimental diffraction 2θ positions with the International Center for Diffraction Data [35] is shown in the Appendix A.1. Several results are presented in this appendix. First, the phase analysis shows that all three zones contain both the α and β phases. Second, comparing to the reported in literature α and β peak positions [6], the 2θ positions for our three zones are shifted. For example, the (110) of Ti β is reported at 38.51°, however, the measured results for our material show that the peak is presented at 39.25° for the BM, 39.27° for the HAZ, and 39.31° for the FZ. This is attributed to the different chemical compositions of the

reference and actually studied samples. In other words, these samples contain variation of α and β phase. These results of mixed phases can also be observed at the microstructure images. There are different α and β volume fractions in each sample. Thus, the lattice parameters for both phases are distorted and this contributes to the 2θ positions shift. Last, there are α peaks, which still can be observed in the FZ. Because only β phase exist in the FZ, this situation can be attributed to the fact that the X-ray scans are generated from too large areas, which cover part of the HAZ and BM zones as well. Thus, the solution is to use the cross-section sample to make sure that only FZ or BM can be detected, as it is presented in a schematic diagram shown in Figure 3.16.

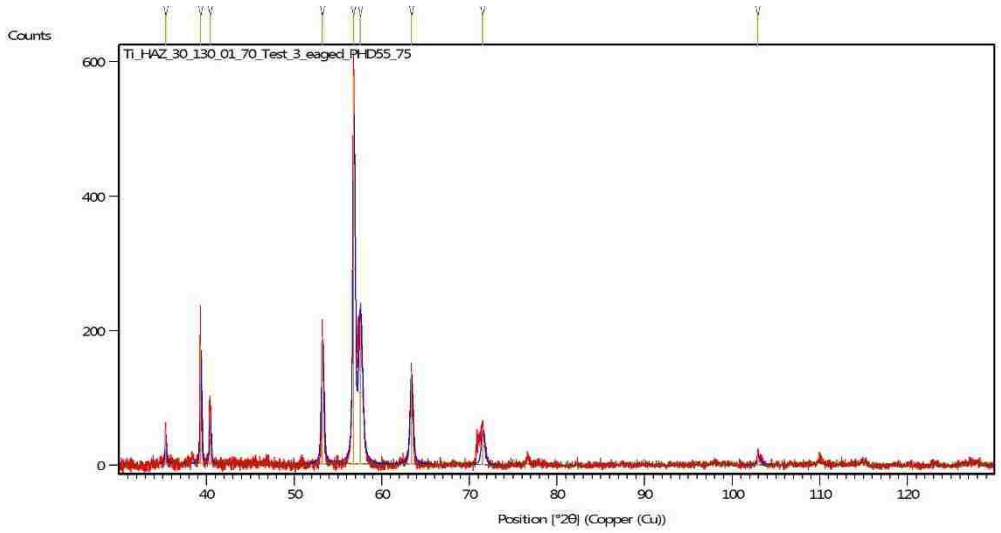

Figure 3.14: The diffraction pattern of Ti1023 as-welded HAZ

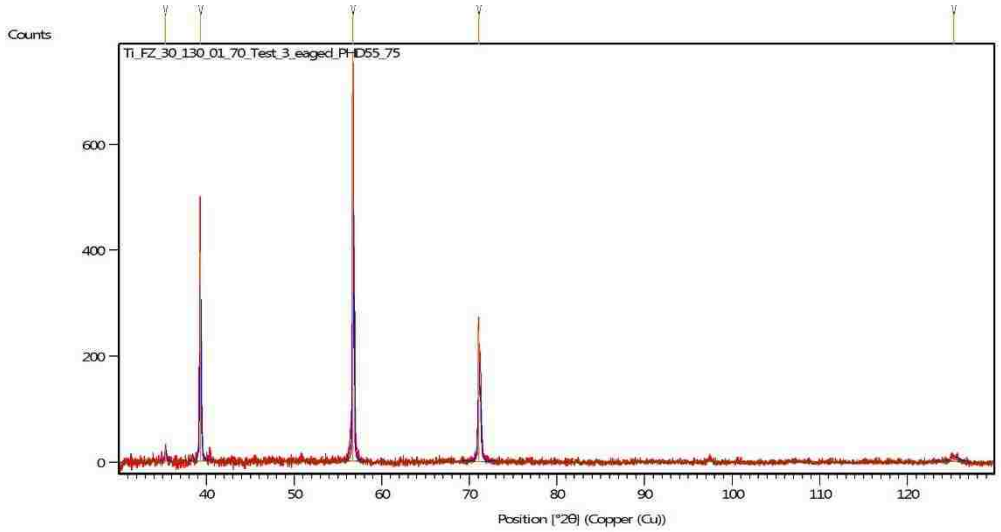

Figure 3.15: The diffraction pattern of Ti1023 as-welded FZ

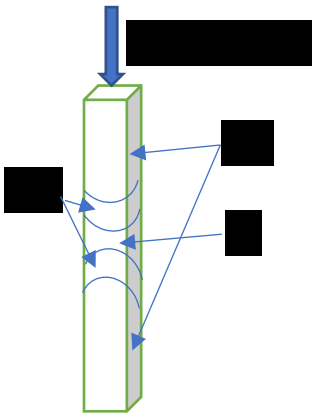

Figure 3.16: Schematic diagram of the observed location of sample cross section

The cross section of FZ was tested with a normal X-ray scan speed in the first time. However, the diffraction pattern was very weak and not clear. The reason for that was very small the scan area of cross section (6x1.6mm^2). Thus, the effective signal is weaker and it is more difficult to present the obvious, expected peaks. To improve this situation, the scan speed was doubled. The detected results for higher speed are shown in Figure 3.17. Next step was to find a peak which is used for further residual stress

measurements. Because the residual stress is more obvious at high diffraction angle, a short angle range between 120~130 was chosen and measured the diffraction pattern (shown in Figure 3.18). According to this result, a peak at 125.63° is presented. Also, its intensity is still very weak. Next, thirteen diffraction patterns were obtained from these measurements and are presented in Figure 3.19. Finally, the stress analysis software of PANalytical has been applied to identify and calculate the residual stress. The final results are plotted in Figure 3.20. Based on the performed measurements, the residual stress of Ti1023 laser as-welded FZ is calculated as 221.3±228.5 MPa.

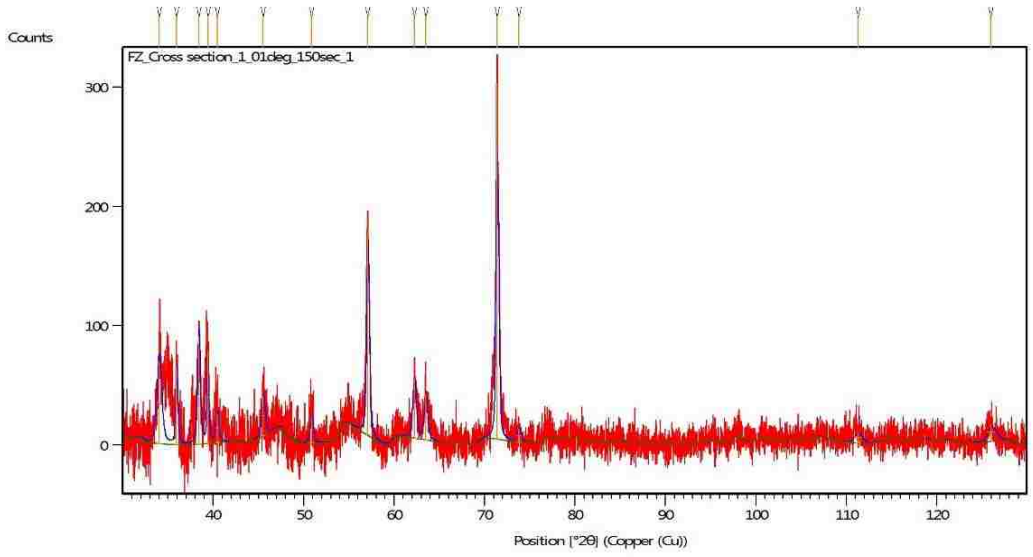

Figure 3.17: The diffraction pattern of Ti1023 as-welded FZ cross section with a longer scan speed

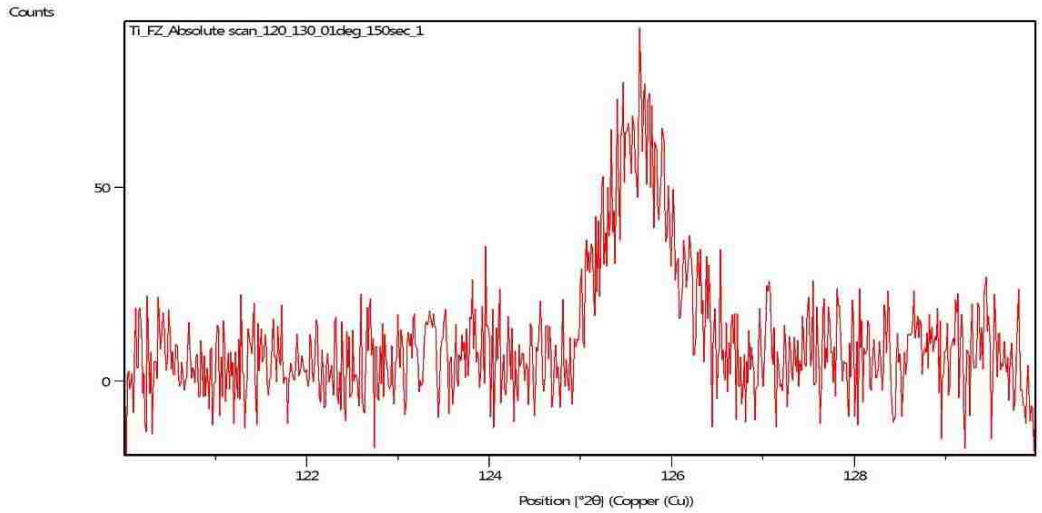

Figure 3.18: The diffraction pattern of Ti1023 as-welded FZ cross section in the detecting angle between 120° and 130°

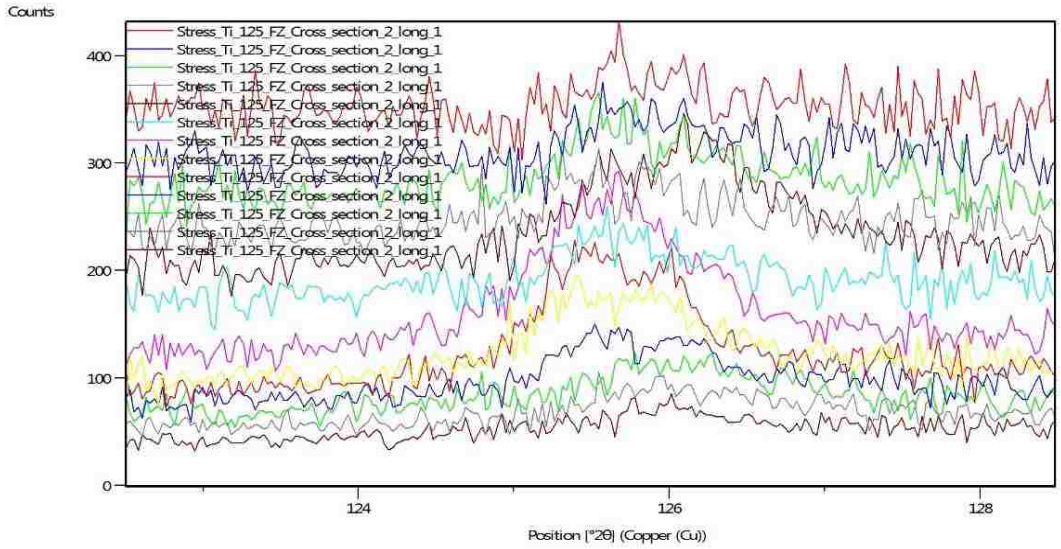

Figure 3.19: The residual stress measurements of the diffraction pattern for Ti1023 as-welded FZ cross section

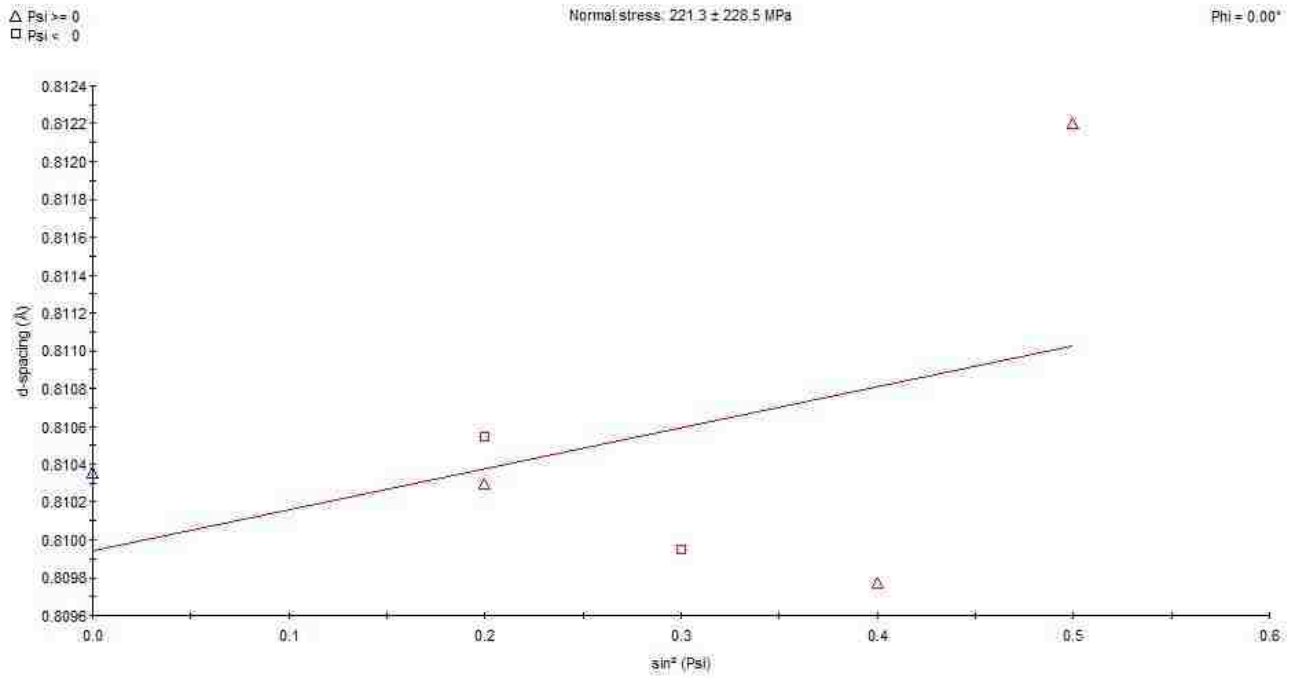

Figure 3.20: The residual stress measurement results for Ti1023 as-welded FZ cross section showing d-spacing as a function of angular ($sin^2\Psi$)

In order to compare the value of the residual stress before and after the laser welding, the diffraction pattern for BM is needed as reference. The wide diffraction angle range was measured and it is shown in Figure 3.21. Then, Figure 3.22 shows the short angle range detected and present two diffraction peaks at, 122.8° and 127.4° . Here, β phase was chosen due to this phase presented in both BM and FZ zones. Thus, thirteen diffraction patterns of the 122.8° peak (β phase) are detected and shown in Figure 3.23. And the stress software calculates the residual stress (Figure 3.24) for Ti1023 BM cross section to be -63.2±19.2 MPa.

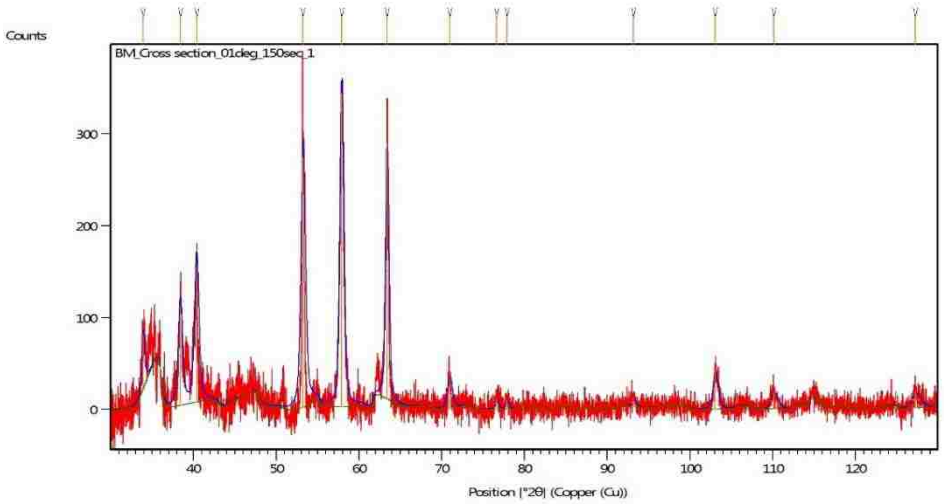

Figure 3.21: The diffraction pattern of Ti1023 as-welded BM cross section

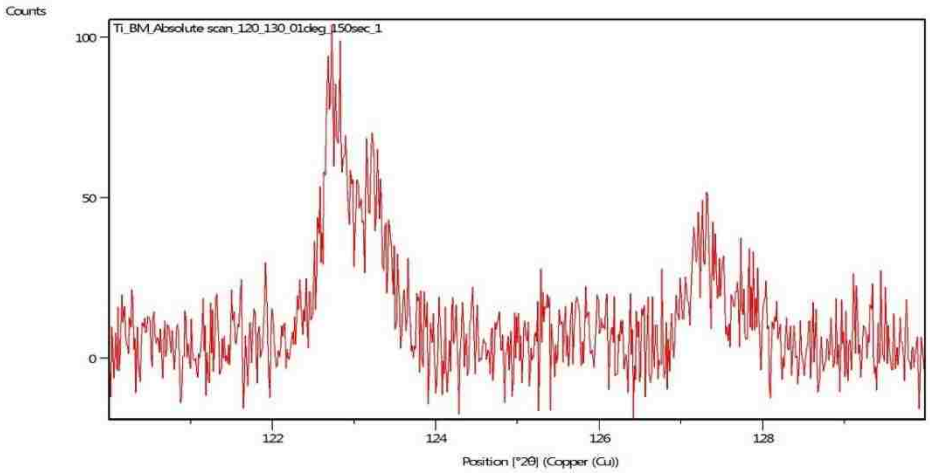

Figure 3.22: The diffraction pattern of Ti1023 as-welded BM cross section in the detecting angle between 120° and 130°

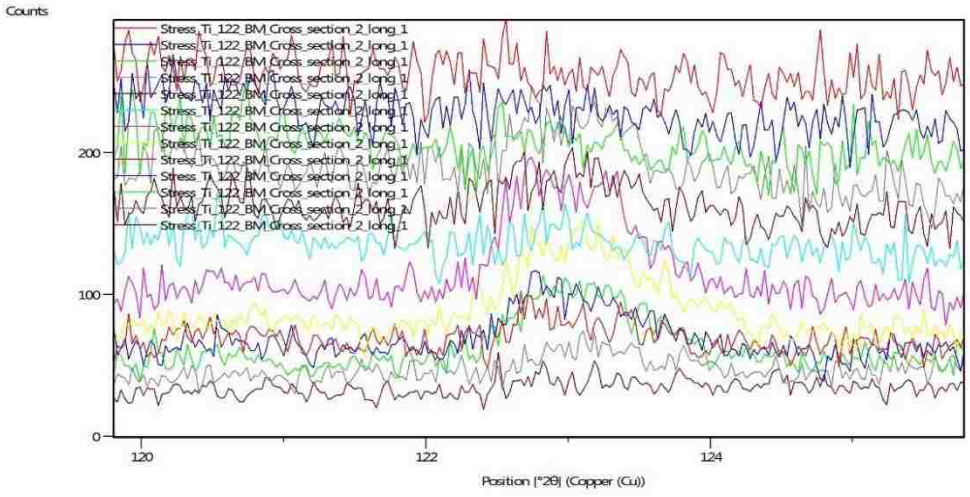

Figure 3.23: The residual stress measurement diffraction pattern of Ti1023 as-welded BM cross section

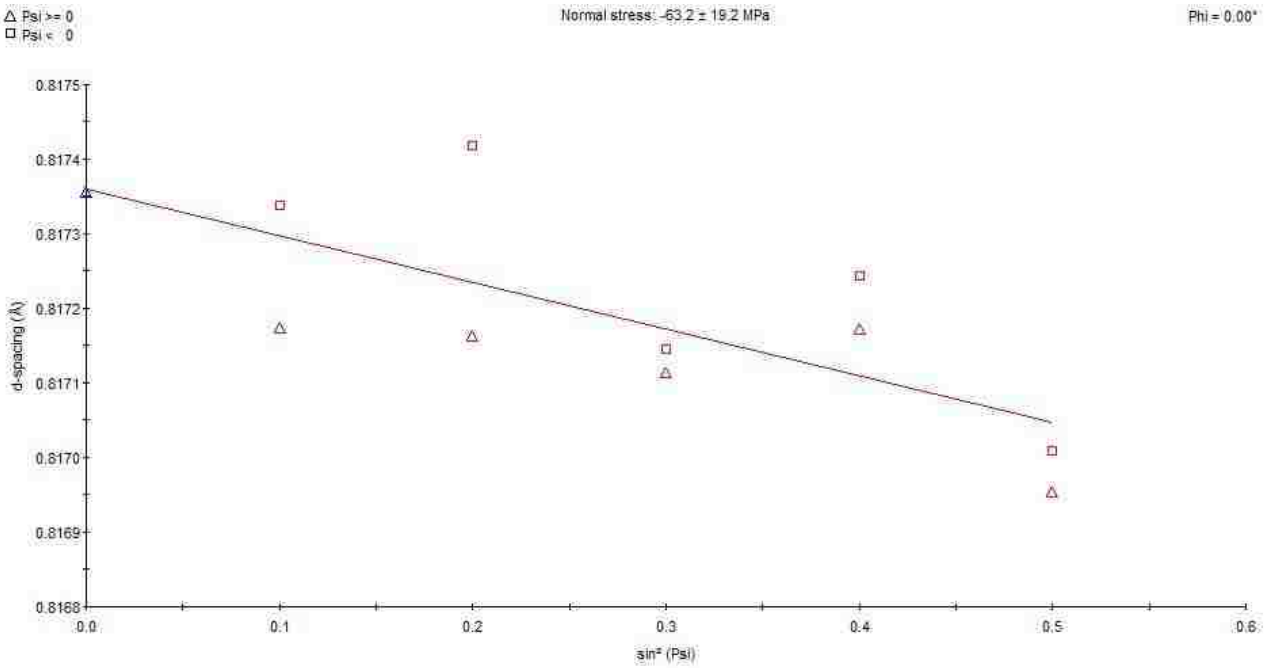

Figure 3.24: The residual stress measurement result of Ti1023 as-welded BM cross section showing d-spacing as a function of angular ($sin^2\Psi$)

By comparing the residual stress measurements of Ti1023 for as-welded BM and FZ, it can be observed that the standard deviation for both zones is too large. Thus, this result can-not represent the real residual stress condition due to only three peaks within each zone and can be identified and calculated by stress analysis software. Even though there are thirteen diffraction patterns in the Omega method measurement, most of them can-not be used due to a very weak signal. Several parameters contribute to these results: first, the detecting area (6x1.6mm^2) is too small due to the laser welding specimen preparation conditions. These parameters and laser welding features make the FZ smaller than both the BM and HAZ. In addition, in order to make sure only FZ was detected, the cross section of FZ was needed for the measurements. Thus, comparing

to the irradiated area ($57mm^2$), this detecting area only contributes 16.8% to diffraction and results in weak diffraction pattern. The second contributing parameter is the presence of a few crystallographic phases. There are α and β phase present in the BM and HAZ. The diffraction peaks of these phases may be located too close to identify them or they even overlap. In addition, due to the rapid temperature changing of the laser welding process, each α and β grain lattice distorted easily. Moreover, this bi-phase (α and β) also textures to each other. This structure further weakens the diffraction peak and complexes the diffraction pattern. As for FZ, although only β phase is present, the diffraction peaks are still weak due to the fact that cooling from laser melting is very fast and does not provide good conditions for crystal structure formation. Lastly, the residual stress was measured at the high diffraction angle. However, as it was stated before the peak intensity decreases as the diffraction angle increases. Thus, these above-mentioned factors contributed to harder reading of the residual stress measurements.

3.2 Post Weld Heat Treatment of Laser Beam Welding Ti1023

For studying the post weld heat treatment of laser beam welding Ti1023, two heat treatment designed groups has been executed: annealing+aging and aging. There are five conditions shown in the annealing+aging group and six conditions shown in the

aging group. In this chapter, the experiences of aging group are shown first because one result from them can be applied in the annealing+aging group. In addition, more details are discussed in the first post weld heat treatment condition on each group. Then, only measuring results are reported in other heat treatment conditions on each group. The overview of relationship between microstructure, volume fraction, grain size, hardness, YS, UTS, and EL for the whole post weld heat treatment conditions in this study are compared and discussed in the chapter 3.3.

3.2.1 Microstructure observation, Microhardness Profiles and Tensile Strength of the Aging conditions

3.2.1.1 Aging at 500°C for 2.5 hours

The microstructure of the base metal, heat affect zone, and fusion zone are shown in Figures 3.25-3.27. The α volume fraction of BM can be determined to be 36.3±2.7% from a micrograph presented in Figure 3.25. In addition, the spherical and lath α grain size can be measured as $6.0 \pm 1.6\mu m$ and $1.2 \pm 0.4\mu m$, respectively. Moreover, the total average α grain size is 4.5±3.5μm. Comparing to the BM of as-welded (Figure 3.1), it is obvious that the α phase morphology was modified by the heat from the aging process. In other words, the α grain showed less sharpness after aging. Furthermore, the grain boundary can be observed and some α phase even exist on this

boundary. As for the HAZ, Figure 3.26 presents a microstructure that contains spherical and lath α phase with β phase. This α phase morphology sharpness is weaker. This morphology was affected by the heat from two steps. First, the heat from laser welded process dissolved and broke up some α phase. Then, the heat from aging step tends to shape the α grains. In HAZ, the α volume fraction is 31.9±5.4%. The average α grain size is 3.8±2.8μm. When measured separately, the spherical and lath α grain is 1.2±0.4μm and 5.9±1.5μm, respectively. Figure 3.27 is the optical image of FZ. Only the β phase and its grain boundaries can be observed. However, this microstructure that contains no α phase conflicts with the Ti1023 phase diagram [9,31]. It should be formed as the fine secondary α phase in the FZ. Therefore, the scanning electron microscopy was needed and the image of FZ is shown in the Figure 3.28. Again, there is no specific α phase to be found, it only shows β grains and grain boundaries. In order to find the secondary α phase, the characteristics of α phase and a feature of back-scattered electrons image has been combined and applied. In titanium alloys, the α phase tends to be formed due to the α stabilizer (element) [2]. For example, Al is one of the α stabilizer. As for the back-scattered electrons, there is a feature which is known as atomic number contrast (or compositional contrast) [36]. To be more specific, in a flat and even metallographically polished surface, the back-scattered electrons are in certain relationship to the atomic number. For example, in a back-scattered electrons image,

regions of low atomic number will be darker than to regions of high atomic number. Thus, the back-scattered electrons image of aging 2.5 hours LBW Ti1023 FZ was taken and shown in Figure 3.29. It can be observed that the spherical dark areas are very present in the FZ. In Ti1023, the α stabilizer is Al, and the β stabilizer are V and Fe. Also, the atomic number of these elements are 13, 23, and 26, respectively. Therefore, the spherical dark area can be identified as high composition of Al. In other words, this image can be linked to the α phase. In addition, from this heat treatment temperature (500^{o}C) and this fine size, this spherical dark grain can be considered as the secondary α phase.

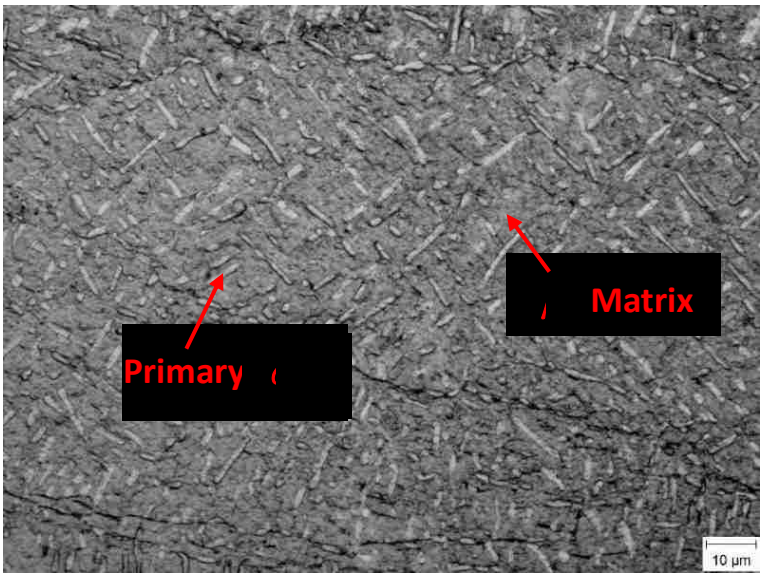

Figure 3.25: Light optical microstructure of aging 2.5 hours LBW Ti1023 base material (BM) presenting the primary α (bright area) textured in the β matrix phase (gray area)

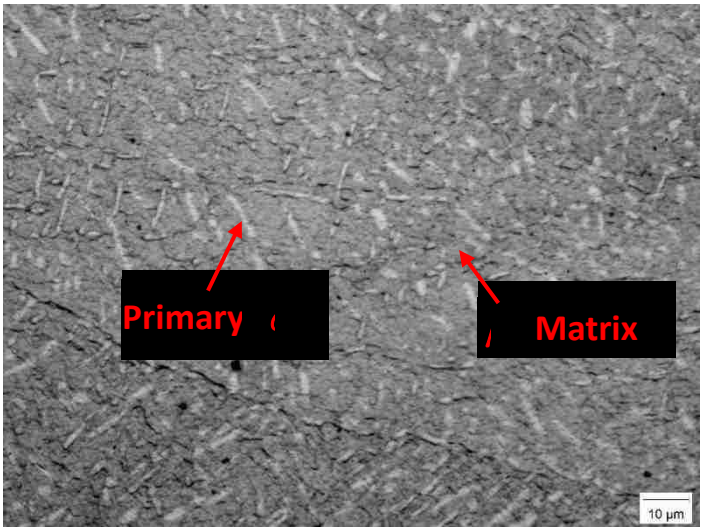

Figure 3.26: Light optical microstructure of aging 2.5 hours LBW Ti1023 heat affected zone (HAZ)

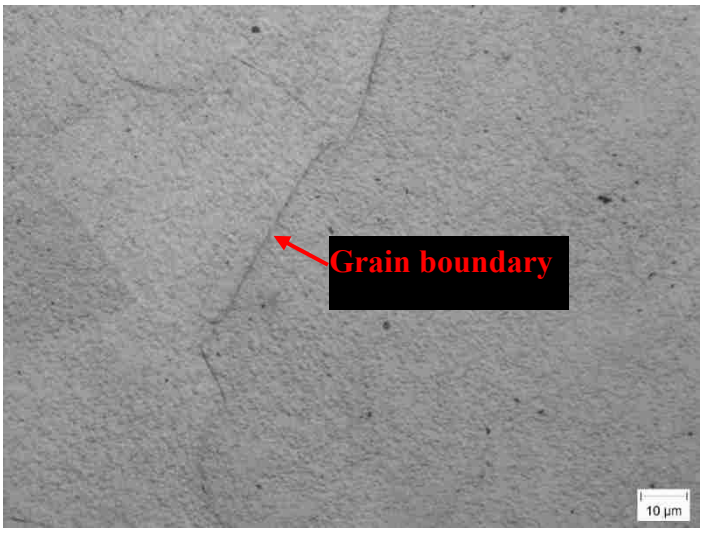

Figure 3.27: Light optical microstructure of aging 2.5 hours LBW Ti1023 fusion zone (FZ) presenting the β grain and its grain boundary

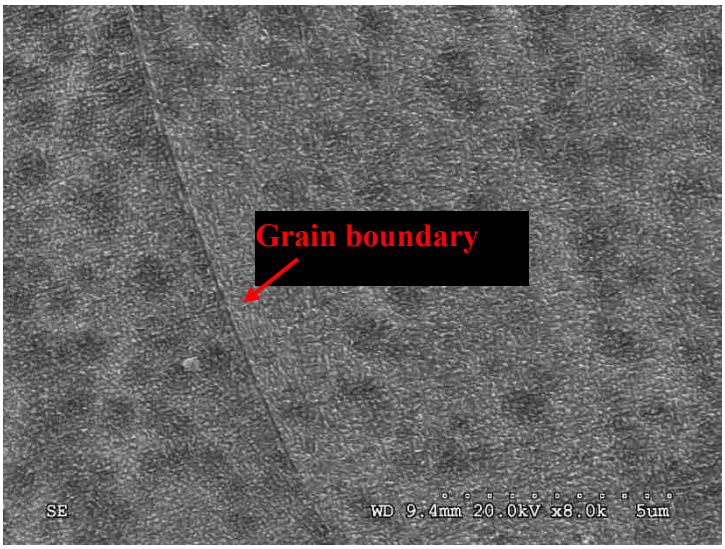

Figure 3.28: Scanning electron microscopy image of aging 2.5 hours LBW Ti1023 fusion zone (FZ) presenting the β grain and its grain boundary

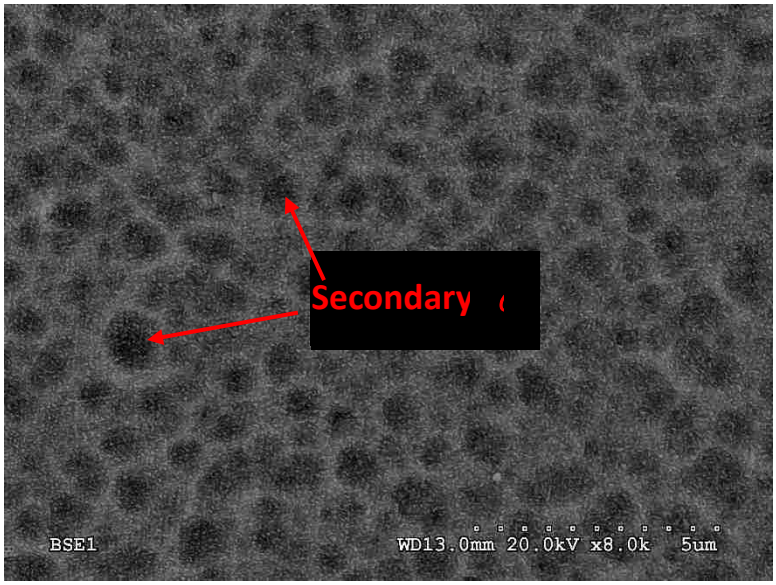

Figure 3.29: Back-scattered electrons image of aging 2.5 hours LBW Ti1023 fusion zone (FZ) is full of the secondary α phase

The hardness profile through three zones of aging 2.5 hours LBW Ti1023 is presented in Figure 3.30. The microhardness of FZ, HAZ, and BM shows 396~409HV, 380~412HV, and 360~378HV, respectively. Because of the microstructure on the FZ, the secondary α contributes to the higher hardness than it is in the HAZ and BM. Another mechanical property, tensile strength, was also measured. But, the samples slipped during the testing process, and no extra samples were available for additional testing. Therefore, there are no YS, UTS, EL results available for this processing condition.

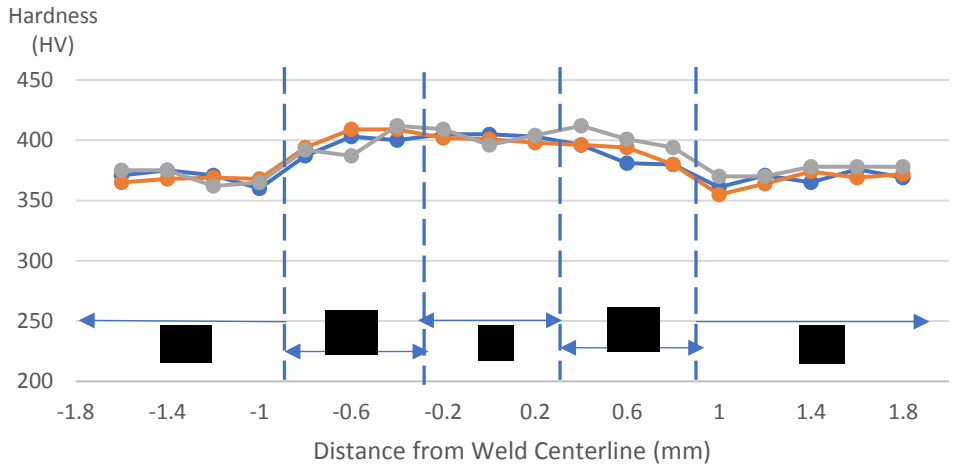

Figure 3.30: the hardness profile of three zones of 2.5 hours 500°C aging following air cooling

3.2.1.2 Aging at 500°C for 4 hours

When the aging time was extended to 4 hours, the representative microstructure of BM, HAZ, and FZ were obtained and are shown in Figure 3.31-3.33. The primary α textured in the β matrix can be found in both of the BM (Figure 3.31) and HAZ (Figure 3.32). For more details, the α volume fraction of BM and HAZ are 39.4±2.4% and 43.5±4.7%, respectively. In addition, the average α grain size of these two zones are 4.5±3.4μm and 6.0±4.1μm, respectively. On the BM, the spherical α grain size is 1.6±0.6, and the lath α grain size is 8.1±1.5μm. As for the HAZ, the spherical and lath α grain size show 7.7±2.0μm and 2.1±0.6μm, respectively. When observing the FZ, Figure 3.33 shows that only β phase can be found. This is because the secondary α is too fine to be seen by the light optical microscopy. The hardness profile of aging 4 hours LBW Ti1023 is shown in the Figure 3.34. It can be found that

the hardness of FZ is closed to it of HAZ, and higher than it of BM. The measured results show that the BM hardness is 362~408HV, the HAZ hardness is 404~459HV, and the FZ hardness is 400~459HV. Here, the secondary α phase has a strong effect on rising hardness. The tensile test result is shown in Figure 3.35. Form this curve, the YS, UTS, and EL can be found as 1086MPa, 1160MPa, and 3.3%, respectively. In addition, the strain map during tensile test is shown in Figure 3.36. It presents that higher strain area locates on the BM during the tensile test. However, the final break area locates on the FZ. That means the ductility on the BM is higher than it on the FZ in this heat treatment condition. After tensile test, the SEM micrographs of the specimen fracture surface were taken. The fracture surface was observed at different magnification and shown in Figure 3.37. Both microvoids coalescence (on the middle) and the transgranular fracture (on the bottom) can be observed in Figure 3.37(a). Furthermore, at higher magnification shown in Figure 3.37(b), these two fracture surfaces were littered with shallow dimple rupture. Therefore, despite the elongation data being low, this fracture morphology still exhibited a ductile behavior. In addition, this phenomenon was also reported for PWHT Ti5553 [38].

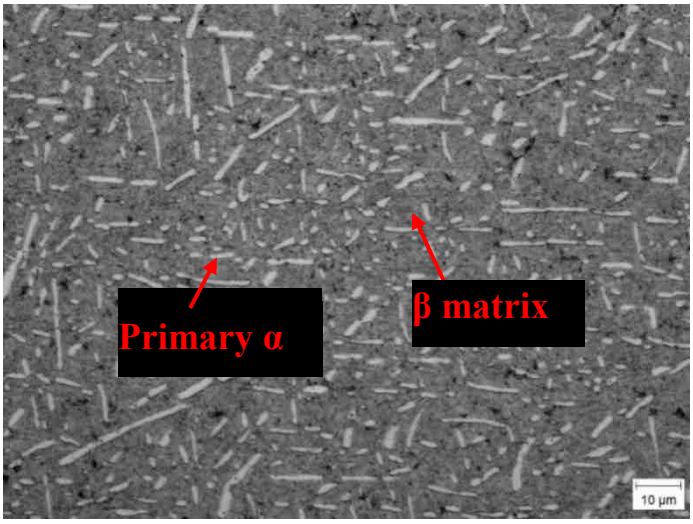

Figure 3.31: Light optical microstructure of aging 4 hours LBW Ti1023 base material (BM) presenting the primary α (bright area) and β matrix phase (gray area)

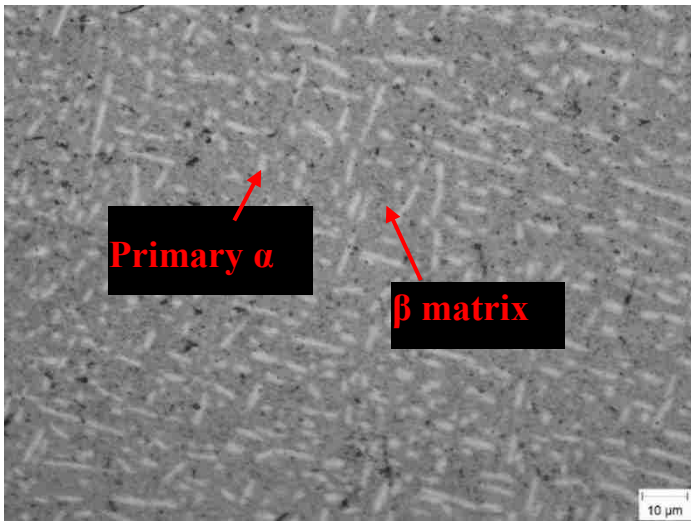

Figure 3.32: Light optical microstructure of aging 4 hours LBW Ti1023 heat affected zone (HAZ) presenting the primary α (bright area) and β matrix phase (gray area)

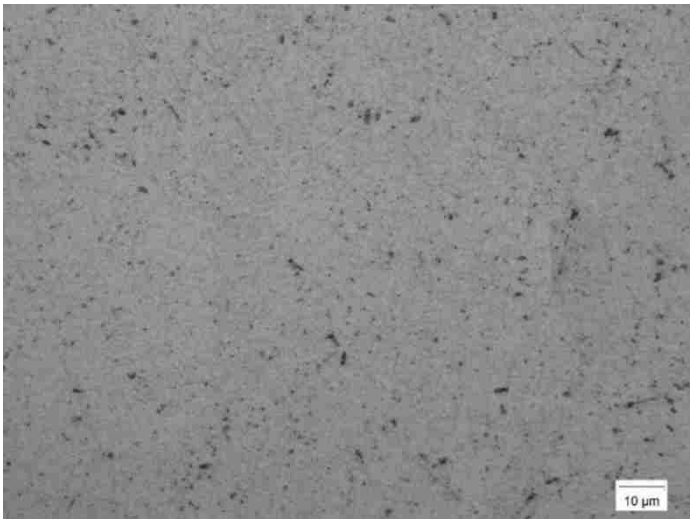

Figure 3.33: Light optical microstructure of aging 4 hours LBW Ti1023 fusion zone (FZ) only shows the β phase

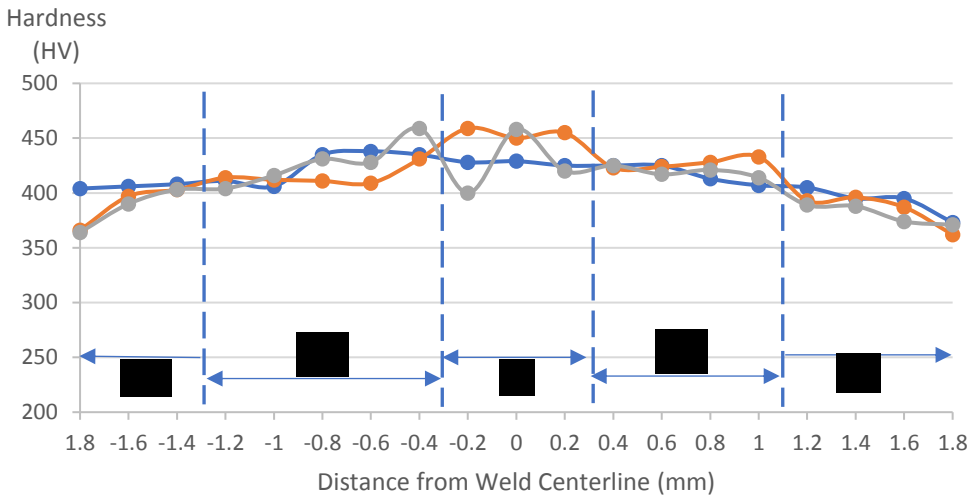

Figure 3.34: The hardness profile of three zones of 4 hours 500ºC aging following air cooling shows the higher hardness on the FZ

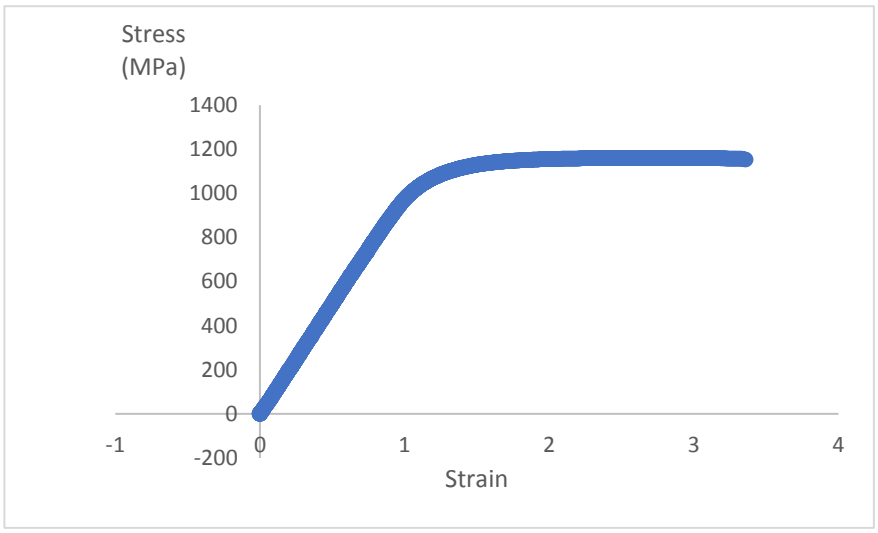

Figure 3.35: The engineering stress-strain curve of 4 hours 500ºC aging

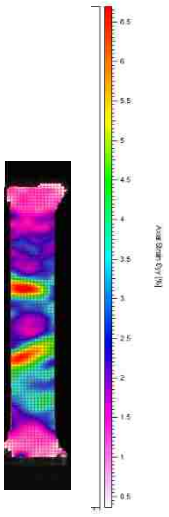

Figure 3.36: Strain map of the sample during tensile testing. The different colors specify strains

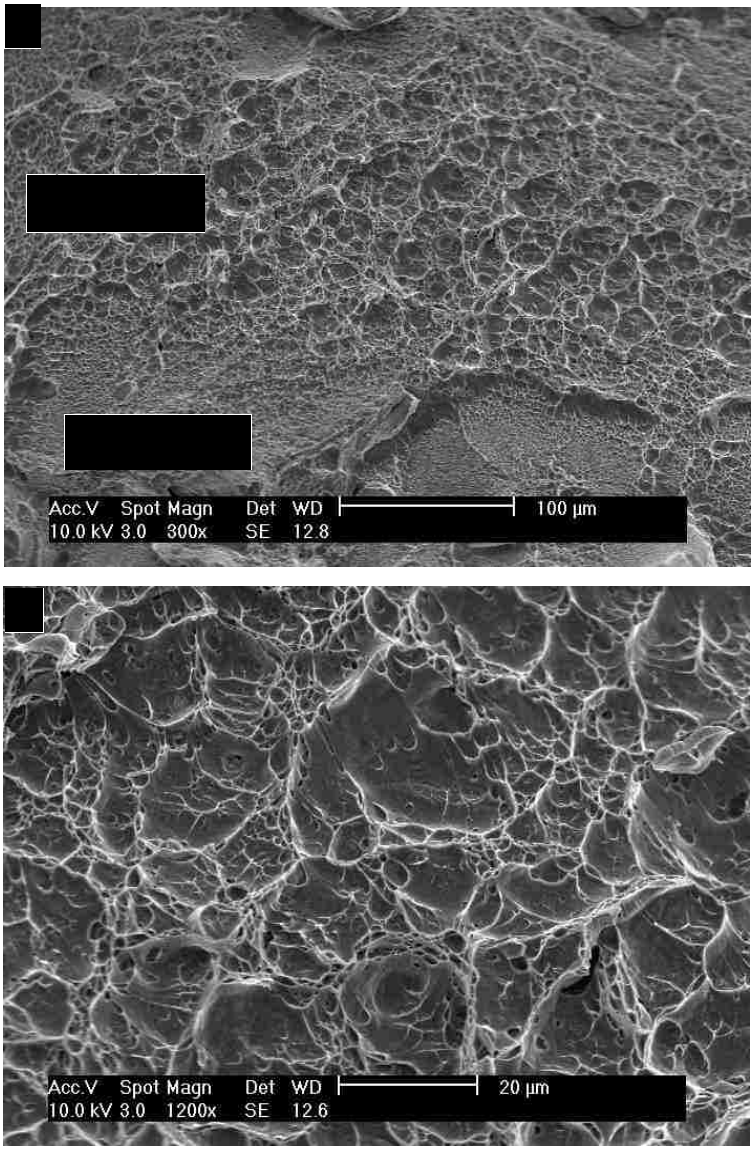

Figure 3.37: SEM micrographs at different magnification of the tensile test specimen fracture surface aged for 4 hours at 500°C (a) magnification: 300x (b) magnification: 1200x

3.2.1.3 Aging at 500°C for 5 hours

Figure 3.38 shows the microstructure of LBW Ti1023 BM material after aging for 5 hours, in which the α volume fraction is 40.4±3.0%. The average α grain size is 4.6±3.6μm. In addition, dividing the phase into spherical and lath α, the grain size of these two are 1.3±0.4μm and 7.2±1.8μm, respectively. Figure 3.39 presents the HAZ microstructure. By measuring, the α volume fraction increased to 43.6±3.5%. Also, the

α average grain size, spherical α grain size, and lath α grain size increased to 6.0±4.1μm, 1.9±0.6μm, and 8.4±2.3μm, respectively. Figure 3.41 shows the hardness of BM, HAZ, and FZ are 353~410HV, 387~441HV, and 396~444HV, respectively. The tensile test of this heat treatment condition was performed, but without recording the stain map. Therefore, only the UTS value was measured as 1153MPa.

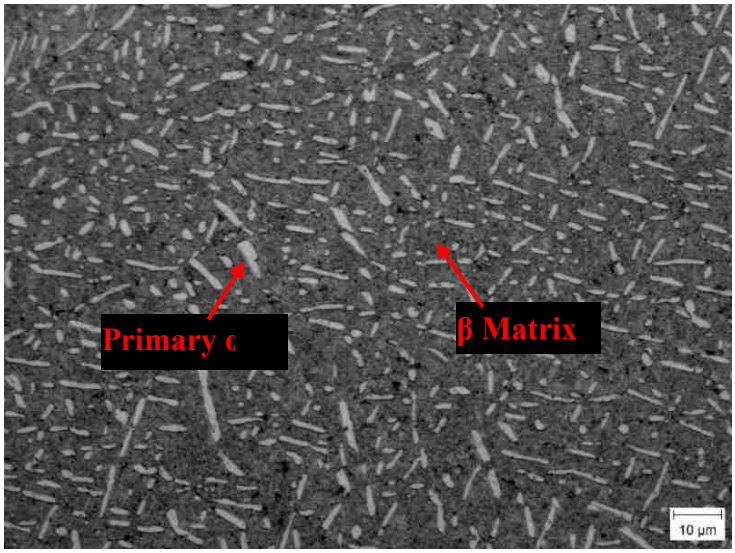

Figure 3.38: Light optical microstructure of aging 5 hours LBW Ti1023 base material (BM) presenting the primary α (bright area) in the β matrix (gray area)

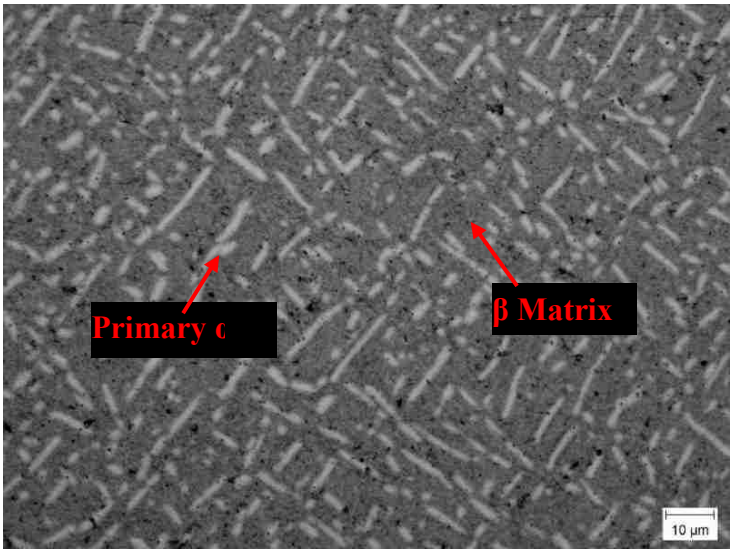

Figure 3.39: Light optical microstructure of aging 5 hours LBW Ti1023 heat affected zone (HAZ) presenting the primary α (bright area) and β matrix phase (gray area)

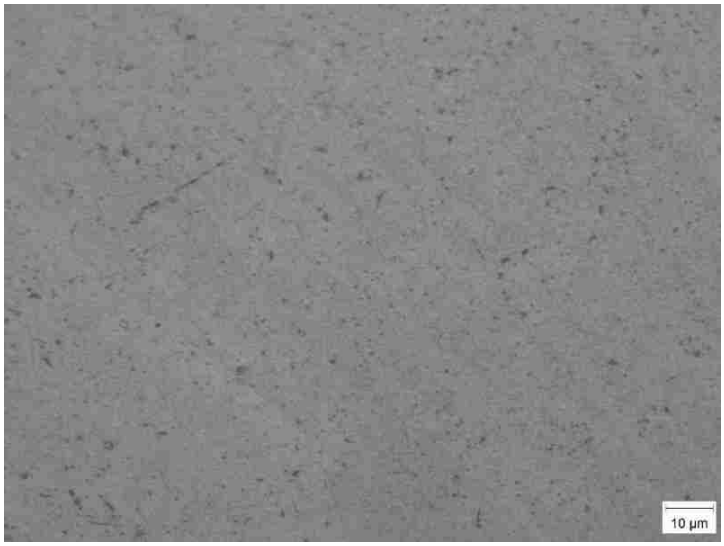

Figure 3.40: Light optical microstructure of aging 4 hours LBW Ti1023 fusion zone (FZ)

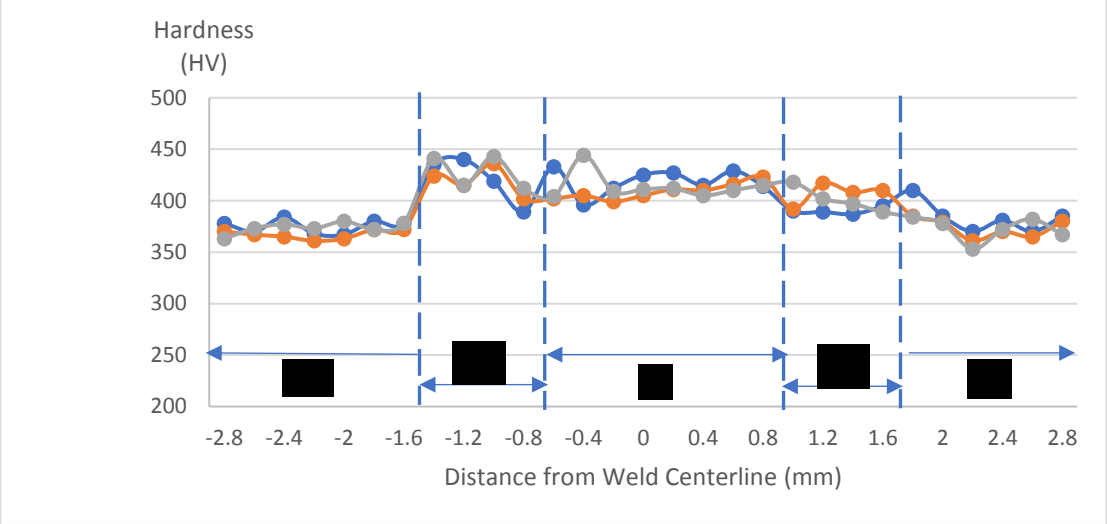

Figure 3.41: The hardness profile of three zones of 5 hours 500°C aging sample

3.2.1.4 Aging at 500°C for 6 hours

For this condition, the light optical image of BM is shown in Figure 3.42. After measuring, the α volume fraction is 40.1±3.7% and the average α grain size is 5.2±4.0μm. In addition, the spherical and lath α grain size is 1.5±0.5μm and 7.7±1.9μm, respectively. Almost similar microstructure is shown in Figure 3.43, which

is the structure of HAZ. However, the heat influence from laser welding reduced the sharpness of α grain and modified the α grain size. The α volume fraction is 43.2±3.3%. The spherical and lath α grain size is 1.8±0.5μm and 7.0±1.9μm, separately. That makes the average α grain size is 5.0±3.5μm on the HAZ. As for the FZ, which is shown in Figure 3.44. Only β and its grain boundary can be found in the optical image. However, the secondary α still contributes the higher hardness on the FZ. The microhardness profile through three zones of this condition is shown in the Figure 3.45. On each zone, the hardness is 343~390HV (BM), 379~447HV (HAZ), and 374~463HV (FZ). The tensile stress vs. strain curve is shown in Figure 3.46. The YS, UTS, and EL are 1031MPa, 1083MPa, and 3%, respectively. The strain map of the sample before the it broken is shown in Figure 3.47. It shows the higher stain area located on the BM. In addition, this location is also the broken area of this sample after tensile test.

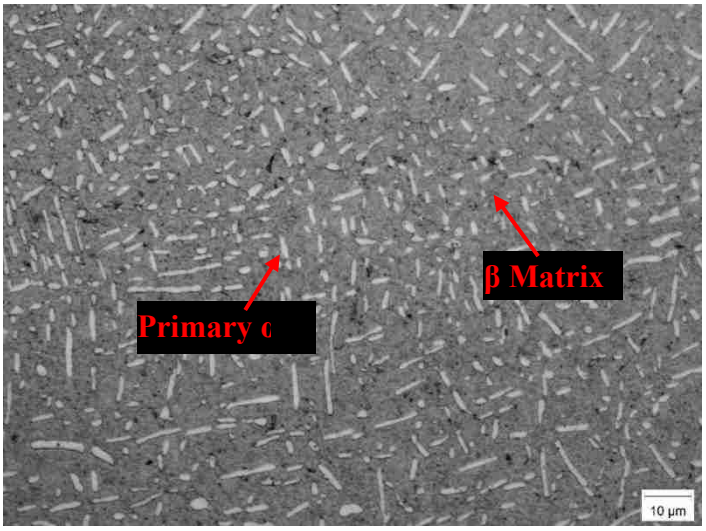

Figure 3.42: Light optical microstructure of aging 6 hours LBW Ti1023 base material (BM) presenting the primary α (bright area) and β matrix phase (gray area)

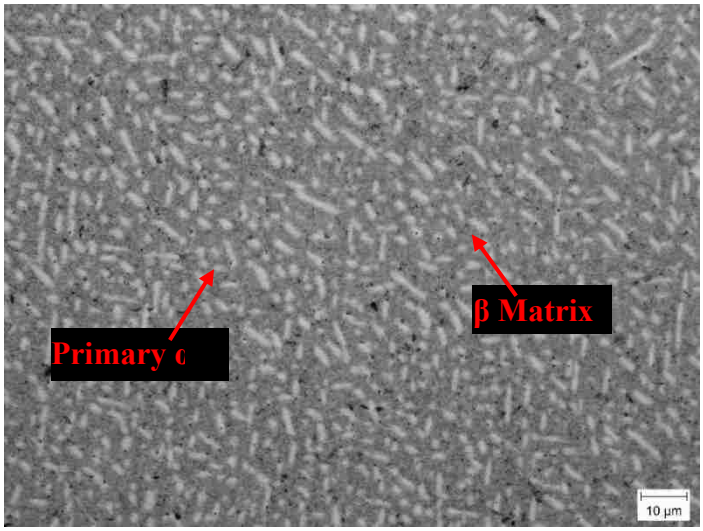

Figure 3.43: Light optical microstructure of aging 6 hours LBW Ti1023 heat affected zone (HAZ) presenting the primary α (bright area) and β matrix phase (gray area)

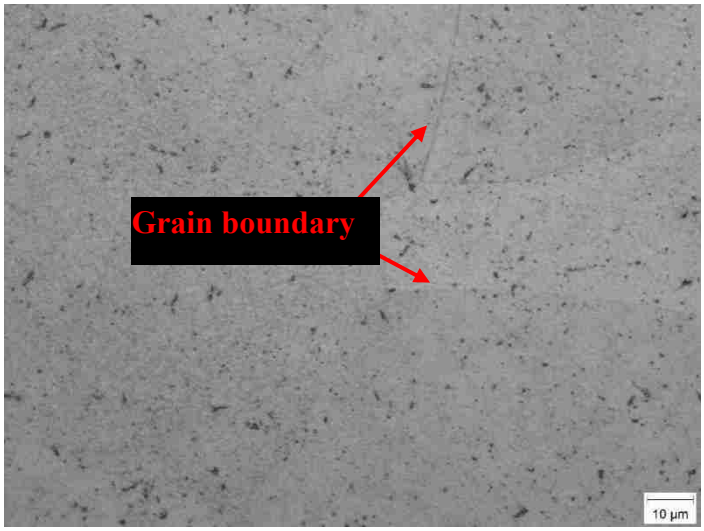

Figure 3.44: Light optical microstructure of aging 6 hours LBW Ti1023 fusion zone (FZ)

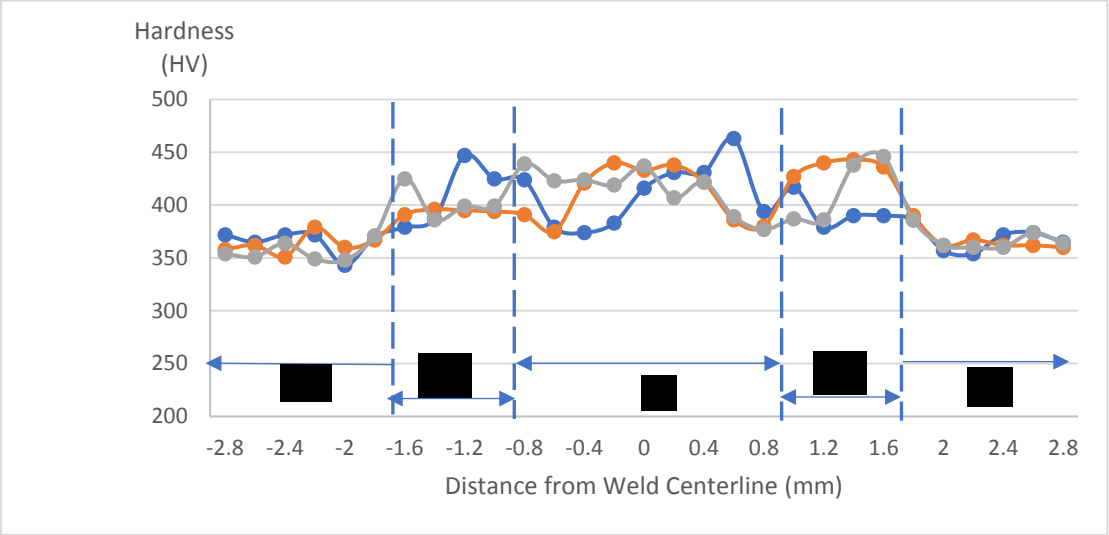

Figure 3.45: The hardness profile of three zones of 6 hours 500°C aging

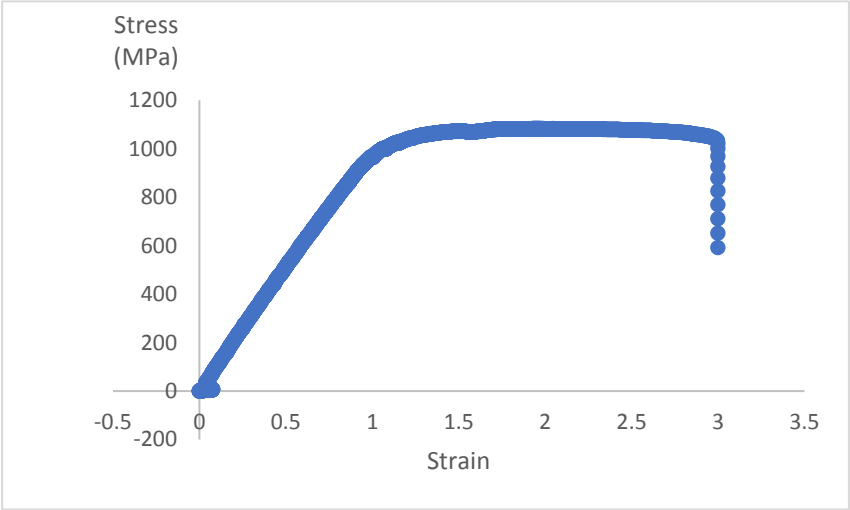

Figure 3.46: The engineering stress-strain curve of 6 hours 500°C aging

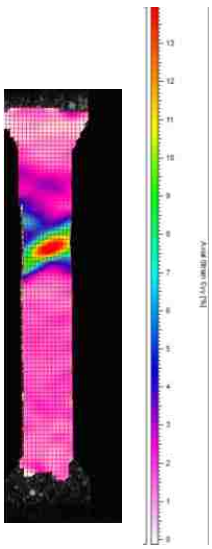

Figure 3.47: Strain map of the sample during tensile testing. The different colors specify strains

3.2.1.5 Aging at 500°C for 10.5 hours

The optical images of these three zones are shown in Figures 3.48-3.50. It can be observed that the spherical and lath α phase is textured in the β matrix on the BM (Figure 3.48) and HAZ (Figure 3.49). In the BM, the α volume fraction is 39.2±3.5% and the average α grain size is 5.4±4.4μm. For more details, the spherical α size is 1.5±0.5μm and the lath α size is 8.3±2.4μm. From Figure 3.45 (HAZ), the average α grain size is 5.1±3.8μm. Also, the spherical and lath α size is 1.8±0.6μm and 7.5±1.9μm, respectively. The α volume fraction is 43±2.2%. The optical image of FZ is shown in Figure 3.50. Different gray level makes β grain boundaries easier to be observed. The hardness profile is shown in Figure 3.51. The hardness of FZ and HAZ is 362~411 HV and 345~396 HV, respectively. That is higher than the hardness of BM (344~387 HV). The tensile test result is shown in Figure 3.52. The YS is 1030 MPa, the UTS is 1068 MPa, and EL is 4.2%. Figure 3.53 shows the higher strain area located in the BM, which is the same area when observing the sample, which fractured.

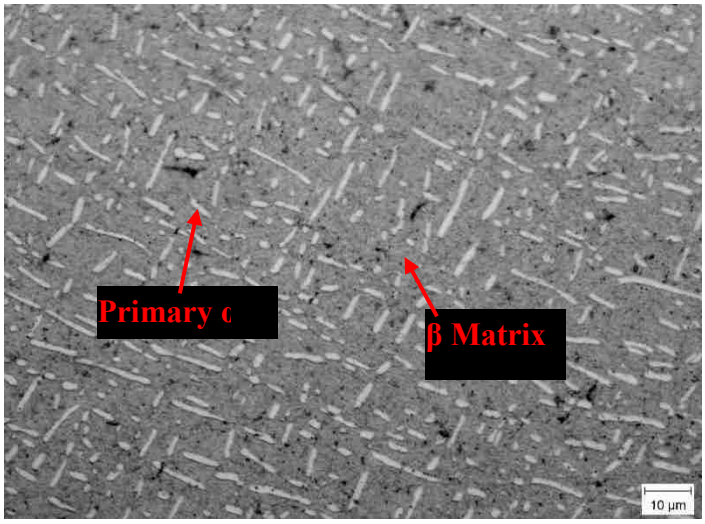

Figure 3.48: Light optical microstructure of aging 10.5 hours LBW Ti1023 base material (B) presenting the primary α (bright area) and β matrix phase (gray area)

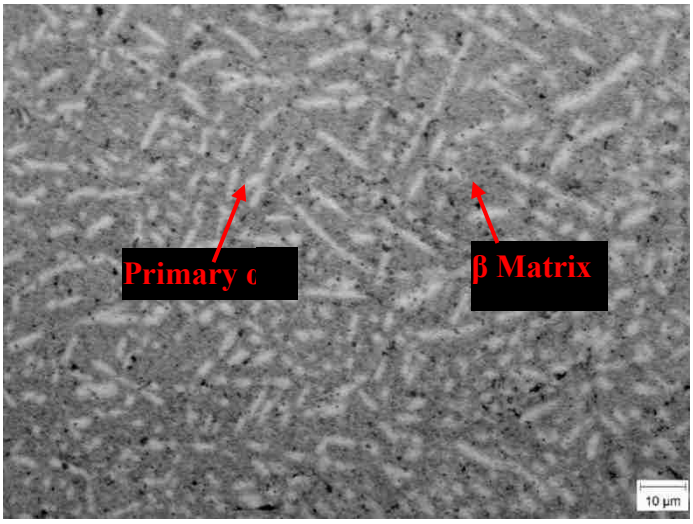

Figure 3.49: Light optical microstructure of aging 10.5 hours LBW Ti1023 heat affected zone (HAZ) presenting the primary α (bright area) and β matrix phase (gray area)

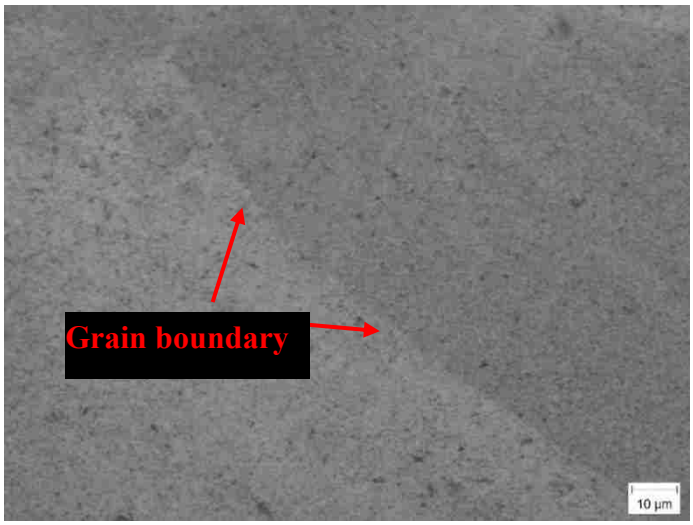

Figure 3.50: Light optical microstructure of aging 10.5 hours LBW Ti1023 fusion zone (FZ) shows β phase and its gain boundary

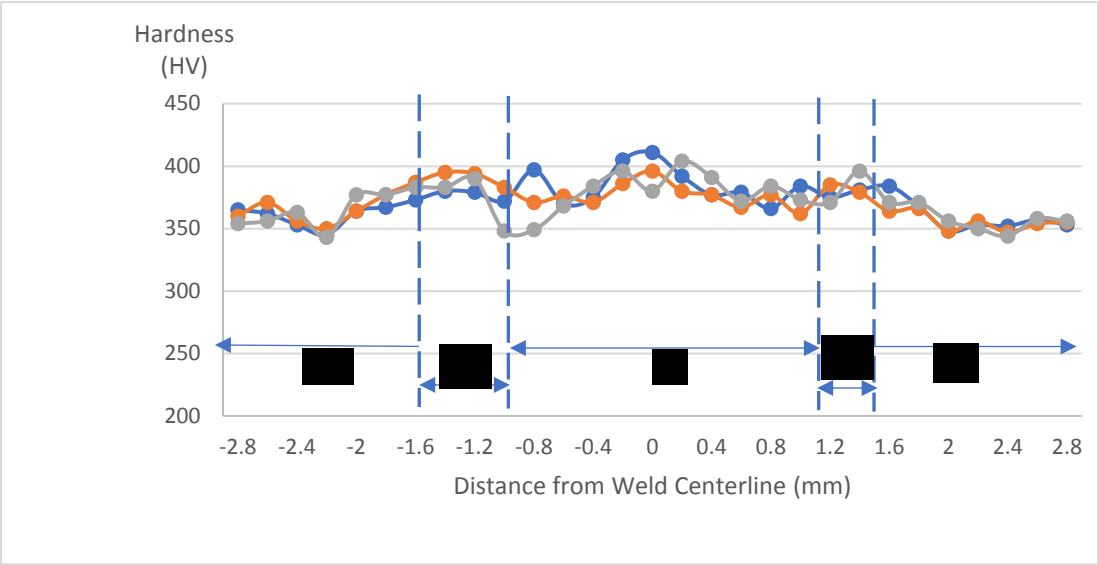

Figure 3.51: The hardness profile of three zones of 10.5 hours 500°C aging following air cooling

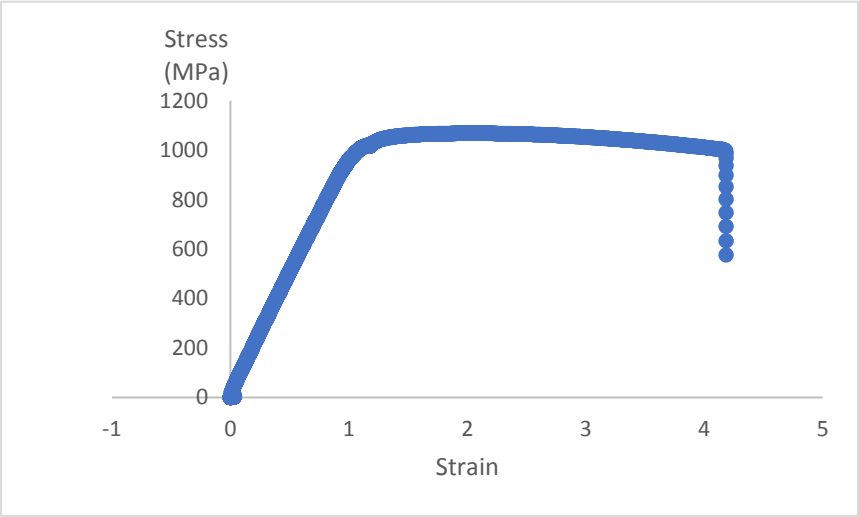

Figure 3.52: The engineering stress-strain curve of 10.5 hours 500°C aging sample

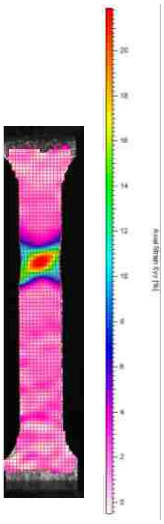

Figure 3.53: Strain map of the sample during tensile testing. The different colors specify strains

3.2.1.6 Aging at 500°C for 20 hours

The microstructures of three zones are shown in Figure 3.54-3.56. The α volume fraction on the BM is 38.6±4.8%. The average α grain size is 4.2±3.2μm, the spherical α size is 1.5±0.5μm, and the lath α size is 6.5±1.9μm. When measuring the images of HAZ, the α volume fraction is 42.4±3.2%. The spherical α size is 1.5±0.5μm, and the lath α size is 7.1±2.1μm. That makes the average α grain size is 4.7±3.6μm. From Figure 3.56, we can conclude that there is still only β phase present in the FZ. For the mechanical properties, Figure 3.57 shows the hardness profile and Figure 3.58 shows the tensile test results. The hardness of BM, HAZ, and FZ is 336~373 HV, 346~380HV, and 350~380HV, respectively. The YS, UTS, and EL is 919MPa, 935MPa, and 4%, respectively. The strain map (Figure 3.59) during tensile test presents the higher strain area located in the BM.

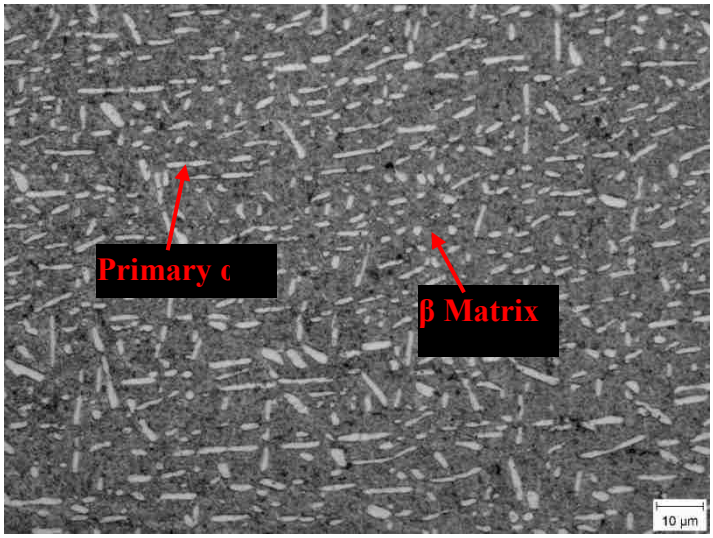

Figure 3.54: Light optical microstructure of aging 20 hours LBW Ti1023 base material (BM) presenting the primary α (bright area) and β matrix phase (gray area)

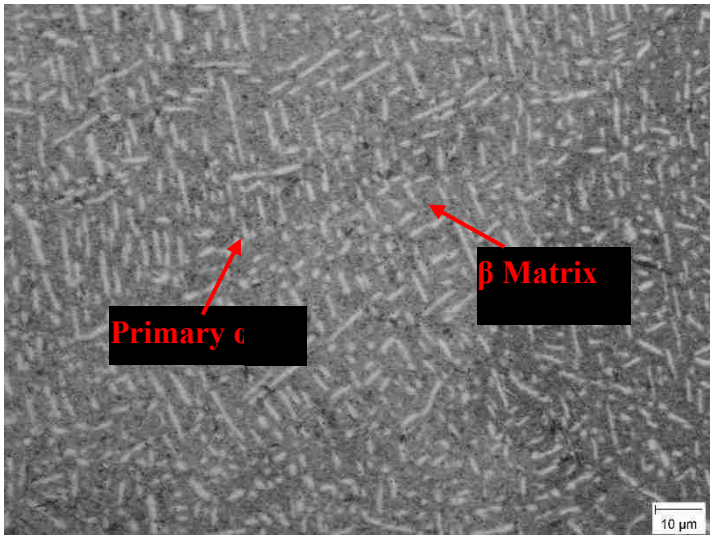

Figure 3.55: Light optical microstructure of aging 20 hours LBW Ti1023 heat affected zone (HAZ) presenting the primary α (bright area) and β matrix phase (gray area)

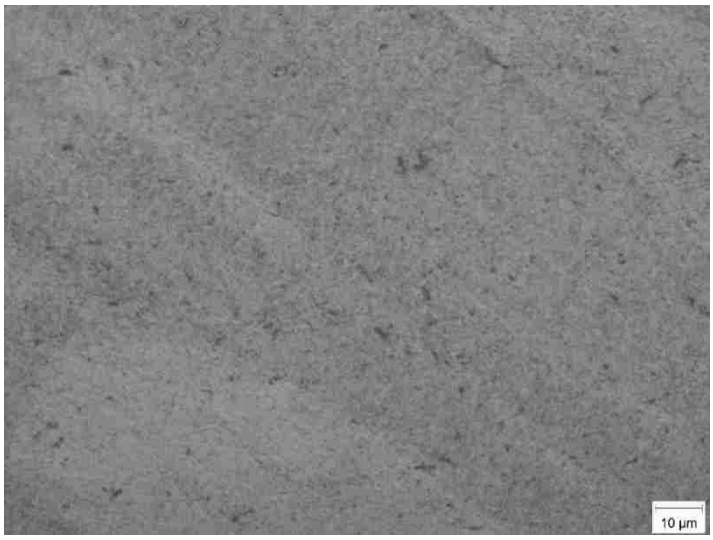

Figure 3.56: Light optical microstructure of aging 20 hours LBW Ti1023 fusion zone (FZ)

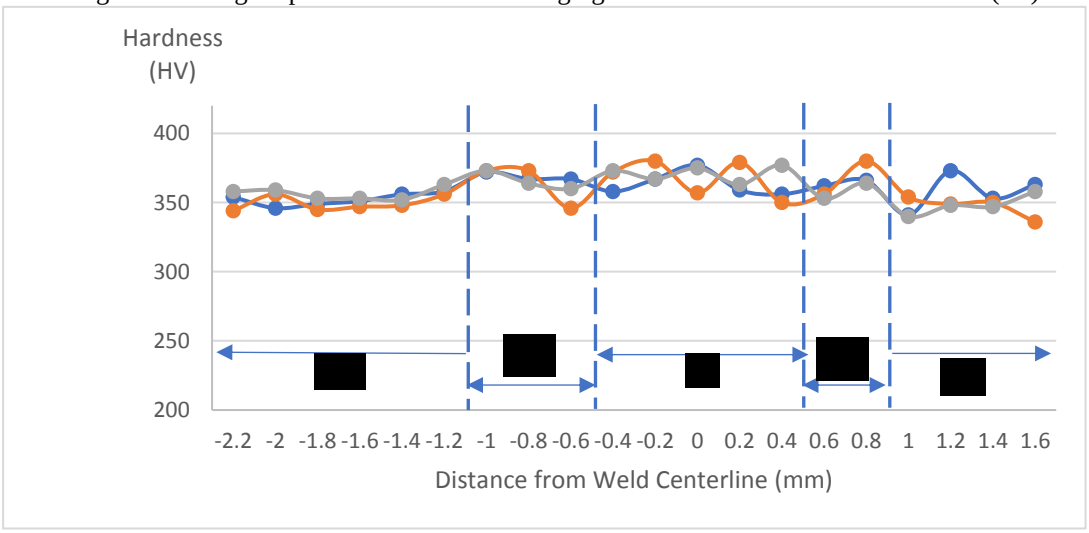

Figure 3.57: The hardness profile of three zones of 20 hours 500ºC aging sample

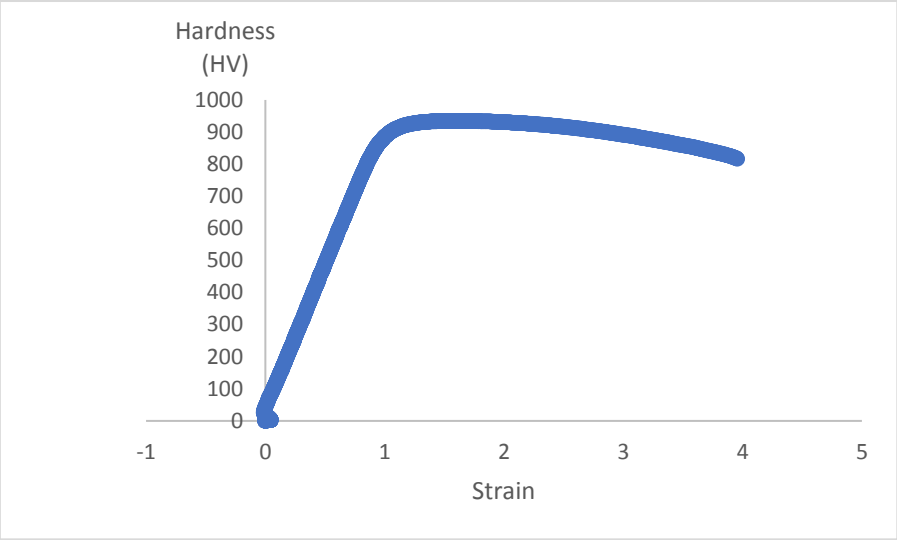

Figure 3.58: The engineering stress-strain curve of 20 hours 500°C aging

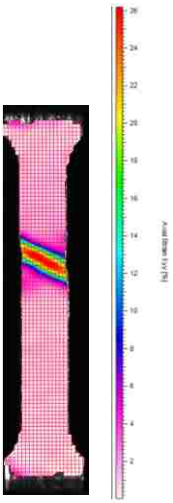

Figure 3.59: Strain map of the sample during tensile testing. The different colors specify strains

3.2.2 Microstructure observation, Microhardness Profiles and Tensile Strength of the Annealing+Aging conditions

3.2.2.1 Annealing at 750°C for 1 hour

The sample, which went only through the annealing treatment without any aging was also investigated in this heat treatment group. The microstructure of BM is

shown in Figure 3.60. It can be observed that the spherical and lath α grain is textured in the β matrix. However, comparing to Figure 3.1, the sharpness of α grain decreased after 750°C annealing. In addition, this microstructure looks like the structure on the heat affected zone, some α grain began to break to several smaller pieces and decreased its sharpness. Therefore, even the heat treatment temperature did not achieve the β-transus of Ti1023, the heat from the 750°C treatment loosed the α phase crystal structure and prepared to transform to the β phase as long as the temperature higher than the β-transus. The α volume fraction of BM is 33.6±4.3%. The average α grain size is 3.4±2.4μm. In addition, the spherical and lath α is 1.4±0.4μm and 5.2±1.4μm, respectively. Figure 3.61 shows the microstructure of HAZ. The thin and dendritic α grains textured in the β matrix can be found in the HAZ. This structure was the result of the heat from the welding and the annealing. The α volume fraction of HAZ is 35.5±6.4%. The average α grain size is 2.9±1.7μm. For more details, the spherical α size is 0.8±0.3μm and the lath α size is 4.0±1.0μm. The microstructure of FZ is shown in Figure 3.62. The β grain is full of the primary α formed form the 750°C treatment. In addition, some α was formed on the β grain boundary. The α volume fraction of the FZ is 49.7±2.2%. The grain size of the primary α inside the β grain is 2.4±0.7μm. This microstructure presents a big different α structure on the FZ when comparing to the only β phase on the as-welded sample. This primary α grain also can be found on the

HAZ, but can-not be observed on the BM. So, even some α phase formed from the 750°C treatment, it tends to merge into the original primary α phase on the BM. Moreover, because the formed primary α is found within the FZ, it can make sure this heat treatment condition does not excess the β-transus. Therefore, the α phase in the BM just decreased its sharpness and loosed its structure, but without transform to the β phase yet. This primary α formed within the β phase structure of FZ is also confirmed by the SEM (Figure 3.63) and BSE (Figure 3.64) images. Comparing to the BSE of the aging group (Figure 3.29), only primary α phase and β matrix can be found in the annealed specimen, and without any secondary α. The hardness profile through three zones is shown in Figure 3.65. The hardness of the FZ is 308~322 HV, that is higher than it of the HAZ (298~318 HV) and BM (289~316HV). This phenomenon can be attributed to the larger amount of α volume fraction and finer average α grain size within the FZ. The tensile test result is shown in Figure 3.66. The YS, UTS, and EL of this sample is 756MPa, 801 MPa, and 2.47%, respectively. The strain map during tensile test is shown in Figure 3.67. One unusual case was observed and it only happened in this heat treatment. In the middle of tensile test, the FZ showed the higher strain. However, the higher strain area moved to the BM and then the sample broke within the same area. That means the FZ has better ductility than the BM within this sample.

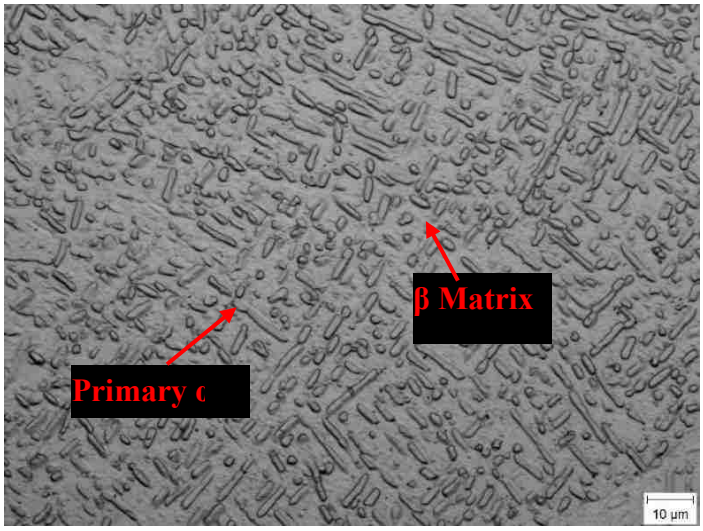

Figure 3.60: Light optical microstructure of annealing 1 hour LBW Ti1023 base material (BM) presenting the primary α (bright area) and β matrix phase (gray area)

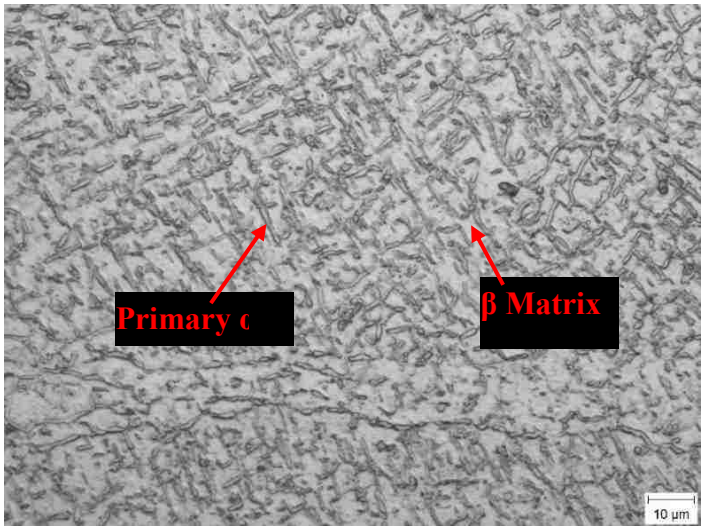

Figure 3.61: Light optical microstructure of annealing 1 hour LBW Ti1023 heat affected zone (HAZ) presenting the primary α (bright area) and β matrix phase (gray area)

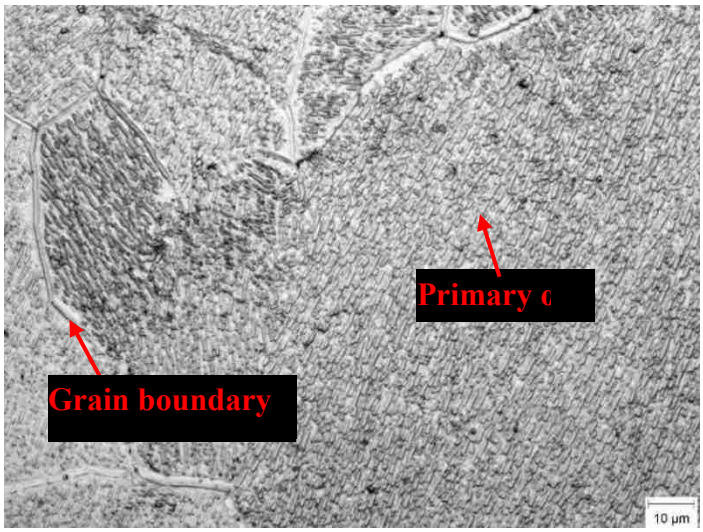

Figure 3.62: Light optical microstructure of annealing 1 hour LBW Ti1023 fusion zone (FZ)

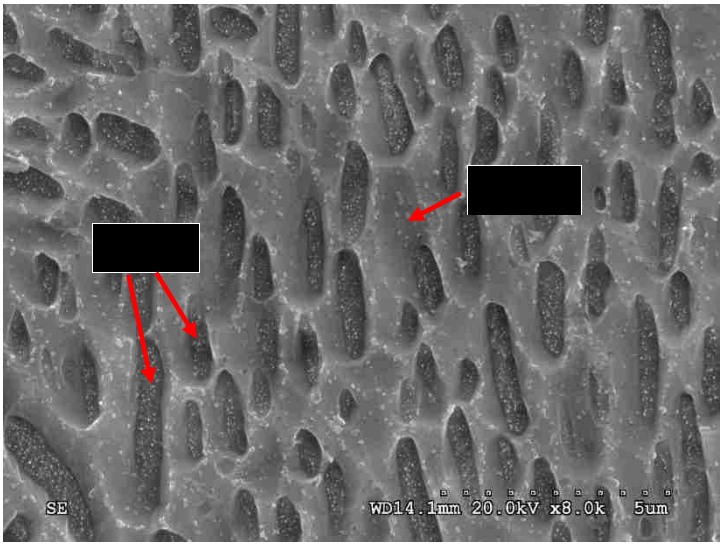

Figure 3.63: Scanning electron microscopy image of annealing 1 hour LBW Ti1023 fusion zone (FZ) presenting primary α grain and β matrix phase

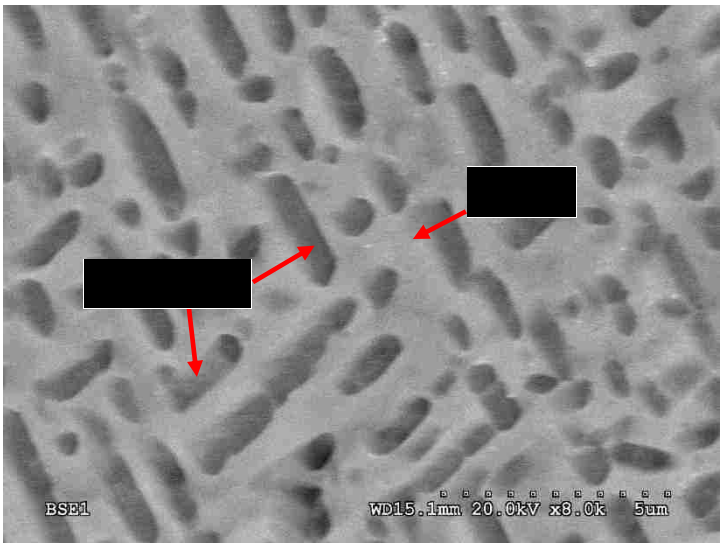

Figure 3.64: Back-scattered electrons image of annealed sample for 1 hour LBW Ti1023 fusion zone (FZ) presenting primary α grain and β matrix phase

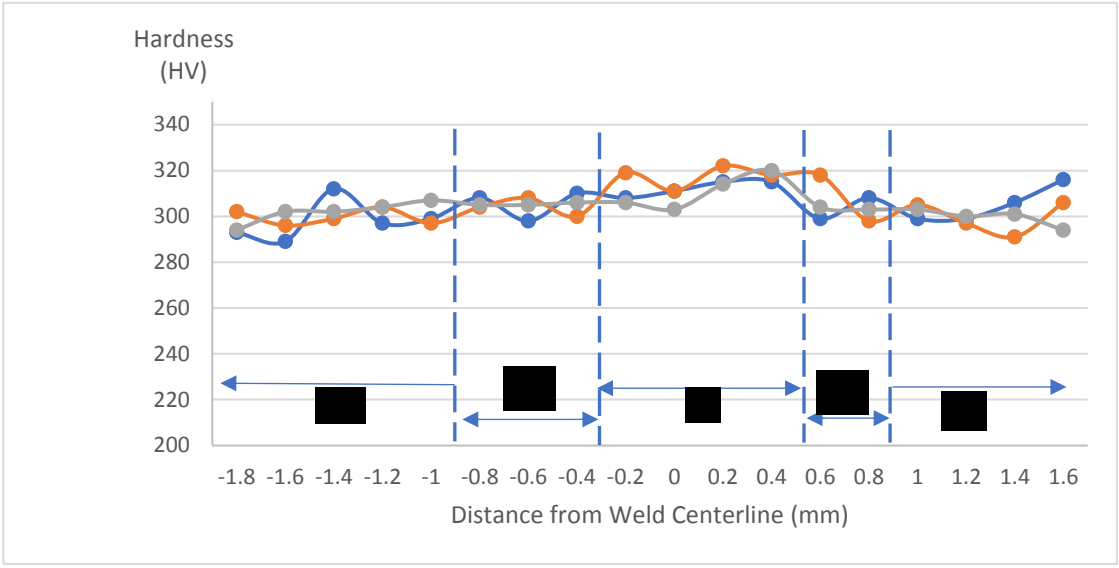

Figure 3.65: The hardness profile of three zones of annealing 1 hour

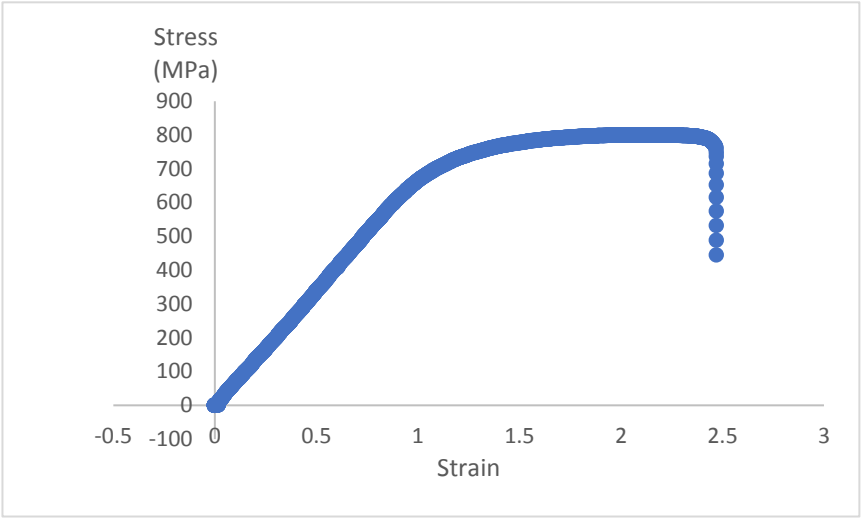

Figure 3.66: The engineering stress-strain curve of annealing 1 hour following water quenching

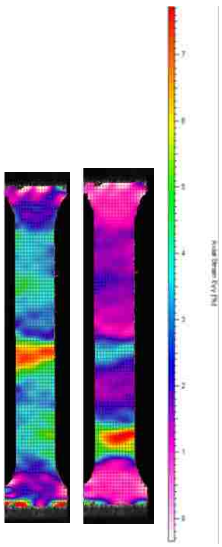

Figure 3.67: Strain map of the sample during tensile testing. The different colors specify strains

3.2.2.2 Annealing at 750°C for 1 hour plus aging at 500°C for 2.5 hours

The microstructure of BM is shown in Figure 3.68. The lath and spherical α phase is textured in the β matrix. In addition, after aging process, the α grain is clearer than it is in the only annealed sample. Form the results of only aging group (chapter 3.2.1), the secondary α is formed and observed in the aging step. In addition, only annealing condition shows the primary α is formed in the chapter 3.2.2.1. Thus, both of the primary α from the annealing step and the secondary α from the aging step were formed in this annealing plus aging condition. Moreover, the aging temperature is much lower than the β-transus and makes the α structure more stable. Therefore, these two reasons shape this morphology of α grains in Figure 3.68. Furthermore, the primary α formed from the annealing is also not easy to be observed due to its tendency to blend into the original primary α. The α volume fraction is 39.8±3.2%. The average α grain size is 4.5±3.5μm. In addition, the spherical α size is 1.5±0.6μm and the lath α size is 6.9±2.2μm. The HAZ microstructure is shown in Figure 3.69. This structure is similar to the thin and dendritic α textured in the β matrix on the annealing sample. The α volume fraction is 36.7±3.7% and the lath α size is 4.0±1.3μm. The optical image of FZ (Figure 3.70) shows the clear primary α and grain boundary α. The grain size of primary α is 1.6±0.8μm. And, the volume fraction of α phase is 50.8±1.8%. In addition, in the SEM (Figure 3.71) one can also observe the primary α and grain boundary α

within the β phase. The secondary α can be found in the BSE image (Figure 3.72). Next is the mechanical properties test. The hardness profile is shown in Figure 3.73. The BM hardness is 378~396HV, the HAZ hardness is 368~385HV, and the FZ hardness is 364~383HV. Although the FZ contains higher α volume fraction, the BM still presents higher hardness. It is believed that this hardness result may be affected by the secondary α. The YS, UTS, and EL of this sample is 968MPa, 1020MPa, and 1.83%, respectively. And, this tensile test curve is shown in Figure 3.74. During the tensile test, the stain map (Figure 3.75) shows that the higher strain area located within the FZ.

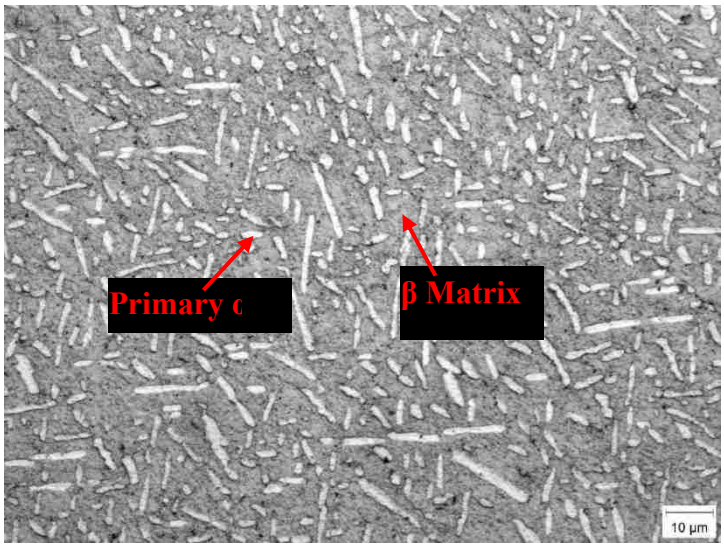

Figure 3.68: Light optical microstructure of annealing 1 hour plus aging 2.5 hours LBW Ti1023 base material (BM) presenting the primary α (bright area) and β matrix phase (gray area)

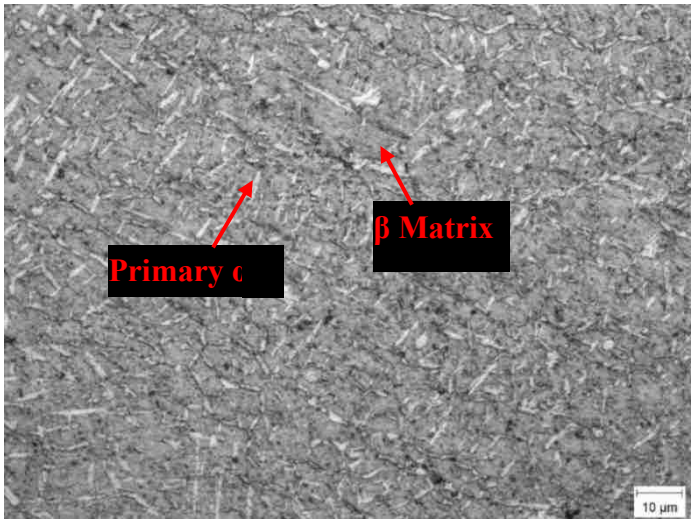

Figure 3.69: Light optical microstructure of annealing 1 hour plus aging 2.5 hours LBW Ti1023 heat affected zone (HAZ) presenting the primary α (bright area) and β matrix phase (gray area)

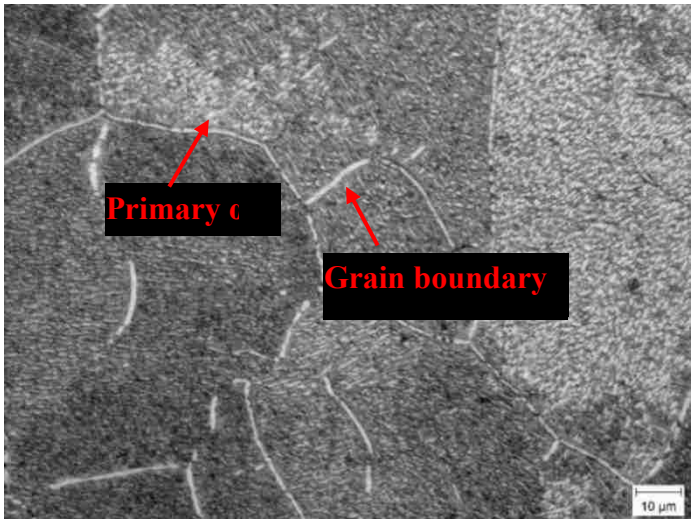

Figure 3.70: Light optical microstructure of annealing 1 hour plus aging 2.5 hours LBW Ti1023 fusion zone (FZ) shows primary α and grain boundary α

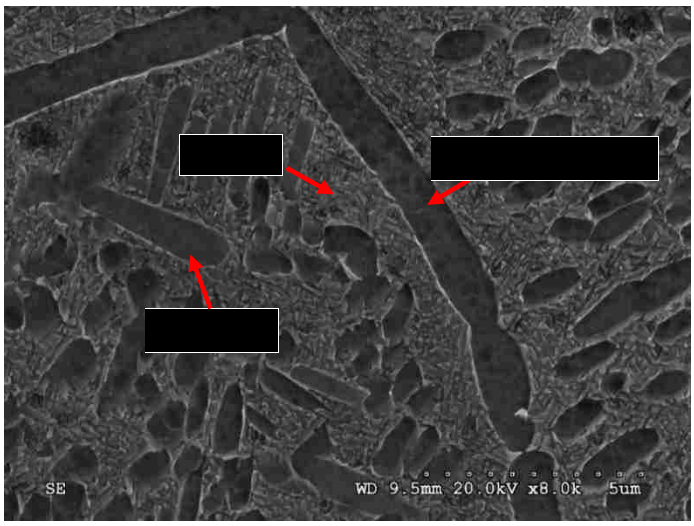

Figure 3.71: Scanning electron microscopy image of annealed 1 hour plus 2.5 hours LBW Ti1023 fusion zone (FZ) presenting primary α grain and β matrix phase

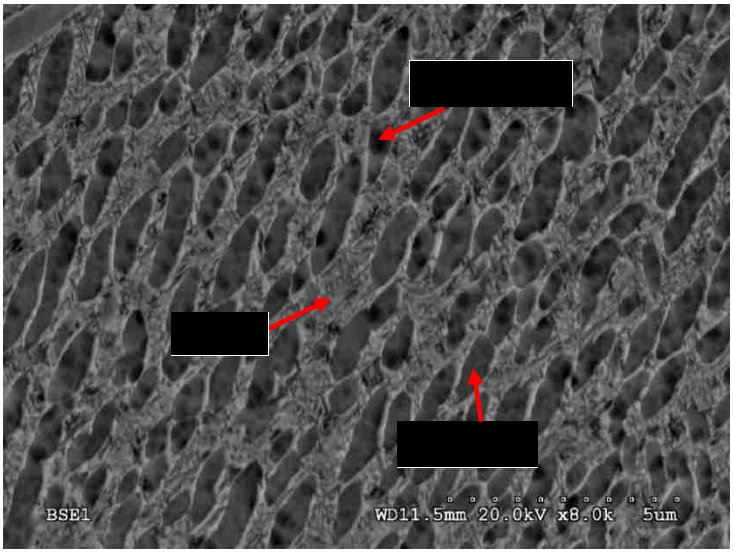

Figure 3.72: Back-scattered electrons image of annealed 1 hour plus 2.5 hours LBW Ti1023 fusion zone (FZ) presenting primary α grain and β matrix phase

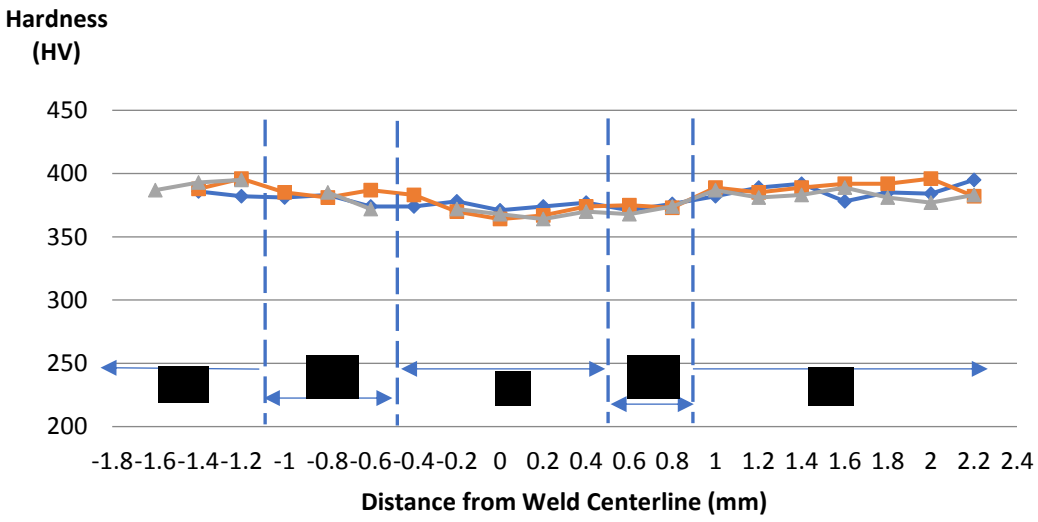

Figure 3.73: The hardness profile of three zones of annealing 1 hour plus aging 2.5 hours sample

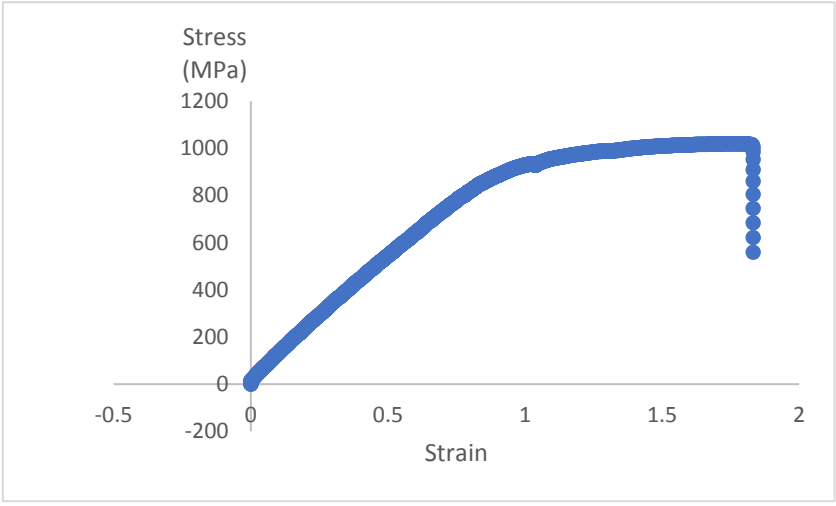

Figure 3.74: The engineering stress-strain curve of annealing 1 hour plus aging 2.5 hours

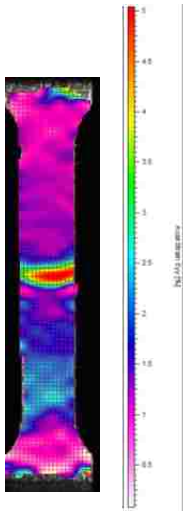

Figure 3.75: Strain map of the sample during tensile testing. The different colors specify strains

3.2.2.3 Annealing at 750°C for 1 hour plus aging at 500°C for 4 hours

The representative microstructures of three zones are shown in Figure 3.76-3.78. The microstructure of BM (Figure 3.76) contains spherical and lath α on a β matrix. The α volume fraction is 39.6±2.7%. The average α grain size is 5.0±3.8μm. Because its morphology, the spherical α is 1.9±0.8μm and the lath α is 7.1±1.9μm. In addition, the grain growth of spherical α can be observed in this sample. Figure 3.77 presents the structure of HAZ. The α morphology shows a thin and dendritic structure. And its volume fraction is 36±3.0%. Also, this lath α size is 4.5±1.4μm. As for the FZ, Figure 3.78 shows the β grain is full of the primary α and grain boundary α. The α volume fraction is 51.2±1.0%. In addition, the primary α size is 1.9±0.7μm. The hardness test showed the BM hardness (374~394HV), HAZ hardness (384~394HV) and FZ (379~392HV). The hardness profile is shown in Figure 3.79. In this sample, the

hardness of these three zones are almost equal. For the tensile test, the stress vs. strain curve is shown in Figure 3.80. And, the YS is 1090MPa, the UTS is 1170MPa, the EL is 2.1%. Moreover, the higher strain area during tensile located within the FZ of this sample (Figure 3.81). After tensile test, the SEM micrographs of the specimen fracture surface were taken and fracture surfaces were observed at different magnification and shown in Figure 3.82. Both microvoids coalescence and transgranular fracture can be observed in Figure 3.82(a). Furthermore, at higher magnification shown in Figure 3.82(b), these two fracture surfaces were littered with shallow dimple rupture.

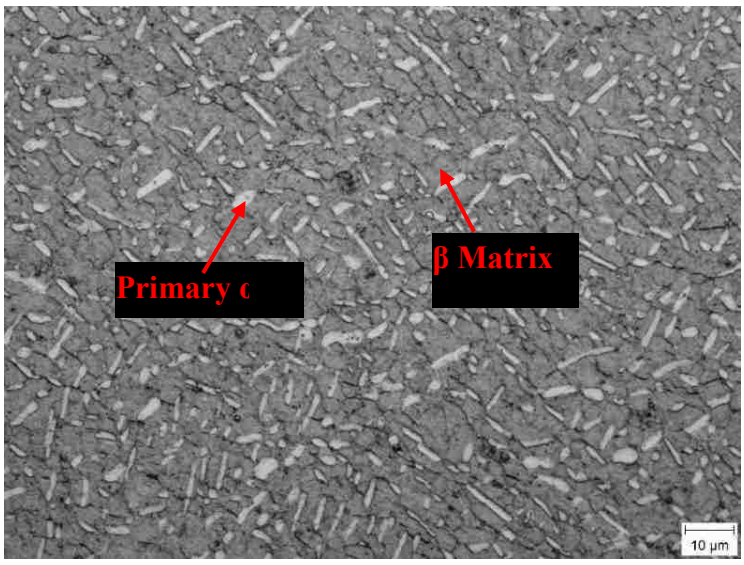

Figure 3.76: Light optical microstructure of annealing 1 hour plus aging 4 hours LBW Ti1023 base material (BM) presenting the primary α (bright area) and β matrix phase (gray area)

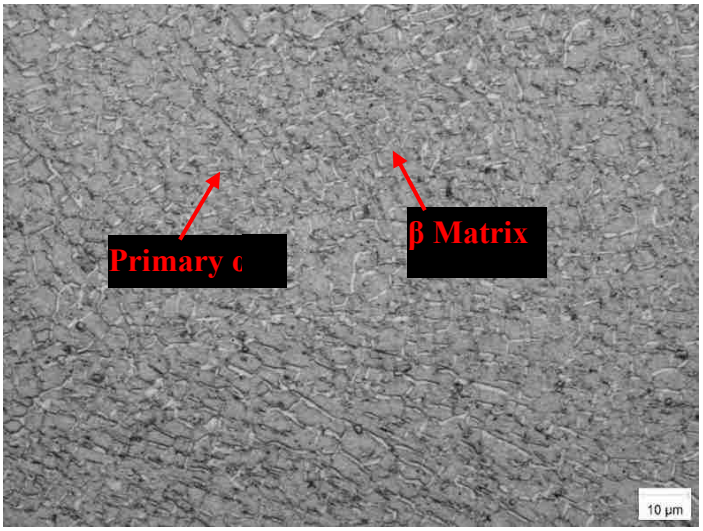

Figure 3.77: Light optical microstructure of annealing 1 hour plus aging 4 hours LBW Ti1023 heat affected zone (HAZ) presenting the primary α (bright area) and β matrix phase (gray area)

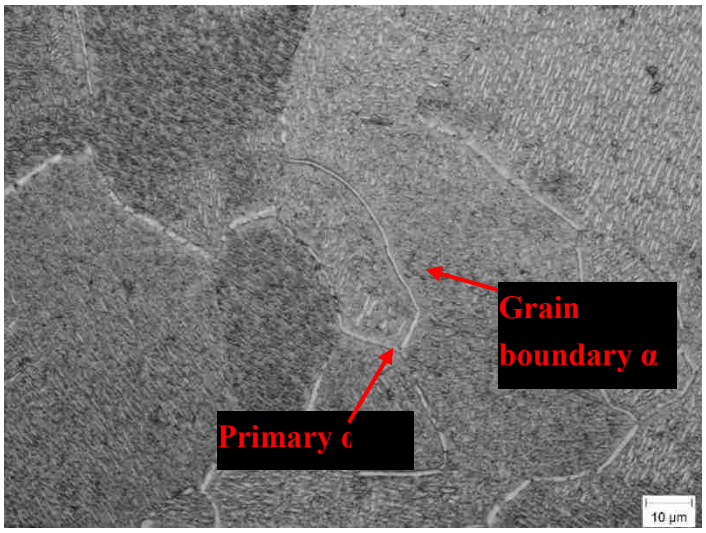

Figure 3.78: Light optical microstructure of annealing 1 hour plus aging 4 hours LBW Ti1023 fusion zone (FZ) shows primary α and grain boundary α

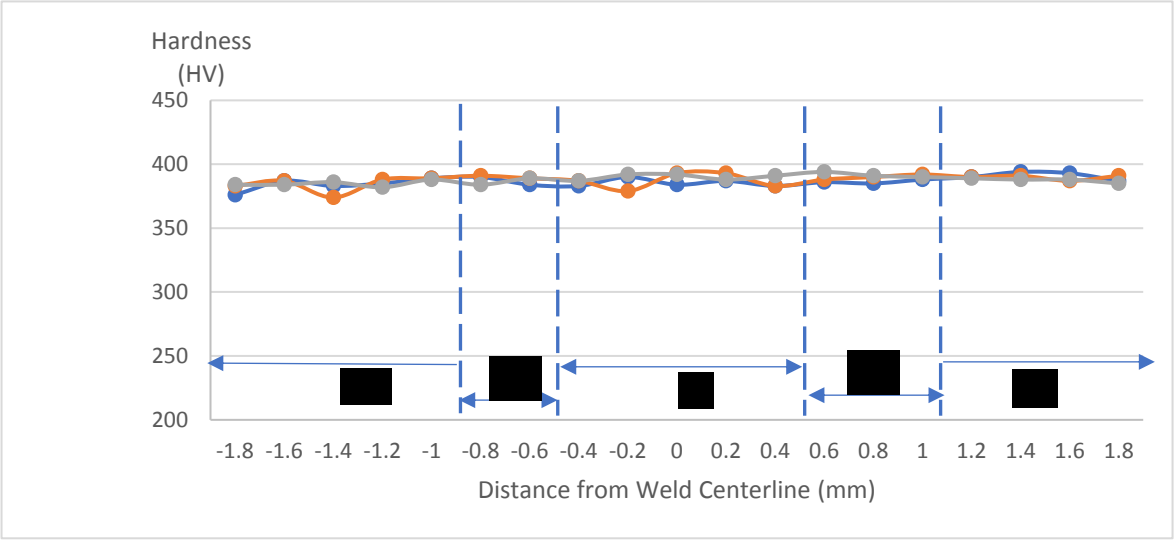

Figure 3.79: The hardness profile of three zones of annealing 1 hour plus aging 4 hours

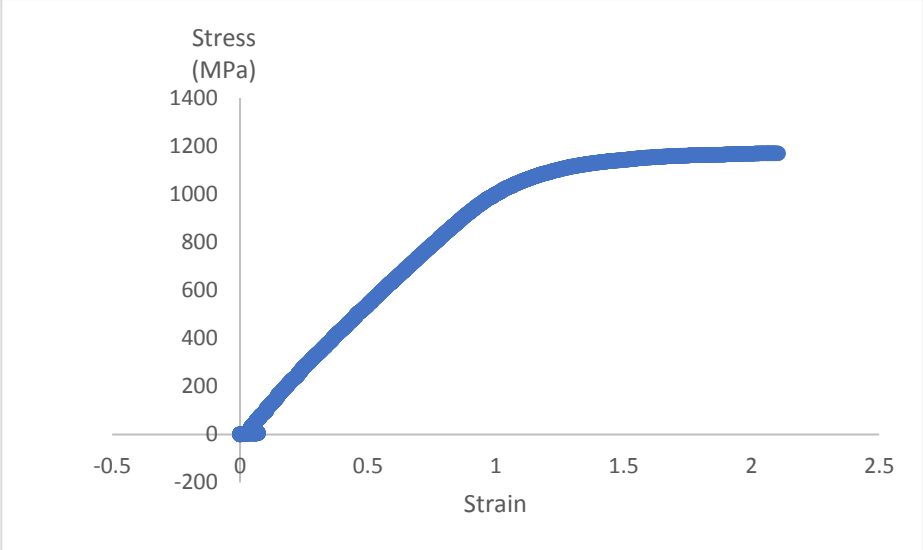

Figure 3.80: The engineering stress-strain curve of annealing 1 hour plus aging 4 hours

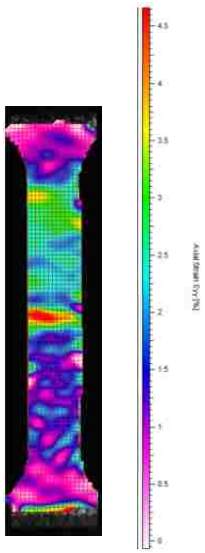

Figure 3.81: Strain map of the sample during tensile testing. The different colors specify strains

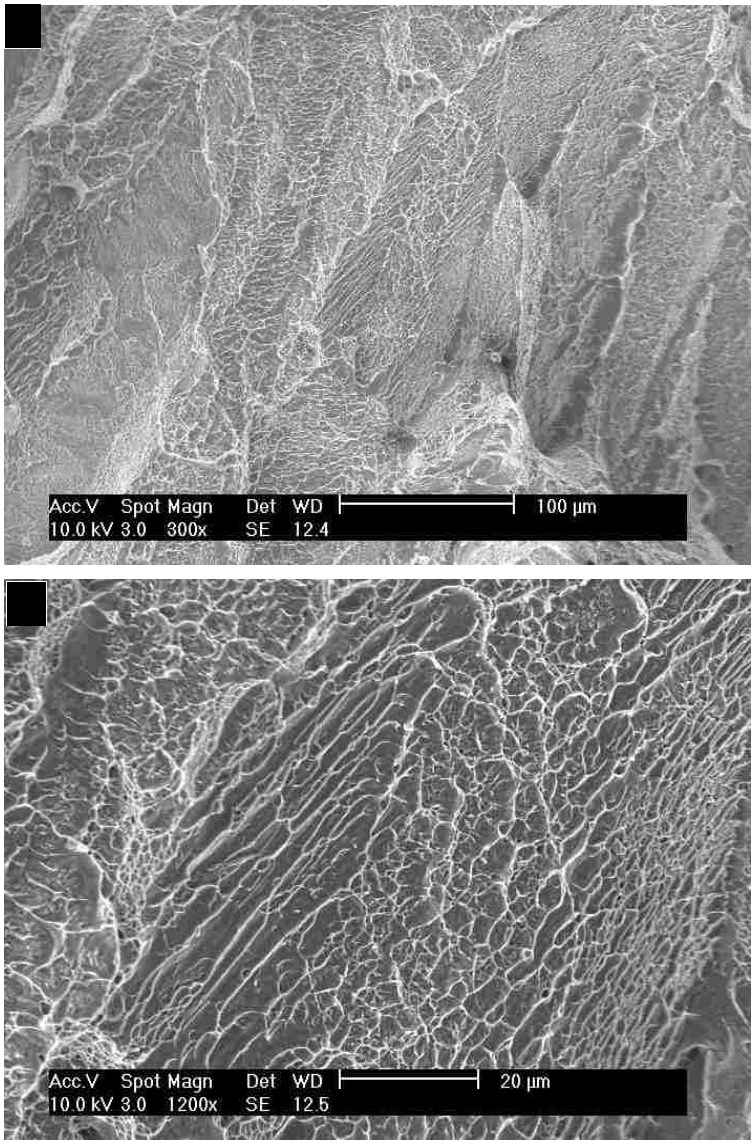

Figure 3.82: SEM micrographs at different magnification of the tensile test specimen fracture surface aged for 750°C annealed for 1 hour plus 500°C aging for 4 hours (a) magnification: 300x (b) magnification: 1200x

3.2.2.4 Annealing at 750°C for 1 hour plus aging at 500°C for 5 hours

The BM microstructure, Figure 3.83, shows the lath and spherical α phase textured in the β matrix. The spherical α size is 1.6±0.5μm and the lath α size is 7.9±1.9μm. When combing these two morphology α, the average α grain size is 5.9±4.6μm. In addition, the α volume fraction is 43.7±4.0%. Figure 3.84 shows the microstructure of the HAZ. Besides the dendritic α, the primary α from the annealing

step can be observed on the HAZ. The α volume fraction is 39.2±1.2%. The average α grain size is 4.3±3.4μm. To specific, the lath α size is 6.2±1.9μm and the spherical α size is 0.7±0.2μm. The FZ structure is shown in Figure 3.85. The α volume fraction is 48.2±2.2%. The primary α size is 1.9±0.9μm. The hardness profile of this sample is shown in Figure 3.86. It shows that the BM hardness is 399~415 HV, the HAZ hardness is 390~407HV, and the FZ hardness is 383~391HV. The YS, UTS, and EL was tested as 1098MPa, 1167MPa, and 2.39%, respectively. And the tensile test curve is shown in Figure 3.87.

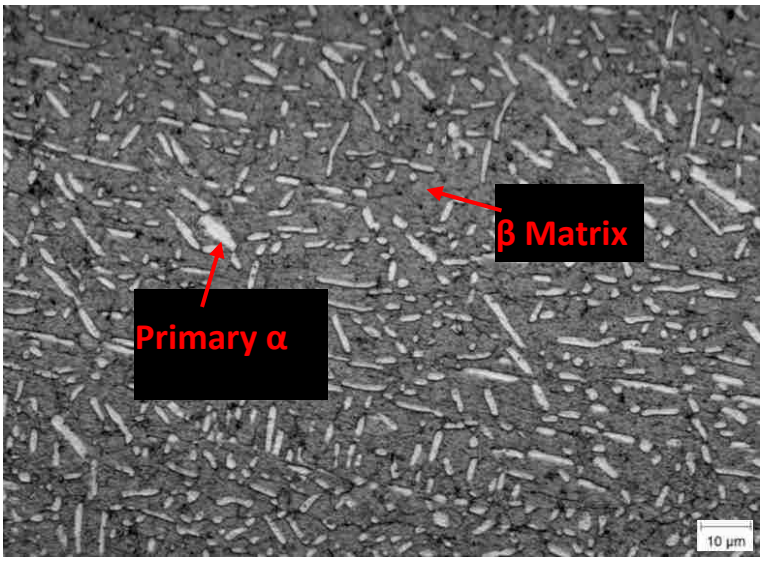

Figure 3.83: Light optical microstructure of annealing 1 hour plus aging 5 hours LBW Ti1023 base material (BM) presenting the primary α (bright area) and β matrix phase (gray area)

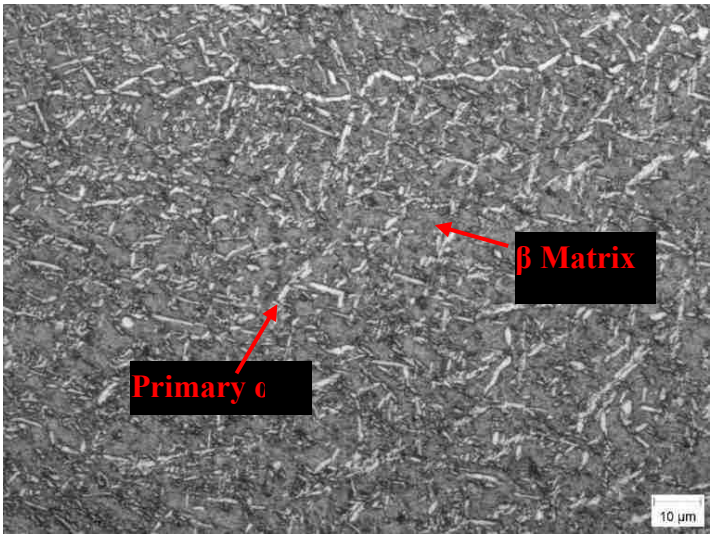

Figure 3.84: Light optical microstructure of annealing 1 hour plus aging 5 hours LBW Ti1023 heat affected zone (HAZ) presenting the primary α (bright area) and β matrix phase (gray area)

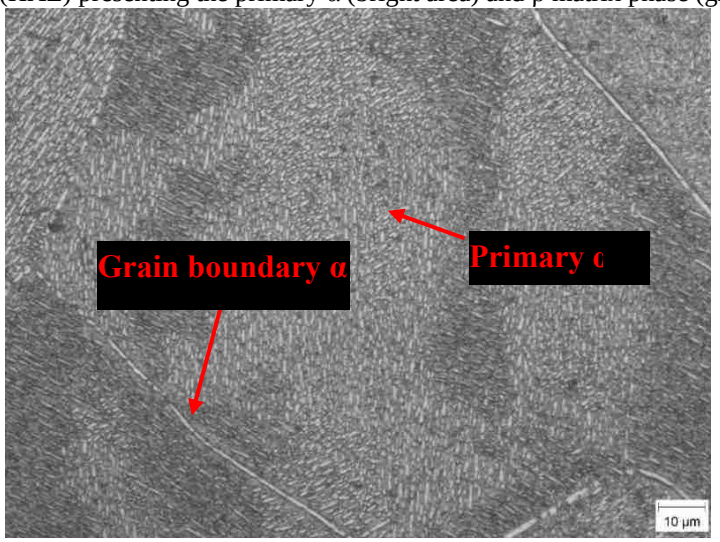

Figure 3.85: Light optical microstructure of annealing 1 hour plus aging 5 hours LBW Ti1023 fusion zone (FZ) shows primary α and grain boundary α

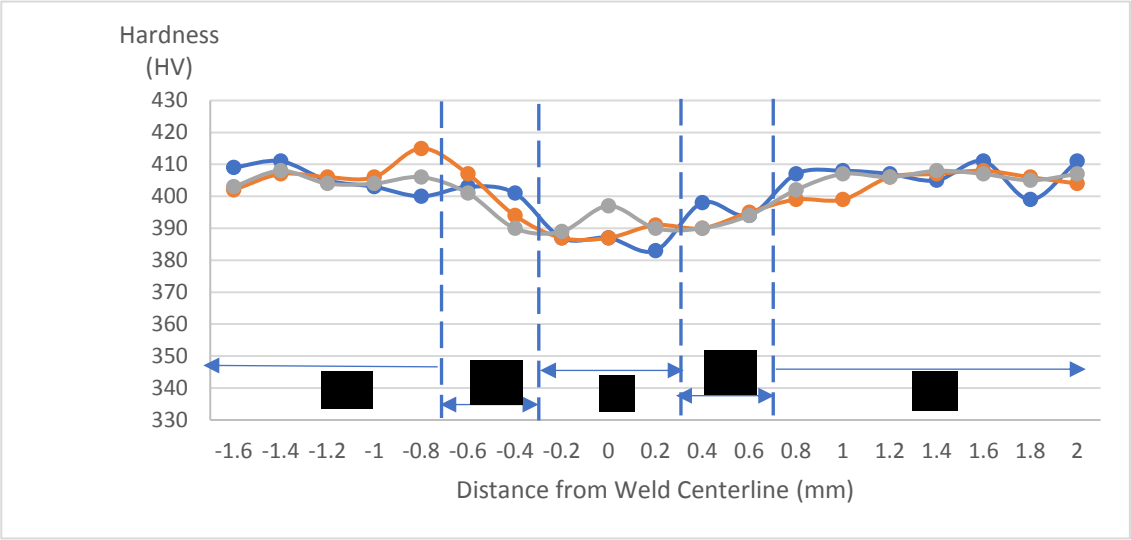

Figure 3.86: The hardness profile of three zones of annealing 1 hour plus aging 5 hours

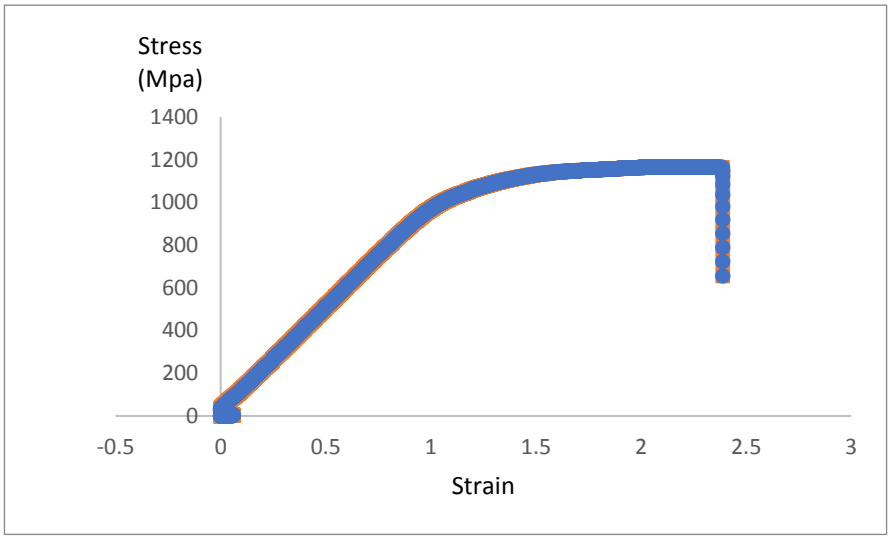

Figure 3.87: The engineering stress-strain curve of annealing 1 hour plus aging 5 hours

3.2.2.5 Annealing at 750°C for 1 hour plus aging at 500°C for 8 hours

The optical image of BM is shown in Figure 3.88. The α volume fraction is 37.4±2.6%. The average α grain size is 5.9±5.0μm. Separately, the spherical α size is 1.3±0.4μm and the lath α size is 9.4±2.1μm. In Figure 3.89, the α volume fraction is 32.7±3.5% on the HAZ. This dendritic α size is 5.3±2.3μm. When observing the FZ (Figure 3.901), the α volume fraction is 48.9±2.7%. In addition, the primary α size is 2.2±1.0μm. The hardness profile is shown in Figure 3.91. The hardness of these three zones are 349~391HV (BM), 353~389HV (HAZ), and 352~370HV (FZ). The tensile test result is shown in Figure 3.92. The YS is 1072MPa, the UTS is 1136MPa, and the EL is 1.79%. Figure 3.93 shows the higher strain area located on the FZ.

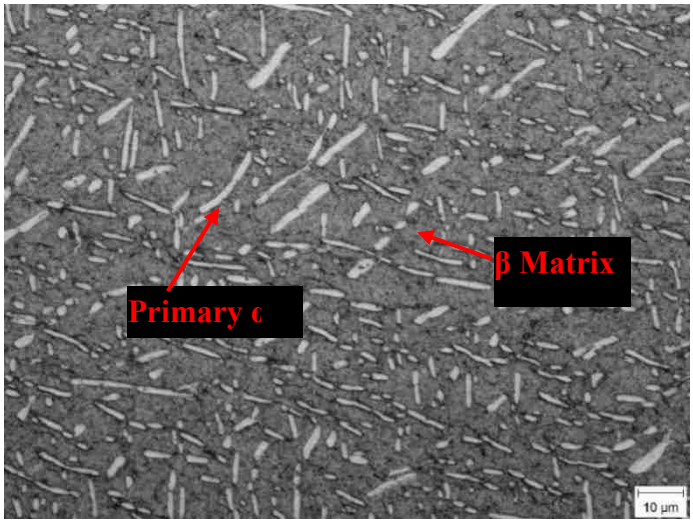

Figure 3.88: Light optical microstructure of annealing 1 hour plus aging 8 hours LBW Ti1023 base material (BM) presenting the primary α (bright area) and β matrix phase (gray area)

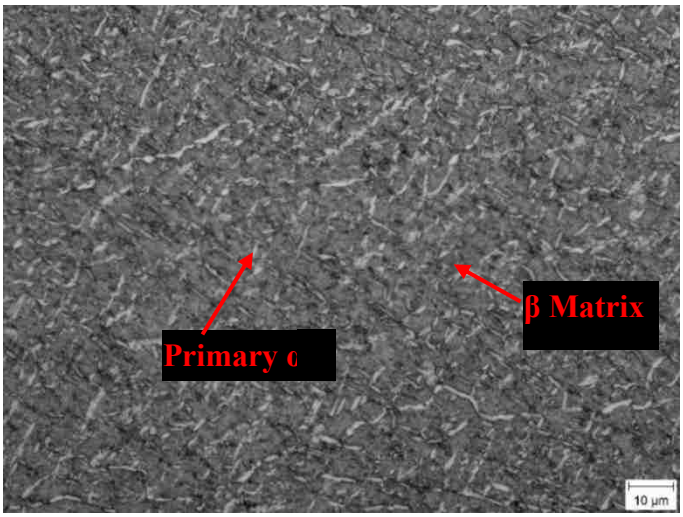

Figure 3.89: Light optical microstructure of annealing 1 hour plus aging 8 hours LBW Ti1023 heat affected zone (HAZ) presenting the primary α (bright area) and β matrix phase (gray area)

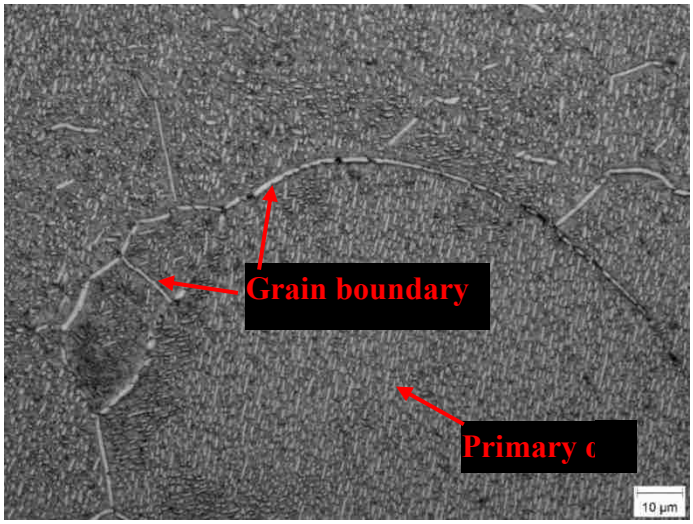

Figure 3.90: Light optical microstructure of annealing 1 hour plus aging 8 hours LBW Ti1023 fusion zone (FZ) shows primary α and grain boundary α

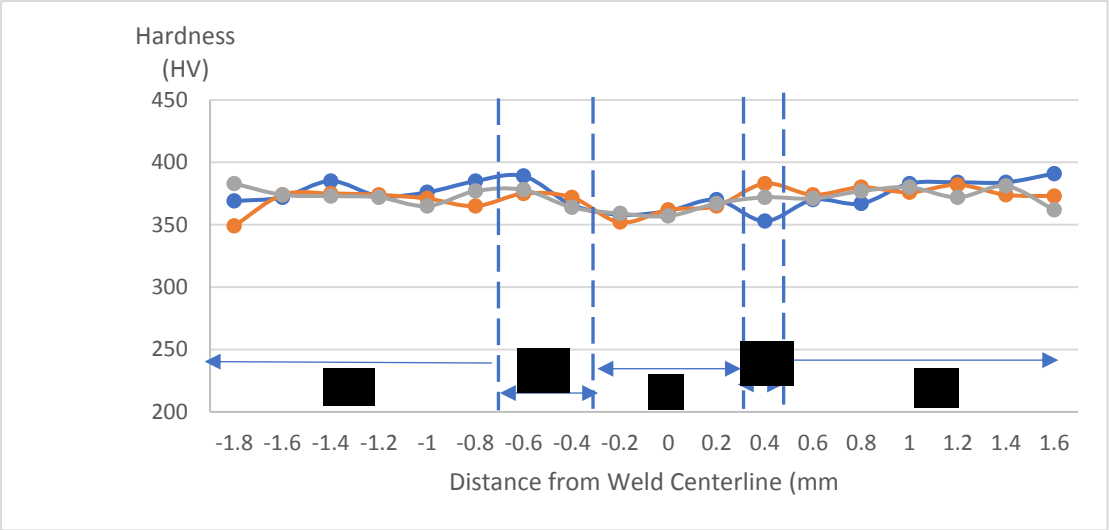

Figure 3.91: The hardness profile of three zones of annealing 1 hour plus aging 8 hours

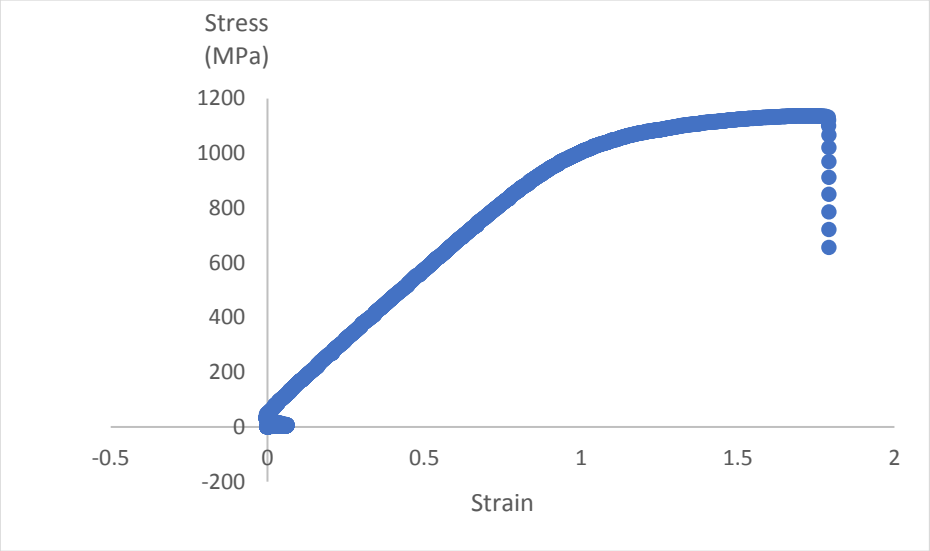

Figure 3.92: The engineering stress-strain curve of annealing 1 hour plus aging 8 hours

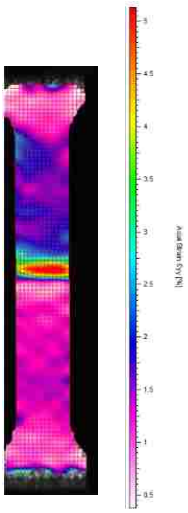

Figure 3.93: Strain map of the sample during tensile testing. The different colors specify strains

3.3 The Relationship Between Microstructure, Microhardness and Tensile Strength of As-Welded and Post Weld Heat Treatment Ti1023

Two PWHT groups, Aging and Annealing+Aging, are discussed separately in this chapter. In each group, the microstructure and microhardness results can be divided into three zones and discussed individually. However, the tensile strength can-not be tested specifically in each zone due to the fact that the tensile test sample contains all three zones. Finally, the optimization of each group is proposed.

3.3.1 Aging

3.3.1.1 Microstructure change

The curve of α volume fraction and average grain size on the BM under different aging time is shown in Figure 3.94. The α volume fraction increases as the aging time increases until 5 hours aging, and then it decreases as the aging time increasing. As for the average α grain size curve, it increases until 10.5 hours aging, and then decreases with longer aging time. This α morphology modification was caused by the heat from the aging process. In addition, because the secondary α was formed from the same step and this secondary α has the same crystal structure (HCP) with primary α, this secondary α also contributed to the α morphology. Therefore, with the aging time from 2.5 to 5 hours, the α volume fraction increases but almost keeps the same size. The main trend is to increase the α volume fraction in this period. With the

aging time from 5 to 10.5 hours, the α volume fraction becomes lower. But the average α grain size turns to longer. So, during this period, the main trend is to increase the α grain size. Finally, with the aging time from 10.5 to 20 hours, both of the α volume fraction and average grain size are decreased. However, from the microstructure of aging time of 20 hours BM (Figure 3.54), the α grain turns coarser. Thus, the α grain did not increase its length but grow coarser during this period.

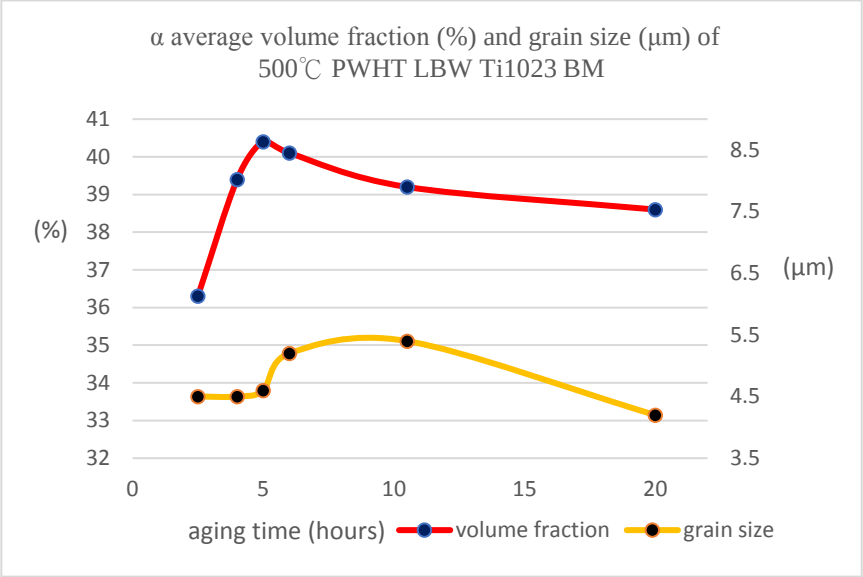

Figure 3.94: The average α volume fraction and grain size of 500ºC PWHT LBW Ti1023 BM

Figure 3.95 shows the relation between the α volume fraction, grain size and aging time of 500ºC PWHT LBW Ti1023 BM. Both of the volume fraction and grain size curve present an increasing from 2.5 to 5 hours, and then decreased from 5 to 6 hours, and following by keeping almost the same amount of α from 6 to 20 hours. On the HAZ, the α morphology was affected by the heat from not only aging but also laser

welding. Generally, the volume fraction and grain size trend on the HAZ are similar to it on the BM.

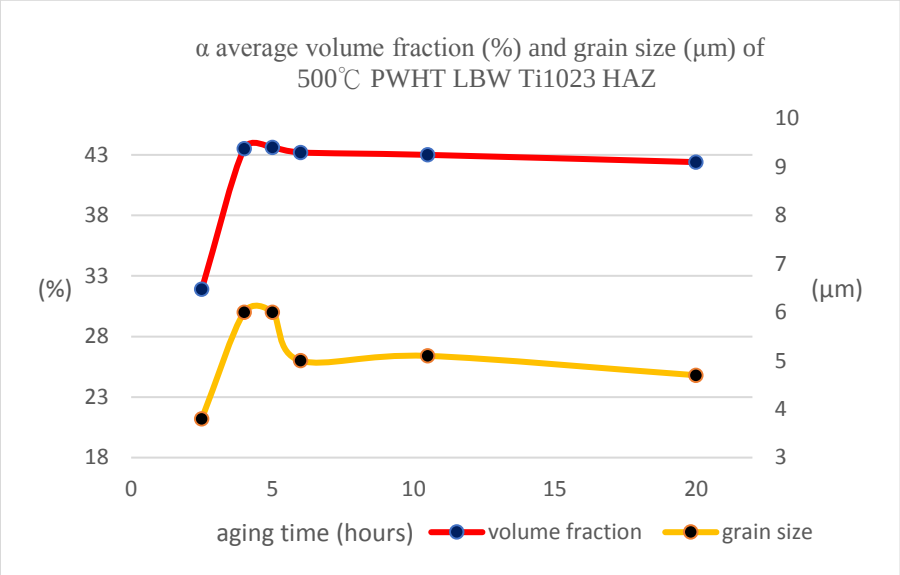

Figure 3.95: The average α volume fraction and grain size of 500°C PWHT LBW Ti1023 HAZ

3.3.1.2 Microhardness Profile

The hardness profiles of 500°C aging LBW Ti1023 in the BM, HAZ and FZ are shown in Figures 3.96-3.98 In these profiles, the aging 0 hour is without heat treatment, that represents the as-welded sample. When observing these three hardness profiles, the main different is the hardness decreased from aging 0 hour to 4 hours in the BM. But, the hardness presents increases at the same aging period on the HAZ and FZ. It is believed that the amount of the primary α and secondary α contributed to this difference. First, it has been discussed that the α phase is the main structure for increasing the hardness due to its HCP crystal structure in the chapter 3.1.2.1. Second,

the original primary α and aging secondary α are the composition of the whole α phase on the BM and HAZ. But, just aging secondary α exists on the FZ. Third, because the α phase was formed from the α stabilizer and the weight percentage was consistency, the amount of whole α phase is fixed for each sample. For example, in the BM, part of the α stabilizer formed the original primary α, and then, the rest of α stabilizer was used to form the secondary α. As for the HAZ, part of the α stabilizer formed the original primary α. But, the heat from the laser welds dissolved the α phase and released some α stabilizer. Therefore, when comparing to the BM, there was more α stabilizer and it could form the secondary α on the HAZ. Another microstructure on the FZ, because the primary α phase was all transform to the β phase and released all α stabilizer, whole α stabilizer can be used to form the secondary α. Thus, from as-welded to aging 2.5 hours on the BM, the secondary α was not formed enough to affect the hardness. That made the hardness dominant by the primary α during this period in the BM. The higher α volume fraction on the as-welded contributed this phenomenon. As for the HAZ and FZ, the hardness was dominant by the secondary α. Especially by observing the hardness profile in the FZ, there was no α phase in the as-welded material and then aging made the hardness increased. In addition, comparing to the 40.1% α volume fraction of as-welded BM, there are no primary α existed in the FZ of every aging sample. However, the hardness of each aging profile is still higher than it in the as-

welded BM.

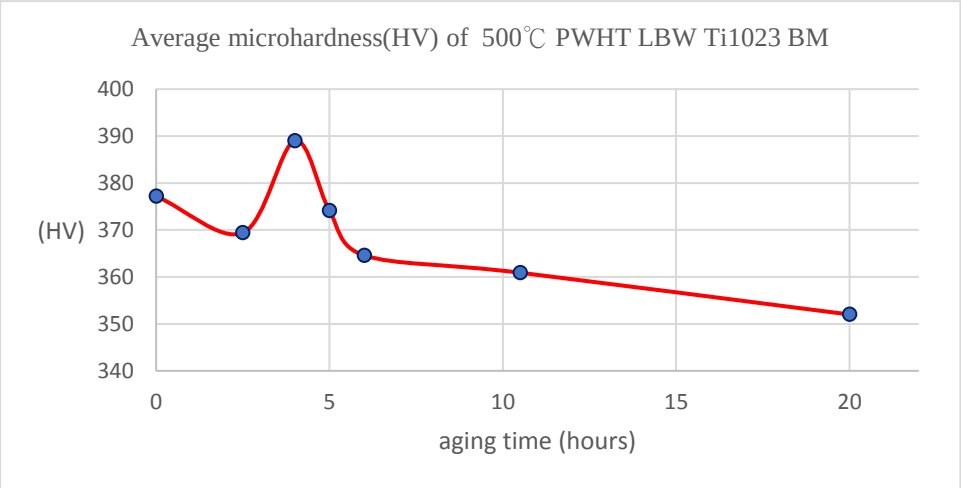

Figure 3.96: The average microhardness of 500°C PWHT LBW Ti1023 BM

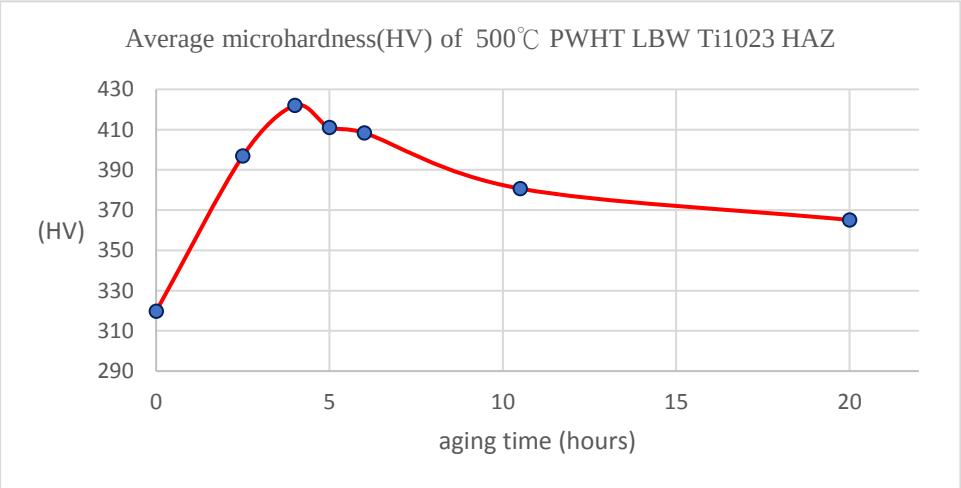

Figure 3.97: The average microhardness of 500°C PWHT LBW Ti1023 HAZ

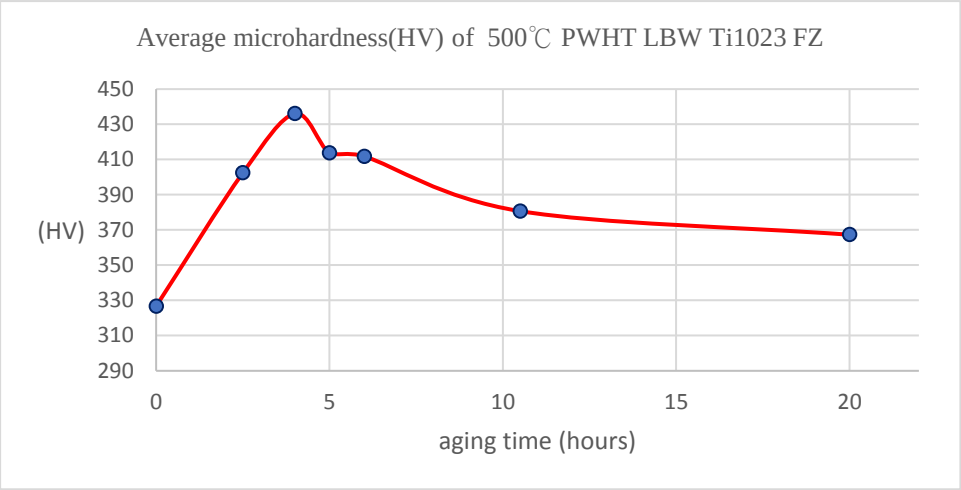

Figure 3.98: The average microhardness of 500°C PWHT LBW Ti1023 FZ

3.3.1.3 Tensile Strength Curve

For the tensile strength test, the stress curves representing YS, UTS, and EL values in the 500°C aging sample as a function of aging time are shown in Figure 3.99. It can be observed that the tensile strength increased as the aging time increased from 0 to 4 hours. And then, the tensile strength began decreased as the aging time from 4 to 6 hours. When the aging time between 6 to 20 hours, the YS and UTS continued to decrease, but the EL turned to increase. The tendency of YS and UTS is similar to the tendency of BM α volume fraction and the hardness profile. In addition, comparing to the as-welded, all of the samples after aging have increase of YS, UTS, and EL.

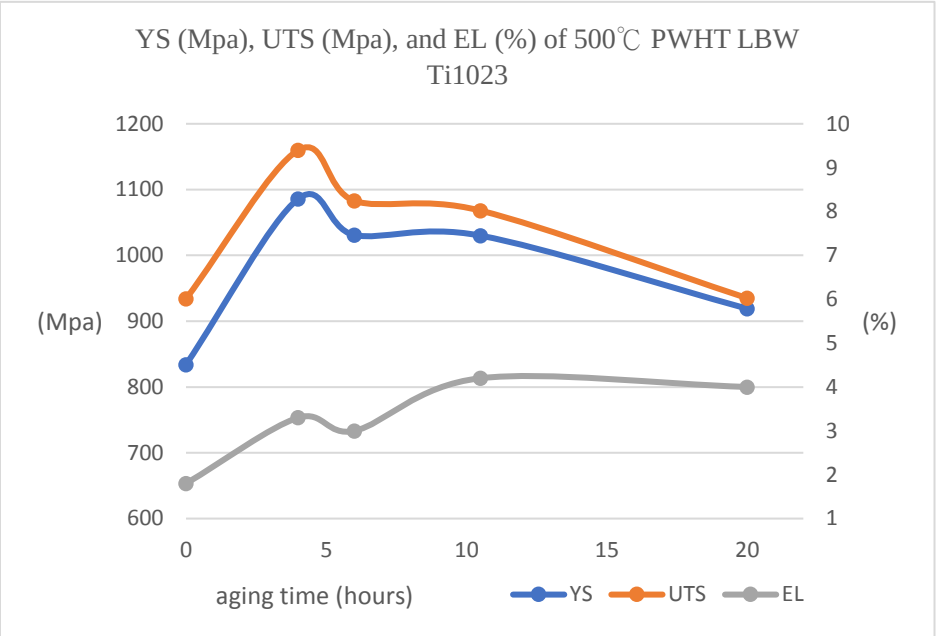

Figure 3.99: The tensile strength of 500°C PWHT LBW Ti1023

3.3.1.4 Optimization of Aging

In this aging group, the optimization heat treatment condition is chosen as 500°C aging for 4 hours and following by air cooling. This heat treatment owns the highest hardness in the FZ among the six aging conditions. In addition, the YS and UTS of this sample are also the highest. Although this sample does not own the best EL, it still has a good improvement when compared to the as-welded.

3.3.2 Annealing+Aging

3.3.2.1 Microstructure Change

The relationship of α average volume fraction and grain size from 750+500ºC PWHT LBW Ti1023 in the BM, HAZ, and FZ are shown in Figure 3.100-3.102. In these figures, all samples were treated by 750ºC annealing for 1 hour and then through different 500ºC aging times. To simplify, these figures were plot as different aging time. In addition, the aging time 0 hour means the sample just through 750ºC annealing for 1 hour and following by water quenching (without any aging). The curve of α volume fraction and grain size on the BM is similar to it on the HAZ. The α volume fraction increased with the aging time from 0 to 5 hours, and then decreased with the aging time from 5 to 8 hours. As for the α grain size curve, it increased as the aging time increased. This α morphology of BM was shaped by the heat from both of the 750ºC annealing and 500ºC aging. In addition, the primary α formed from the 750ºC annealing and the secondary α formed from 500ºC aging were added into the original primary α grain on the BM. As for the HAZ, besides above affection, one more factor influence the α morphology: the heat from the welding. The heat dissolved some original primary α phase and released the α stabilizer. This α stabilizer contributed the above forming primary and secondary α grain. When observing the α volume fraction and grain size curves of FZ (Figure 3.102), both curves does not show obvious difference with the

aging time from 0 to 8 hours. Form the optical image, the β grain is full of the primary α on the FZ. So, the α volume fraction kept around 50% with different aging time. In addition, the α grain size kept around 2μm because the primary α that formed form annealing was limited in the β grain.

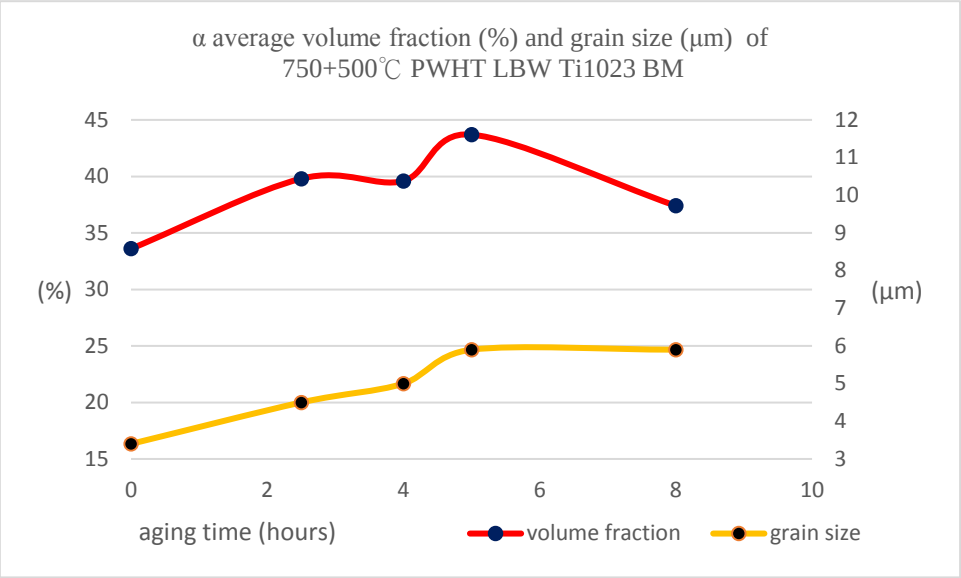

Figure 3.100: The average α volume fraction and grain size of 750+500ºC PWHT LBW Ti1023 BM

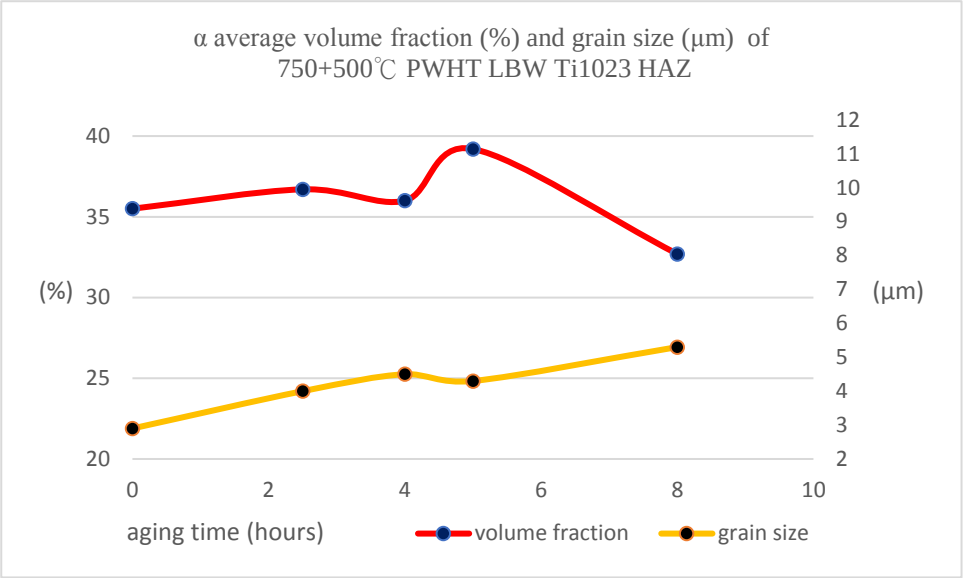

Figure 3.101: The average α volume fraction and grain size of 750+500°C PWHT LBW Ti1023 HAZ

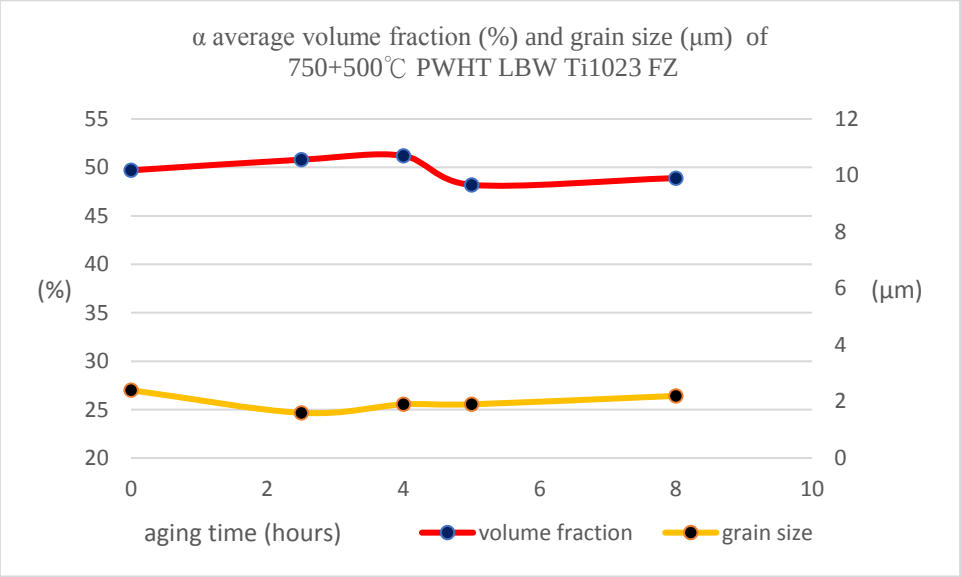

Figure 3.102: The average α volume fraction and grain size of 750+500°C PWHT LBW Ti1023 FZ

3.3.2.2 Microhardness Profile

Figure 3.103-3.105 show the average microhardness profile for 750+500°C PWHT LBW Ti1023 in the BM, HAZ, and BM. The curve shows the similar tendency for three zones. The hardness increased with the aging time from 0 to 5 hours, and then

decreased with the aging time from 5 to 8 hours. Although this hardness was influence by both of the primary α and secondary α, these hardness profiles is also similar to the curve tendency of α volume fraction on the BM and HAZ (Figure 3.100-3.101). In addition, by comparing the aging time from 0 to 2.5 hours, it can be observed that there are big hardness improvements in these three zones. Moreover, when observing Figure 3.105, the hardness curve is similar to it in the BM and HAZ. However, when observing Figure 3.102, the primary α volume fraction is almost consistent. Therefore, we can conclude that the hardness of FZ is dominant by the secondary α. Finally, the hardness of as-welded was not plotted in these figures, but it can be compared with the annealing 1 hour sample. The hardness of these three zones were all higher on the as-welded sample.

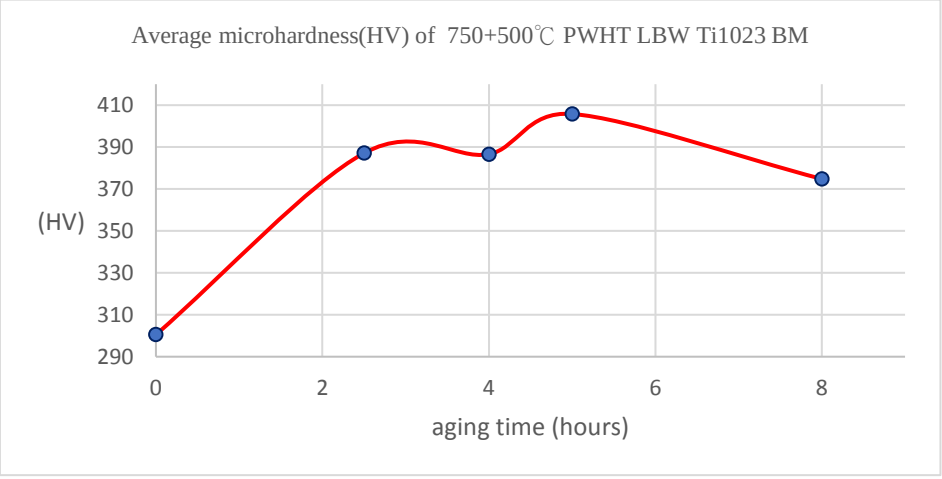

Figure 3.103: The average microhardness of 750+500ºC PWHT LBW Ti1023 BM

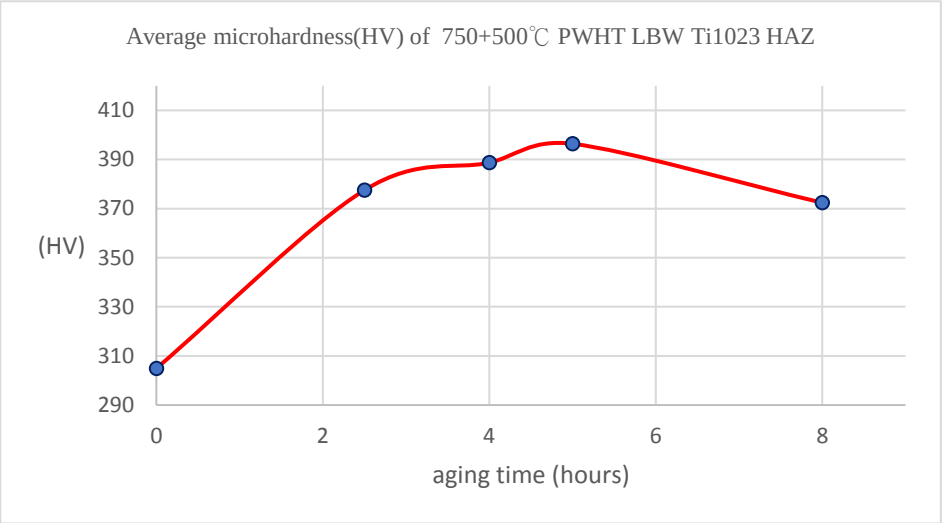

Figure 3.104: The average microhardness of 750+500°C PWHT LBW Ti1023 HAZ

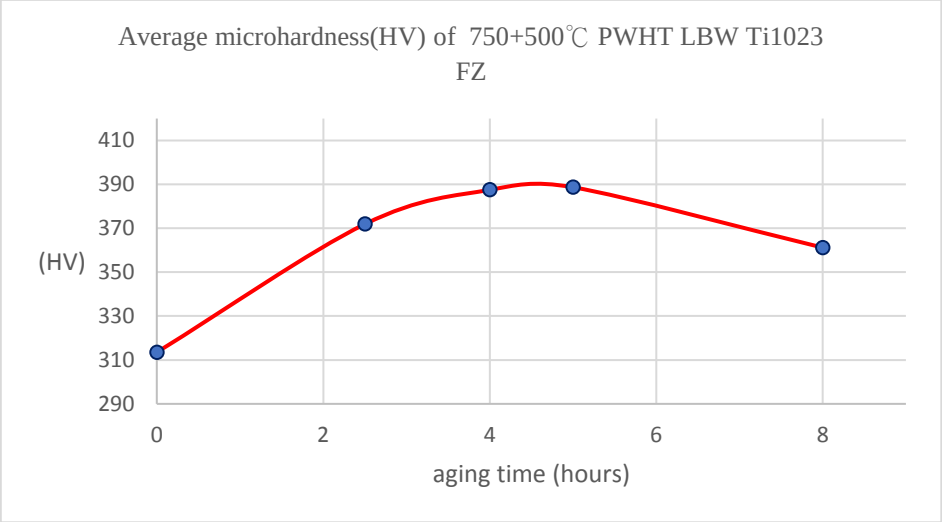

Figure 3.105: The average microhardness of 750+500°C PWHT LBW Ti1023 FZ

3.3.2.3 Tensile Strength Curve

The tensile strength curve is shown in Figure 3.106. The YS and UTS increased with the aging time from 0 to 4 hours, and then slightly decreased with the aging time from 4 to 8 hours. In addition, the tendency of curve is similar to the tendency of hardness profiles. As for the EL, it keeps around 2 % on each sample. Moreover, when comparing to the tensile strength of as-welded material, the YS and UTS of just annealed material for 1 hour sample decrease to the lower hardness values.

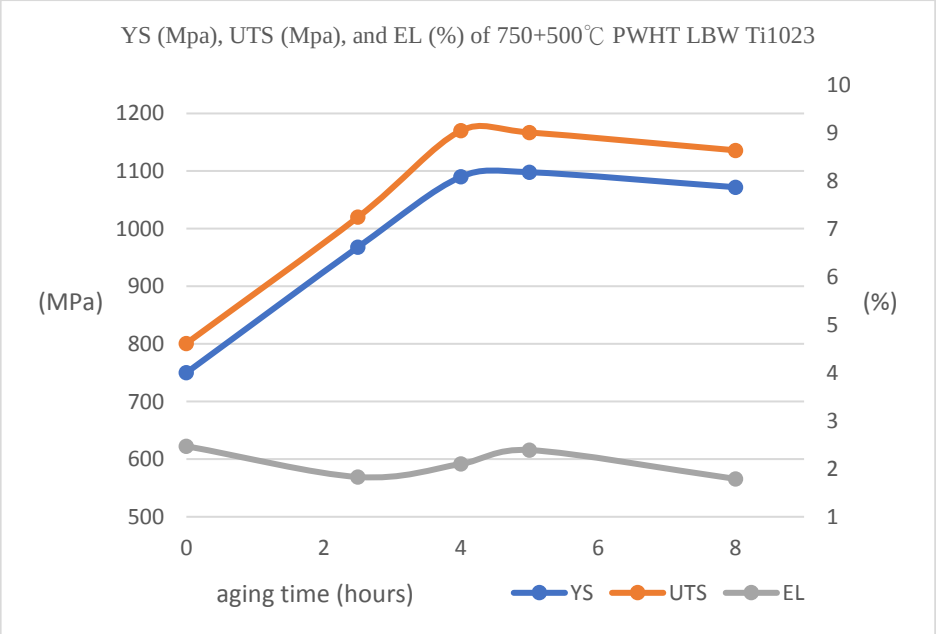

Figure 3.106: The tensile strength of 750+500ºC PWHT LBW Ti1023

3.3.2.4 Optimization of Annealing+Aging

In this group, the optimization heat treatment condition is chosen as 750ºC annealing for 1 hour and following by water quenching, then through 500ºC aging for

4 hours and following by air cooling. The hardness profiles through three zones on each condition in this group are shown in Figure 3.107. Although aging for 5 hours has highest hardness in this group, there is a hardness difference on three zones. Because the hardness difference may cause the weakness of mechanical performance, the optimization condition of this group should choose three zones' hardness almost equal. Thus, from Figure 3.107, the best choose is aging for 4 hours sample. In addition, the sample of this condition has better YS and UTS.

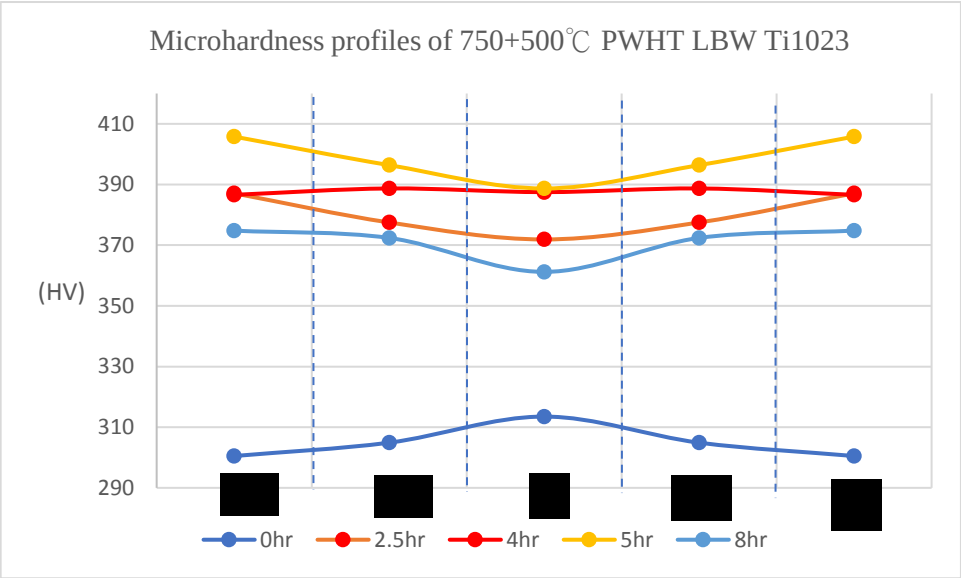

Figure 3.107: The microhardness profile of 750+500°C PWHT LBW Ti1023

4. Conclusions

The purpose of this research was to investigate the microstructure response and change in mechanical performance of Ti-10V-2Fe-3Al as a result of the laser beam welding and post weld heat treatment. Additional objective was to correlate the microstructure findings to the mechanical properties. Thus, the following conclusions can be proposed about the microstructure evolution, hardness profiles, tensile strength, and residual stress measurement of LBW Ti1023 as well as its PWHT.

1. Three zones with different microstructure and mechanical properties were formed in Ti1023 after laser beam welding. First, the spherical and lath α was observed in the β matrix for the base material (BM). Second, in heat affected zone (HAZ), heat from the laser welding process changed the primary α morphology from lath to mostly spherical particles. Comparing the BM with HAZ, both of the α volume fraction and average grain size are higher in the BM. Third, heating over β-transus temperature and rapid cooling resulted in only β presence in the fusion zone (FZ). In addition, a columnar and cellular dendritic β structure was found in the FZ. This structure was strongly affected by the heat flow in the weld solidification process. When evaluating its mechanical properties, the BM hardness is higher than it is in the HAZ and FZ, and all of the mechanical properties (YS, UTS, EL) decreased after LBW. The

reason for higher hardness in the BM is its higher α volume fraction. And, the α phase is harder than the β phase due to fact that the α phase crystal structure is HCP and the β phase has BCC structure. The results of the tensile test after LBW deteriorated because of the presence of the β phase, porosity, and undercut in the FZ.

2. The residual stress on the BM and FZ of LBW Ti1023 was measured. To detect multiple phases in the laser welded Ti1023 samples, several approaches with different parameters are needed to produce the best results. For the incident beam conditions, the divergence slit is $\frac{1}{4}°$ and the mask is 2 mm. As for the diffracted beam conditions, the soller slits are 0.04 radians and the fixed anti-scatter slit (FASS) size is 7.5 mm. Finally, the Pulse Height Discrimination (PHD) choose 55~75. The phase analysis of diffraction patterns shows that the Titanium α and β phases exist and each phase's volume fraction is different. However, the precise and clear residual stress measurements are not easy to obtain due to small specimen area, which results in weak diffraction peaks. Additionally, multiphase presence causes diffraction peak overlapping and makes it difficult to identify, additionally the high diffraction angles reduces peak intensity. According to these observations, only the first issue can be improved by preparing a larger area of specimen. The other two issues still

have to be addressed in a different matter.

3. When comparing to the as-welded results, the PWHT improves the mechanical properties of the FZ in all cases except for the post weld heat treatment at 750^{o}C for 1 hour. In addition, two groups of heat treatment conditions were designed and studied: aging and aging+annealing.

   - The secondary α that was formed from aging at 500^{o}C can obviously increase hardness on the FZ. However, this secondary α phase was too fine to be observed by the light optical microscope. Therefore, by applying the characteristic of the α phase and back-scattered electrons, the scanning electron microscope (SEM) was used to find the secondary α. Because the α phase is formed form the α stabilizer (Al is the main α stabilizer in Ti1023) and the lower atomic number element presents darker area on the back-scattered electrons images, it can be observed that the secondary α was found and widely distributed within the FZ. In this group, the optimized PWHT condition is 500^{o}C aging for 4 hours and followed by air cooling. This heat treatment condition resulted not only in the highest hardness in the FZ but also in the highest YS and UTS values among the all six aging conditions.
   - In another heat treatment (annealing+aging), the primary α was formed

from 750°C annealing step and the secondary α were formed from 500°C aging step. Both of the primary and secondary α contributed to the higher hardness and tensile strength. The optimization PWHT condition of this group is 750°C annealing for 1 hour followed by water quenching, then followed by 500°C aging for 4 hours and following by air cooling. The hardness of this heat treatment with in three welding zones is almost equal, Therefore, it avoids the weak area which is made from to the hardness difference on the tensile test sample.

5. Future Work

The performed research provides good understanding of micro metallurgy effects and macro mechanical properties of LBW Ti1023 and its PWHT. Based on the findings of this study, some ideas for future work are recommended below.

1. The impact test can be introduced to measure toughness response in the LBW Ti1023 and its PWHT in comparison to the tensile results. The impact test sample should be prepared in accordance with ASTM D256 standard.
2. The residual stress of LBW Ti1023 is difficult to measure due to the limitation of diffraction patterns. However, this is still a very interesting topic and worth for further investigation.

References

[1] R. Boyer, G. Welsch, E.W. Collings, *Materials Properties Handbook: Titanium Alloys*, ASM International, 1994, p.3,34,36,836-838

[2] G. Lutjering, J.C. Williams, *Titanium*, 2nd Ed., Springer-Verlag, 2003, p.9,16-21,24,29,30,35,36,182,283-295,337-354

[3] http://wap.sciencenet.cn/blogview.aspx?id=944802

[4] H.W. Rosenberg, *The Science, Technology and Application of Titanium*, Pergamon Press, 1970, p.851

[5] F.H. Froes, *Titanium—Physical Metallurgy, Processing, and Applications*, ASM International, 2015, p.54,69,78-82

[6] M.J. Donachie, *Titanium: A Technical Guide*, 2nd Ed., ASM International, 2000, p.13,16,21-24, 66-69, 247-253

[7] S. Nag, *Influence of Beta Instabilities on the Early Stage of Nucleation and Growth of Alpha inBeta Titanium Alloys*, Dissertation, The Ohio State University, 2008

[8] P.J. Bania, *Beta titanium alloys in the 1990's*, TMS, Warrendale, PA, 1993, p.3-14

[9] G. Terlinde, H.J. Rathjen, K.H. Schwalbe, *Microstructure and Fracture Toughness of the Aged β-Ti Alloy Ti-10V-2Fe-3AI*, Metallurgical Transactions A 19, 1988, p.1037-1049

[10] R.R. Boyer, H.W. Rosenberg, *Beta Titanium Alloys in the 1980's*, The Metallurgical Society, 1984, p.19-60

[11] F. Ho, C.P. Ju, C. Lin, *Structure and properties of cast binary Ti-Mo alloys*, Biomater., Vol.20, 1999, p.2115-2122

[12] Y.A. Bagariatskii, G.I. Nosova, T.V. *Tagunova, Factors in the Formation of Metastable Phases in Titanium-Base Alloys*, Dokl. Akad. Nauk. SSSR, Vo. 3, 1959, p.1014-1018

[13] J.D. Cotton, J.F. Bingert, P.S. Dunn, R.A. Patterson, *Microstructure and*

Mechanical Properties of Ti-40Wt Pct Ta (Ti-15 At. Pct Ta), Metallurgical and Materials Transactions, Vol. 25, 1994, p.461-472

[14] J.M. Silcock, M.H. Davies, H.K. Hardy, *The Mechanism of Phase ransformations in Solids, Institute* of Metals, 1956, p.93

[15] B.S. Hickman, *Omega Phase Precipitation in Alloys of Titanium with Transition metals,* Transactions of the Metallurgical Society of AIME, Vol. 245, 1969a, p.1329-1335

[16] S. Nag, *Influence of Beta Instabilities on the Early Stage of Nucleation and Growth of Alpha inBeta Titanium Alloys*, Dissertation, The Ohio State University, 2008

[17] The Welding Institute (TWI), https://www.twi-global.com/

[18] W. W. Duley, *Laser Welding*, The Wiley-Interscience, 1999, p.11, 15, 124

[19] P.E. Denney, E.A. Metzbower, *Laser Beam Welding of Titanium,* Welding Research Supplement, 1989, p.342-346

[20] A. Chamanfar, T. Pasang, A. Ventura, W.Z. Misiolek, *Mechanical Properties and Microstructure of Laser Welded Ti-6Al-2Sn-4Zr-2Mo (Ti6242) Titanium Alloy*, Materials Science &Engineering A 663, 2016, p.213-224

[21] T. Pasang, J.M.Sánchez Amaya, Y. Tao, M.R. Amaya-Vazquez, F.J. Botana, J.C Sabol, W.Z. Misiolek, O. Kamiya, *Comparison of Ti-5Al-5V-5Mo-3Cr Welds Performed by Laser Beam, Electron Beam and Gas Tungsten Arc Welding,* Procedia Engineering 63, 2013, p.397-404

[22] G.Q. Wang, A.P. Wu, Y. Zhao, G.S. Zou, Q. Chen, J.L. Ren, *Effect of post-weld heat treatment on microstructure and properties of Ti-23Al-17Nb alloy laser beam welding joints,* Transactions of Nonferrous Metals Society of China 20, 2010, p.732-739

[23] C.C. Zhang, T.C. Zhang, Y.J. Ji, J.H. Huang, *Effects of heat treatment on microstructure and microhardness of linear friction welded dissimilar Ti alloys*, Transactions of Nonferrous Metals Society of China 23, 2013, p.3540-3544

[24] C.T. Hsieh, R.K. Shiue, R.T. Huang, L.W. Tsay, *The effect of post-weld heat treatment on the microstructure and notched tensile fracture of Ti-15V-3Cr-3Al-3Sn to Ti-6Al-4V dissimilar laser welds*, Materials Science & Engineering A653, 2016, p.139-146

[25] P.J. Withers, H.K.D.H. Bhadeshia, *Residual Stress Part 1- Measurement Techniques*, *Materials Science and Technology, Vol* 17, 2001, p.355

[26] M.E. Fitzpatrick, A.T. Fry, P. Holdway, F.A. Kandil, J. Shackleton and L. Suominen, *Measurement Good Practice Guide*, No. 52, National Physical Laboratory, 2005, p.4

[27] G. S. Schajer, *Practical residual stress measurement methods*, John Wiley & Sons Inc., 2013, p.145-146

[28] W. Raea, Z. Lomasb , M. Jacksonc , S. Rahimi, *Measurements of residual stress and microstructural evolution in electron beam welded Ti-6Al-4V using multiple techniques*, Materials Characterization 132, 2017, p.10-19

[29] X.K. Meng, J.Z. Zhou, C. Su, S. Huang, K.Y. Luo, J. Sheng, W. Tan, *Residual stress relaxation and its effects on the fatigue properties of Ti6Al4V alloy strengthened by warm laser peening,* Materials Science & Engineering A 680, 2017. p.297-304

[30] Z. Zhou, S. Bhamare, G. Ramakrishnan, S.R. Mannava, K. Langer, Y. Wen, D. Qian, V.K. Vasudevan, *Thermal relaxation of residual stress in laser shock peened Ti-6Al-4V alloy*, Surface & Coatings Technology 206, 2012, p.4619-4627

[31] T. W. Duerig, G. T. Terlinde, J. C. Williams, *Phase Transformations and Tensile Properties of Ti-10V-2Fe-3AI,* Metallurgical Transactions A, 1980, vol. 11A, p.1987

[32] G. Terlinde, T. W. Duerig, J. C. Williams, *Microstructure, tensile deformation, and fracture in aged Ti-10V-2Fe-3Al,* Metallurgical Transactions A, 1983, vol. 14A, p.2101-2115

[33] Y. Zhang, Y. S. Sato, H. Kokawa, S. H. C. Park, S. Hirano, *Microstructural characteristics and mechanical properties of Ti-6Al-4V friction stir welds*, Materials Science and Engineering A 485, 2008, p.448–455

[34] Ron J., R. L. Snyder, Introduction to X-ray powder diffractometry, Wiley, 1996

[35] http://www.icdd.com/, The International Center for Diffraction Data, Pattern: 44-1288

[36] J. Goldstein, D.E. Newbury, D. C. Joy, C. E. Lyman, P. Echlin, E. Lifshin, L. Sawyer, J.R. Michael, *Scanning electron microscopy and x-ray microanalysis*, 3rd Ed., Kluwer Academic/Plenum Publishers, 2003, p.141-143

[37] E. Tal-Gutelmacher, D. Eliezer, *The Hydrogen Embrittlement of Titanium-Based Alloys*, Journal of The Minerals, Metals & Materials Society, 2005, p.46-49

[38] Y Tao, *Microstructure Evolution and Phase Transformation of Welded Metastable Beta-Titanium Alloy (Ti-5Al-5V-5Mo-3Cr),* Thesis, Auckland University of Technology, 2016, p.108-112

[39] N. Norberg, *Grazing incidence multiple {hkl} stress*, Technical Manual, PANalytical B.V., The Netherlands, p.11-16

Appendix A

Table: Phase analyze - on the base of experimentaly measured diffraction patterns.
Ti10V2Fe3Al (Ti1023)

Reletive peak intensity calculation

volum fraction	Ti β	1
	Ti α	1

All diffraction lines are presented

Index	Description
s	strong lines
ss	separated strong lines
sw	separated weak lines
w	weak
un	unknown

Phase identyfication

Colour	Description
red	cubic
black	hexagonal
blue	unknown

Intensity uncodding

Signed	Description
bold (11)	>10
bold (14)	3 strongest
yellow	strongest one

All peak search at HighScorr sowtware done with parameters: 5,00 - 0,40 - 1,00 - 2,03

Standard diffraction pattern										As welded														Heat treated (HT)		
										BM (Base Metal)				HAZ (Heat Affceted Zone)				FZ (Fuzion Zone)					BM	FZ	FZ
Peak position Calculated	PDF	h	k	l	Intensity ICDD	Intensitie volume	Phase		Indeks	Rough surface	Etched surface		Cross section	Etched surface			Cross section	Etched surface			Cross section				
										1	1	2	1	1	2	2		1	2	3	1	2			
									uk		30.50							30.82		30.73			30.31		
									uk		33.95		33.89	33.94							34.00	34.04	33.91		
35.12		1	0	0	25	25	Ti α	hex	ss	35.2	35.26	35.28		35.22		35.20		35.27		35.37			35.27		
									uk	37.45															
38.46		0	0	2	30	30	Ti α	hex	s		38.42	38.47	38.37								38.25		38.38	38.39	
39.31	38.51	1	1	0	100	100	Ti β	cubic	s	39.25				39.27	39.30	39.26		39.31	39.25	39.26	39.27	39.22			39.85
40.21		1	0	1	100	100	Ti α	hex	s		40.24	40.23	40.32	40.41		40.38		40.40					40.35	40.19	40.34
									uk																
									uk	43.32															
									uk					45.30				45.53			45.48	45.45			
									uk					47.03				46.92				47.01			
									uk		50.74							50.74		50.68	50.85				
									uk	52.58															
53.05		1	0	2	13	13	Ti α	hex	ss		53.25	53.23	53.20	53.23	53.23	53.21		53.19		53.16		54.41	53.15	53.16	53.20
									uk				54.97												
56.73	55.59	2	0	0	12	12	Ti β	cubic	ss					56.73	56.80	56.79		56.73	56.67	56.70	57.04	56.93			57.68
									uk	57.04	57.88	57.87	57.87	57.56	57.57								57.72	57.66	
									uk					62.26				62.19			62.17	62.21			
63.01		1	1	0	11	11	Ti α	hex	ss	62.99	63.31	63.29	63.29	63.31	63.28	63.31		63.38		63.37	63.52		63.36	63.20	63.23
70.73		1	0	3	11	11	Ti α	hex	w	70.01	70.91	70.89	70.91										70.83	70.87	
71.12	69.66	2	1	1	17	17	Ti β	cubic	ss	71.33				71.17		71.31		71.11	71.11	71.12	71.03	71.21			
									uk		72.72	72.63											72.45	72.31	
74.23		2	0	0	1	1	Ti α	hex	w		74.72			74.67		74.56									
76.30		1	1	2	9	9	Ti α	hex	w	75.81	76.62	76.63	76.62					76.78		76.48			76.63	76.59	
77.45		2	0	1	6	6	Ti α	hex	w	77.62	77.89			77.74		77.88		77.99					77.83	77.61	
									uk	79.4															
82.38		0	0	4	1	1	Ti α	hex	w	82.49															
84.44	82.52	2	2	0	4	4	Ti β	cubic	w	84.7				84.50		84.64		84.52		84.59		84.44			
86.85		2	0	2	1	1	Ti α	hex	w	86.74														86.03	
92.83		1	0	4	1	1	Ti α	hex	w		93.01									89.65			92.99		
97.44	95.01	3	1	0	5	5	Ti β	cubic	sw					97.43				97.49		97.52		97.73			
									uk	98.61	99.90												99.59		
#####		2	0	3	2	2	Ti α	hex	w		103.00	103.06	103.03	102.97		102.91		103.11					102.97	103.09	
#####		2	1	0	1	1	Ti α	hex	w		106.87												106.64		
#####		2	1	1	4	4	Ti α	hex	w				109.97										109.99		
#####	107.74	2	2	2	1	1	Ti β	cubic	w	109.5	110.08	110.00								110.78				109.28	
#####		1	1	4	3	3	Ti α	hex	w		114.85		114.82	114.75		114.83									
#####		2	1	2	1	1	Ti α	hex	w														114.87	114.73	
																							120.56		
									uk	121.29	122.88			122.93		122.64						122.73		
#####	121.48	3	2	1	7	7	Ti β	cubic	sw		125.57			125.63		125.64		125.83	125.23	125.48	125.92	125.60			
									uk		127.24		127.18												
									uk		130.97														
									uk									136.44							
																		137.81							
#####					1	1	Ti α	hex	w	141.55	140.96							140.87					140.96		
#####	137.70	4	0	0	1	1	Ti β	cubic	w																

Vita

Meng Fu Huang was born on July 25, 1981 in Kaohsiung, Taiwan. He grew up with his parents, Rui-Ju Zhuang and his younger brother, Dian-Long Zhuang. He graduated from Kaohsiung Municipal Kaohsiung Senior High School in 1999. Meng Fu obtained his Bachelor of Science in mechanical engineering at Chung Cheng Institute of Technology in 2003. He received a full fellowship and began his graduate studies under the guidance of Dr. Yung-Chiun Her at National Chung Hsing University in 2004. After two years of working on characterizing silver nanoparticle thin film, he earned his Master of Science in materials engineering. Then, he worked as a mechanical engineer in the 202th Arsenal till 2014. Once again, he obtained a full fellowship and then became a PhD candidate in mechanical engineering and mechanics at Lehigh University. For his doctoral research, he studies the effects of titanium after laser beam welding and post welded heat treatment under the guidance of Dr. Wojciech Z. Misiolek. In 2018, he graduated and received his Doctor of Philosophy in mechanical engineering and mechanics. After graduation, Meng Fu will be go back to the 202th Arsenal and work as a mechanical engineer.